2021

Electrocatalytic reaction driven flow

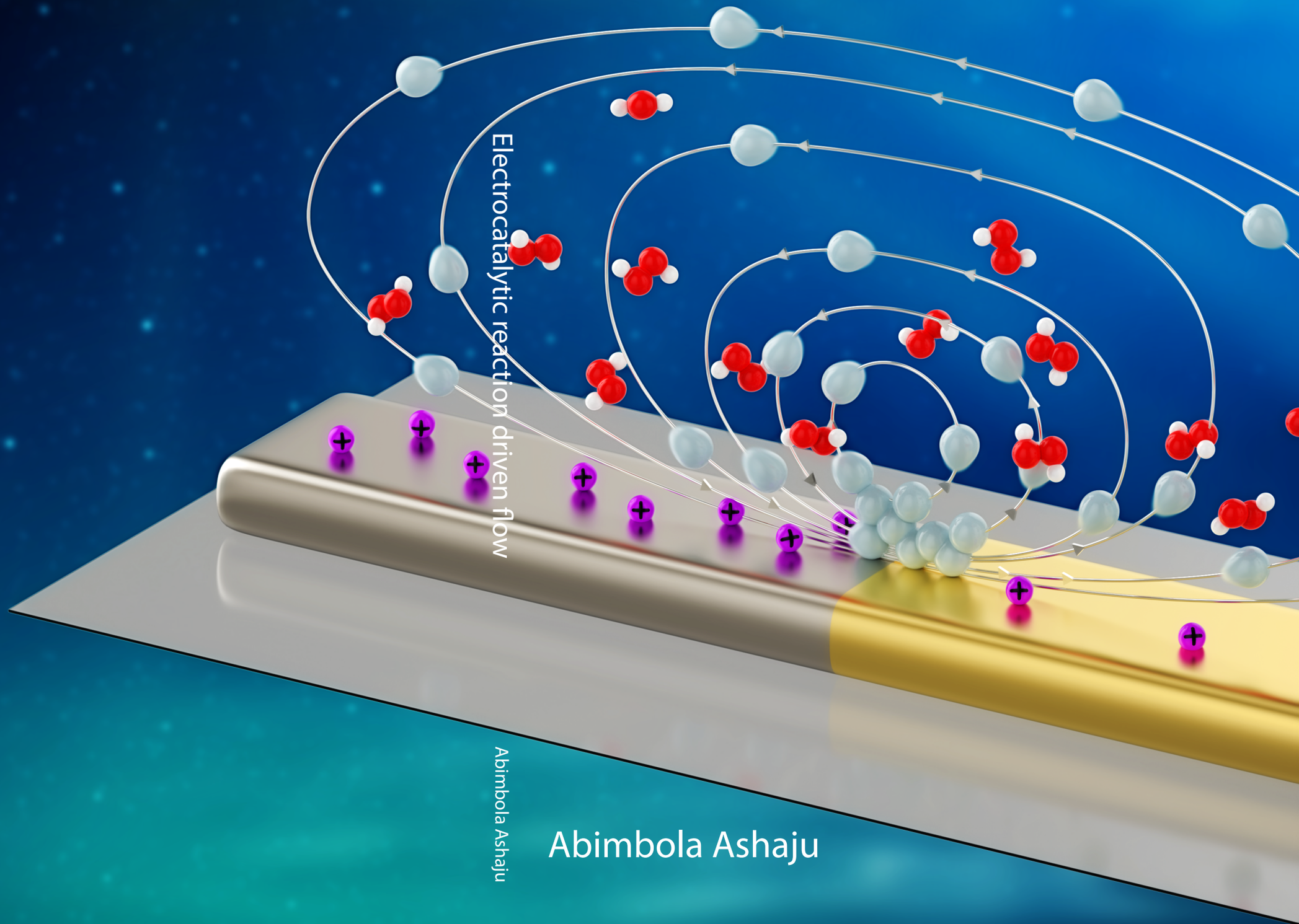

Electrocatalytic reaction driven flow

Abimbola Ashaju

Abimbola Ashaju

ISBN 978-90-365-5230-1

Electrocatalytic Reaction Driven Flow

Abimbola Ayodeji Ashaju

Thesis committee members:

Prof. dr. J. L. Herek (chairman)	UT, Enschede
Prof. dr. ir. R.G.H. Lammertink (promotor)	UT, Enschede
Dr. J.A. Wood (Co-supervisor)	UT, Enschede
Prof. dr. J.C.T. Eijkel	UT, Enschede
Prof. dr. S.J.G. Lemay	UT, Enschede
Dr. Corinna C Maaß	UT, Enschede
Prof. C. Cottin-Bizonne	Université Claude Bernard Lyon 1
Prof. Ali Mani	Stanford university, California

This work is part of the research programme Stirring the boundary layer with project number STW 016.160.312, which is financed by the Dutch Research Council (NWO).

This work was performed at
Soft matter, Fluidics and Interfaces
MESA$^+$ Institute for Nanotechnology
Faculty of Science and Technology
University of Twente
P.O. Box 217
7500 AE Enschede
The Netherlands

Electrocatalytic Reaction Driven Flow

ISBN: 978-90-365-5230-1
DOI: 10.3990/1.9789036552301
URL: https://doi.org/10.3990/1.9789036552301
Cover design:Somersault18:24 B.V.
Typeset in LaTeX
Printed by: Ipskamp printing

Copyright © 2021 by A.A.Ashaju. All rights reserved. No part of this work may be reproduced or transmitted for commercial purposes, in any form or by any means, electronic or mechanical, including photocopying and recording, or by any information storage or retrieval system, except as expressly permitted by the publisher.

Electrocatalytic Reaction Driven Flow

DISSERTATION

to obtain
the degree of doctor at the University of Twente,
on the authority of the rector magnificus,
Prof. Dr. ir. A.Veldkamp,
on account of the decision of the graduation committee,
to be publicly defended
on Friday the 3rd of September 2021 at 14:45

by

Abimbola Ayodeji Ashaju
Born on the 3rd of May 1988
in Lewisham, United kingdom

This dissertation has been approved by the promotor:

Prof. Dr. ir. R.G.H. Lammertink

Co-supervisor:

Dr. J. A. Wood

Dedication

This thesis is dedicated to my late guardian, Chief **M.D. Olayinka** (1926-2011). The seed that you've planted and nurtured has germinated and matured. I know you will be extremely proud of this accomplishment.

"In arranging the bodies in order of their electrical nature, there is formed an electro-chemical system which, in my opinion, is more fit than any other to give an idea of chemistry."

Jöns Jacob Berzelius

Contents

Chapter 1

Introduction

1.1 Background

During Feynman's famous talk titled "There's Plenty of Room at the Bottom" at the annual American Physical Society meeting at Caltech 1959, he posed a challenge on the design of a micromachine with a prize of $1000, which was won by a Caltech graduate named William McLellan [1]. William designed a tiny motor using a tweezer with an optical microscope, which weighed about $250\mu g$ (see Fig. 1.1). This challenge has inspired scientists that became actively involved in nanotechnology and nanoscience research and developmental activities where structures are synthesized, manipulated, and controlled at the molecular, atomic, and macromolecular scale for diverse applications.

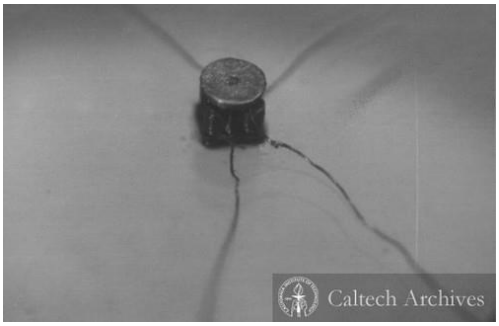

Figure 1.1: Optical micrograph of McLellan's micromotor. Source: Caltech Archives ID: RPF35.3-1

In the same vein, nature has engineered the translational and rotational motion of biological motors that functions primarily on the conversion of biochemical energy sourced from their surrounding nutrient molecules to adenosine triphosphate (ATP) that powers vital functions in living organisms [12, 9, 16, 8]. A good example is the motility of sperm powered by ATP. The supply of ATP is crucial for sperm performance and enhances the swimming velocity propelled by flagella [14]. These bioengineering feats by nature have inspired several interests in artificial micromotors aimed at understanding and replicating the complex functionalities of biological motors [13, 6, 15, 11].
A micromotor exhibits autonomous motion after being powered by the conversion of chemical energy from fuel sourced from its local environment. It was first demonstrated by the group of Whitesides, where they engineered hemicylindrical plates that are driven under the impulse of bubbles created during the decomposition of hydrogen peroxide catalyzed by platinum [2]. This concept was scaled down in 2004 by the team of Mallouk and Sen who developed

bimetallic catalytic nanorods [6, 10]. A single nanorod consists of a Pt-Au electrode pair that catalyzes the decomposition of hydrogen peroxide through oxidation and reduction reaction pathways (Fig 1.2). This heterogeneous surface reaction leads to the establishment of concentration and potential gradients that propelled the nanorod within its immediate surroundings [5]. If the

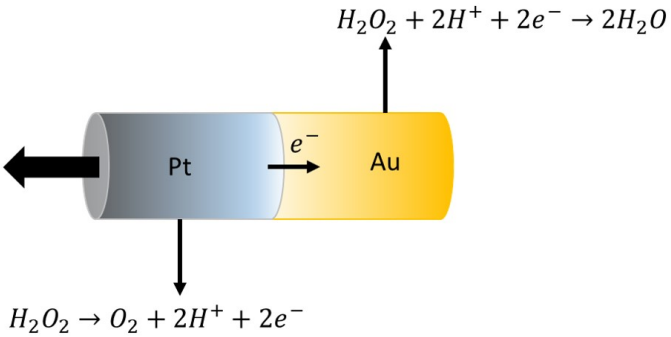

Figure 1.2: Schematic diagram of Pt-Au bimetallic nanorod.

motion of the catalytic nanorod is restricted by immobilizing it on a substrate and confined within a closed space with hydrogen peroxide, an electrocatalytic reaction-driven fluid flow will be generated. The flow is typically driven from the anode to cathode and recirculated at the upper region to fulfill flow continuity (Fig 1.3).

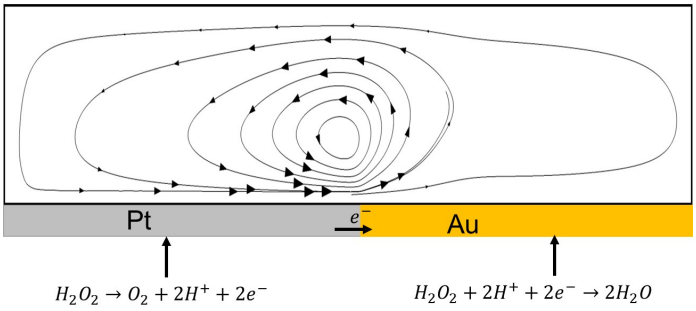

Figure 1.3: Schematic diagram of an electrocatalytic reaction flow- stream generated by an immobilized Pt-Au bimetallic nanorod.

This system, also referred to as a chemically powered micropump [17] has the potential for diverse microscale flow applications .

In this thesis, the concepts behind the electrocatalytic reaction-driven fluid flow (ERDF) generated by a Pt-Au and hydrogen peroxide system form the main subjects of interest, which consists of coupled mechanisms such as, electrode reactions, ions transport and convective fluid flow, etc. This project was initially conceived from the research theme "Stirring the boundary layer", whose aim is to exploit gradients that impose fluid flow near the interface, and establish mixing within the boundary layer (see Fig 1.4).

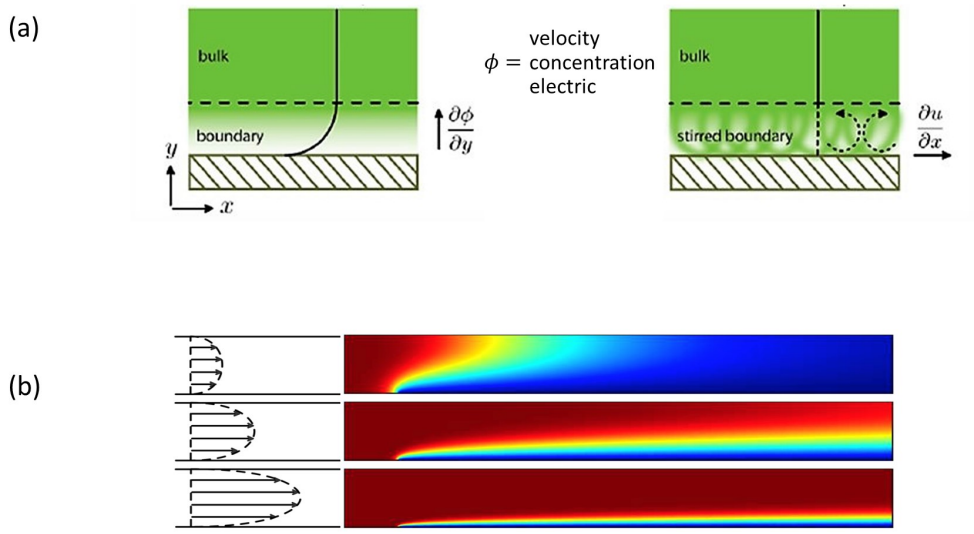

Figure 1.4: (a) A schematic that illustrates mixing within the boundary layer (b) Surface plot of the boundary layer that describes how mass transport is impacted by increase or decrease in boundary layer thickness

The fluid flow that is driven along an active catalytic surface has been termed diffusioosmosis, which is attributed to the establishment of a tangential concentration gradient of an ionic salt next to the charged wall [3, 4]. The concentration gradient establishes a pressure gradient and a net surface flow, which can also result in the movement of particles (known as diffusiophoresis) [7]. However, ERDF differs from diffusioosmosis due to the reaction of the charged surface with the electrolyte that results in the generation of an asymmetric concentration gradient of proton via oxidation and reduction reactions during the catalytic decomposition of H_2O_2 by platinum and gold electrodes, generates an electric field and electric body force that acts on the surface electric

double layer to induce net fluid flow. These phenomena result from electro and diffusiokinetic contributions.

1.2 Aims and objectives

To realize the full potential of ERDF for relevant applications, fundamental understanding of the controlling parameters that affect the chemo-mechanical actuation of the bimetallic system is crucial. This thesis aims to investigate and elaborate the key elements such as the proton gradient, the generated electric field, reaction kinetics, and diffusio-electroosmotic phenomena that controls the catalytically induced fluid flow, by using a combined experimental and numerical approach. These phenomena are decoupled and investigated independently to ascertain their influence on the overall electrocatalytic output. A proof of concept study is realized by using platinum and gold bi-electrodes that are immobilized on glass substrates within hydrogen peroxide solutions. The bimetallic electrodes allow the *in-situ* observation of the interfacial flow that is generated through heterogeneous surface reactions, as well as the spatial mapping and characterization of the reaction-induced proton gradient that is established during the generation and consumption of protons involving the electrochemical decomposition of hydrogen peroxide by platinum and gold electrodes. The electrochemical properties of the bimetallic system was studied using Pt-Au interdigitated electrodes that are bonded on a printed circuit board. This platforms offer a means of controlling externally the electrochemical reaction, likewise determining the reaction mechanism and kinetics through current and potential measurements.

1.3 Scope of the study

Chapter two presents a comprehensive review of several immobilized bimetallic systems. The underlying mechanisms of electrophoresis, diffusiophoresis and diffusioosmosis are discussed. The state of the art involving the fuel choice, electrode reactivity, and potential applications are analyzed. The power conversion efficiency for several bimetallic electrocatalytic systems is also evaluated and compared.
Chapter three provides a detailed numerical modelling framework that offers more insight and interpretation to the experimental observations. A 2D model was formulated based on the Poisson-Nernst-Planck and Stokes' equations, which are all coupled. The model accounts for water equilibrium reactions

involving the dissociation and recombination of the ionic constituents of water (H^+ and OH^-), as well as acid equilibrium reaction that occurs due to the adjustment of pH of the bulk solution. The numerical simulations yield predictions on the impact of key parameters on the surface-reaction driven flow.

Experimental and numerical results that focus on the key elements that control the overall mass transport characteristics are presented in chapter four. The induced potential and catalytic current are measured electrochemically and analyzed. ERDF is visualized and quantified using particle tracking methods. Numerical simulations are presented that highlight the interplay between the reactivity of the electrodes, which are characterized by the dimensionless Damköhler numbers, with the induced fluid flow.

Under certain reactive conditions described by the anodic Damköhler number, the electrocatalytic reaction driven flow becomes fully reversed and is driven from the cathode (gold) to the anode (platinum). The origin and dynamics of this flow reversal form the subject matter in chapter five. The reaction-induced proton gradient, which serves as the basis of electrocatalytic actuation, is experimentally investigated using fluorescence lifetime imaging microscopy. A numerical analysis that investigates the proton gradient dynamics under different regimes and their consequences for the electro- diffusiokinetic phenomena is presented.

Chapter six addresses the colloidal aggregation phenomena that are observed at the junction of the connected electrodes. The aggregation which is primarily controlled reaction-induced electric field and indirectly influenced by the induced flow will be analyzed and the underlying mechanism will be expanded on.

Finally, chapter seven summarizes the findings of the overall study and provides my perspective towards current and future research in the subject of ERDF.

References

[1] Hey, A. [2018]. *Feynman And Computation*, CRC Press.

[2] Ismagilov, R. F., Schwartz, A., Bowden, N. and Whitesides, G. M. [2002]. Autonomous movement and self-assembly, *Angewandte Chemie International Edition* **41**(4): 652–654.

[3] Keh, H. J. and Hsu, L. Y. [2007]. Diffusioosmosis of electrolyte solutions in fibrous porous media, *Microfluidics and Nanofluidics* **5**(3): 347–356.

[4] Keh, H. J. and Wu, J. H. [2001]. Electrokinetic flow in fine capillaries caused by gradients of electrolyte concentration, *Langmuir* **17**(14): 4216–4222.

[5] Kline, T. R., Paxton, W. F., Wang, Y., Velegol, D., Mallouk, T. E. and Sen, A. [2005]. Catalytic micropumps: microscopic convective fluid flow and pattern formation, *Journal of the American Chemical Society* **127**(49): 17150–17151.

[6] Mallouk, T. E. and Sen, A. [2009]. Powering nanorobots, *Scientific American* **300**(5): 72–77.

[7] McDermott, J. J., Kar, A., Daher, M., Klara, S., Wang, G., Sen, A. and Velegol, D. [2012]. Self-generated diffusioosmotic flows from calcium carbonate micropumps, *Langmuir* **28**(44): 15491–15497.

[8] Mirkovic, T., Zacharia, N. S., Scholes, G. D. and Ozin, G. A. [2010]. Nanolocomotion—catalytic nanomotors and nanorotors, *Small* **6**(2): 159–167.

[9] Pantaloni, D., Clainche, C. L. and Carlier, M.-F. [2001]. Mechanism of actin-based motility, *Science* **292**(5521): 1502–1506.

[10] Paxton, W. F., Kistler, K. C., Olmeda, C. C., Sen, A., St. Angelo, S. K., Cao, Y., Mallouk, T. E., Lammert, P. E. and Crespi, V. H. [2004]. Catalytic nanomotors: Autonomous movement of striped nanorods, *Journal of the American Chemical Society* **126**(41): 13424–13431.

[11] Sengupta, S., Ibele, M. E. and Sen, A. [2012]. Fantastic voyage: Designing self-powered nanorobots, *Angewandte Chemie International Edition* **51**(34): 8434–8445.

[12] Soong, R. K., Bachand, G. D., Neves, H. P., Olkhovets, A. G., Craighead, H. G. and Montemagno, C. D. [2000]. Powering an inorganic nanodevice with a biomolecular motor, *Science* **290**(5496): 1555–1558.

[13] Sánchez, S. and Pumera, M. [2009]. Nanorobots: The ultimate wireless self-propelled sensing and actuating devices, *Chemistry – An Asian Journal* **4**(9): 1402–1410.

[14] Tourmente, M., Varea-Sánchez, M. and Roldan, E. R. S. [2018]. Faster and more efficient swimming: energy consumption of murine spermatozoa under sperm competition†, *Biology of Reproduction* **100**(2): 420–428.

[15] Wang, J. [2009]. Can man-made nanomachines compete with nature biomotors?, *ACS Nano* **3**(1): 4–9.

[16] Weibel, D. B., Garstecki, P., Ryan, D., DiLuzio, W. R., Mayer, M., Seto, J. E. and Whitesides, G. M. [2005]. Microoxen: Microorganisms to move microscale loads, *Proceedings of the National Academy of Sciences* **102**(34): 11963–11967.

[17] Zhou, C., Zhang, H., Li, Z. and Wang, W. [2016]. Chemistry pumps: a review of chemically powered micropumps, *Lab Chip* **16**: 1797–1811.

Chapter 2

Immobilized bimetallic motors

2.1 Introduction

In this chapter, the progress on the design of immobilized electrocatalytic systems is reviewed. The basic mechanisms that concern operation of these systems are discussed, the state of the art techniques for characterizing the electrokinetic properties are presented, and their integration into "real-world" applications are highlighted. The power conversion efficiencies for different systems are evaluated, compared, and analyzed as will be shown in a later section.

2.2 Working Principle

A typical catalytic bimetallic motor consists of a galvanic couple involving two metals that catalyze the decomposition of a water soluble fuel, which powers its directional motion. Such a metallic duo can be selected depending on its reactivity, with either of the metals assuming the anodic or cathodic role depending on its mixed potential [44]. A platinum and gold pair has emerged as a suitable choice for catalytic bimetallic motor design in several studies because they offer a strong resistance to corrosion, and catalyze the decomposition of hydrogen peroxide via oxidation and reduction pathways (Fig 1.2).
The electrochemical reaction involving hydrogen peroxide proceeds, with oxidation occurring at the platinum anode yielding protons, electrons and oxygen (2.1), and reduction reaction taking place at the gold cathode where protons are consumed and water is formed (2.2).

$$H_2O_2 \rightarrow 2H^+ + O_2 + 2e^- \tag{2.1}$$

$$H_2O_2 + 2H^+ + 2e^- \rightarrow H_2O \tag{2.2}$$

The production and consumption of protons leads to the establishment of a proton gradient along the bimetallic electrode. The resulting ion and electron flux constitutes an electrical body force that phoretically drives the bimetallic motor. The motion of the bimetallic motor is created by two main forms of field acting along the electrode-electrolyte interface, which involves both the electric and concentration gradient [3].

2.2.1 Self-electrophoresis

Self-electrophoresis has been identified as the underlying mechanism for the electrokinetic process involving synthetic motors that were modeled after bio-

logical motors [3]. Peter Mitchell [27] laid the theoretical framework by identifying the existence of a self-induced potential and electric gradient on the surface of a bacterium that powers its motion. Previously, the locomotion of catalytic bimetallic motors was attributed to mechanisms based on interfacial tension [22] and oxygen bubble recoil [33]. Later, a consensus was reached on self-electrophoresis as the main driving force, which is controlled by localized concentration and electrical gradients and fueled by the chemical conversion of the surrounding electrolyte. The phoretic movement of the bimetallic motor is powered by a self-induced electric field in conjunction with the proton gradient that is generated during the electrochemical reaction, hence the name self-electrophoresis.
Self-electrophoresis was initially demonstrated using striped bimetallic motors by Paxton et al. [35], that catalyzes the decomposition of hydrogen peroxide through surface reactions and creates an electric field $\mathbf{E}$ that propels the movements of the bimetallic motors (Fig. 2.1). The resulting electric field can induce particle migration whose velocity $\mathbf{u}_{ep}$ can be expressed by the Helmholtz-Smoluchowski equation

$$\mathbf{u}_{ep} = \mu_e \mathbf{E} \tag{2.3}$$

where μ_e is the electrophoretic mobility of the particle. In addition to the electric force, the bimetallic motors also experience a viscous drag force (F_D) that is exerted by the fluid medium during its motion. The drag force depends on the shape of the bimetallic motor [42]. For a spherical bimetallic motors, the average drag force is expressed as

$$\mathbf{F}_D = 6\pi\eta r \mathbf{v}_{eph} \tag{2.4}$$

while for cylindrical motors, the average drag force is

$$\mathbf{F}_D = \frac{2\pi\eta L}{ln\frac{L}{R} - 0.72}\mathbf{v}_{eph} \tag{2.5}$$

where η is the viscosity of the fluid, $\mathbf{v}_{eph}$ is the rod's electrophoretic velocity and r is the radius of the spherical micromotor, L and R are the length and radius of the cylindrical micromotor respectively. The self-electrophoretic mechanism requires a net charged layer surrounding the rod, generated by the electrochemical reaction that generates the asymmetric distribution of charged intermediates whose transport is governed by diffusion, migration, and convective fluxes. The charge density combines with a self-induced electric field

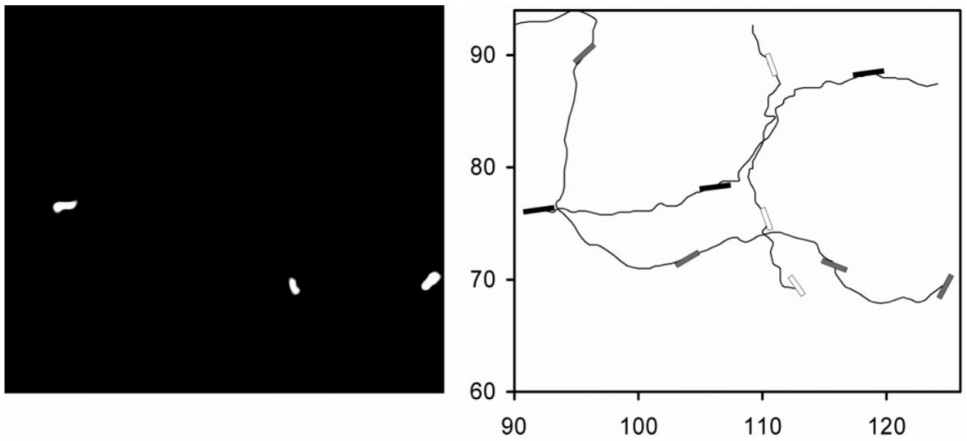

Figure 2.1: Locomotion and trajectories of stripped nanorods through self-electrophoresis in hydrogen peroxide. Reprinted with permission from [35]. Copyright 2004 American Chemical Society.

to create a body force that powers the rod movement [10]. These fields which are coupled can be solved numerically [31]. Moran et al. [28] developed a comprehensive self-electrophoretic numerical framework for a bimetallic motor by solving the coupled Poisson-Nernst-Plank and Stokes equations, where the surface reaction and fluxes can be accounted for using the simplified Frumkin corrected Butler- Volmer equations. The velocity of the bimetallic motor showed dependence on several parameters including the concentration of the fuel and conductivity [30].

2.3 Immobilized bimetallic motors

Kline et al. [22], inspired by Paxton's Au-Pt bimetallic motors [35], patterned a Au-Ag bielectrode on a substrate and contacted this with a hydrogen peroxide solution. This configuration immobilizes the bimetallic motor and restricts its motility during the electrochemical reaction with hydrogen peroxide. Based on the principle of Galilean relativity, a fluid flow was generated within the immediate surroundings of the bielectrode system. The immobilized bimetallic motor is also termed a micropump, due to its fluid pumping capability. The interfacial flow was visualized using tracer particles. The particle velocity

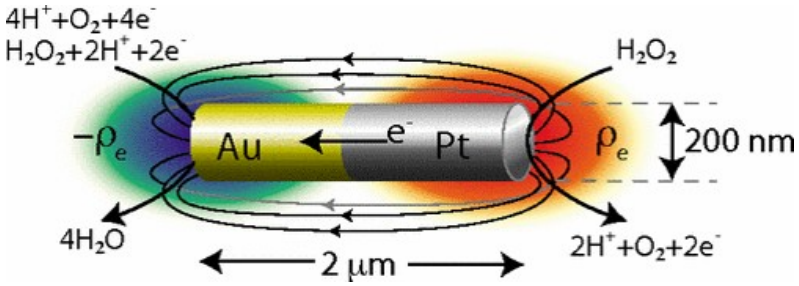

Figure 2.2: Schematic diagram of Pt-Au nanorod, showing the induced electric field (black streamlines) and the charge density (red and blue color map) generated during self-electrophoresis. Adapted with permission from [28]. Copyright 2010 The American Physical Society.

consists of the electrophoretic component that is convoluted with the electroosmotic velocity which has to be decoupled, hence they determined the electric field magnitude from current measurements (approximately 4.3 V/cm) and estimated the electroosmotic velocity based on the Helmoltz Smoluchowski equation

$$\mathbf{u}_{es} = -\frac{\varepsilon}{\eta}\zeta_m \mathbf{E} \tag{2.6}$$

where ζ_m is the zeta potential of the metal. The flow is driven by a self-induced electric field, generated by proton currents during the electrochemical reaction, and is referred to as self-electroosmosis. The characterization of these key elements, including the fluid are discussed in the next sections.

2.3.1 Numerical modelling

The electrokinetic modeling of an immobilized bimetallic motor has been adapted from earlier studies on micro/nanomotors whose locomotion is described by the Poisson-Nernst-Planck and Stokes equations [21, 28, 32, 43]. The Poisson equation accounts for the electrostatic field by relating the ionic species charge density to the electric potential ϕ whose negative gradient gives the induced electric field $\mathbf{E}$.

$$-\varepsilon\nabla^2\phi = \rho_e \tag{2.7}$$

where $\rho_e = F\sum_i z_i c_i$ is the space charge density and ε is the permittivity of the liquid. The Nernst-Planck equation combines the diffusive and electromigration fluxes in relation with the convective flux to describe the ionic species

transport.

$$\mathbf{u} \cdot \nabla c_i = \nabla \cdot (D_i \nabla c_i + z_i F \mu_i c_i \nabla \phi) \tag{2.8}$$

c_i is the concentration of ionic species with valence z_i, diffusivity D_i that is related to the ionic mobility μ_i through the Einstein equation $D_i = \mu_i RT$, with R is the universal gas constant and T is the absolute temperature. The continuity and Stokes equations resolve the induced fluid flow for an incompressible fluid under steady state conditions.

$$\nabla \cdot \mathbf{u} = 0 \tag{2.9}$$

$$-\nabla p + \eta \nabla^2 \mathbf{u} + \rho_e \nabla \phi = 0 \tag{2.10}$$

where p is the pressure, η is the fluid viscosity, and $\rho_e \nabla \phi$ is the electrical body force from the combined charge density and electric field.

Kline et al. [21] described the motion of tracer particles driven by the induced flow by using the electrokinetics based on the aforementioned governing equations. The particle velocities were modeled by solving simultaneously, partial differential equations that describes ion transport, particle motions, flow and electric field. The model captures the electric field that mediates the movement of the charged tracers and agrees with observations of Paxton et al. [34] on particle motions driven by the interdigitated electrode.

Esplandiu et al. [12] investigated the key parameters such as the ionic strength, zeta potential and reaction kinetics that affect the performance of a Au-Pt and hydrogen peroxide electrocatalytic system. The electric field, which is primarily induced by the proton gradient was ascertained as the major driving force for the electroosmotic flow. On the other hand, they established that electric field and fluid flow are mainly controlled by ionic strength, which contrasts early assumptions of the fluid conductivity as the major influence. Their study was extended to the reaction-induced proton gradient [13], where they solved numerically the proton concentration profile across the electrodes. Their numerical result showed good agreement with their experimental measurement.

Davidson et al. [8] developed an analytical model for a Pt-Au H_2O_2 based system that captures the induced potential and fluid flow without the need for any fitting parameters or simulations. The model demonstrated good agreement with their direct numerical simulations over a broad range of Damköhler numbers. However their model only considers the transport H^+ and OH^- ionic species within pure water. In practical sense other species may be present in water due to the contamination or the dissolution of carbonic acid. The

inclusion of these additional species may impact the electrocatalytic process through the pH or conductivity.

2.3.2 Electrochemical characterization

The connected electrodes compare to a simple electrochemical cell that exhibits potentiometric or amperometric responses during electrochemical reactions. Two major indices used in characterizing the electrochemical reactions are the bimetallic potential and the catalytic current.
The catalytic current that travels between the connected electrodes has been measured directly with an ammeter for a Pt-Au and hydrogen peroxide catalytic system [34] (Fig. 2.3). For this test configuration, the platinum electrode was short-circuited with gold through an ammeter and introduced into hydrogen peroxide solution. The electrochemical reaction proceeds and is indicated by a steady state electric current density. From the measured current, the decomposition of H_2O_2 was established as the dominant reaction that triggers the electrokinetic output of a bimetallic system.

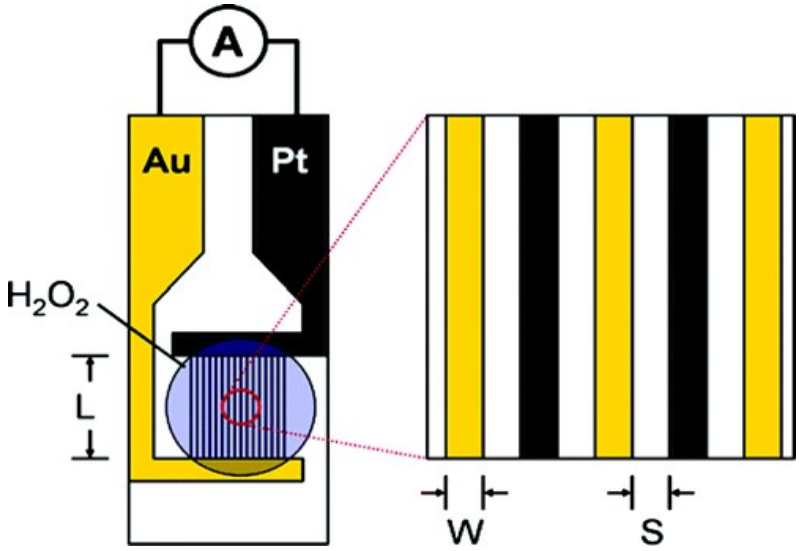

Figure 2.3: Schematic of a Pt-Au interdigitated electrode setup used in measuring the electrocatalytic current with an ammeter. Adapted with permission from [34] copyright 2006, American Chemical Society.

Another method of measuring the catalytic current is from the so-called Tafel

curve, obtained from voltammetry experiments [44]. The voltammetry experiments can be performed using either cyclic or linear sweep voltammetry test protocols, where individual electrodes are subjected to applied potentials in the oxidation or reduction range. The resulting electric current is plotted in logarithm form against the electric potential that gives the Tafel curve. The current measured in this way provides information on the reaction kinetics and ion fluxes. Both the catalytic current and bimetallic potential can be directly inferred from the intersection point that is bounded by the mixed potential for both electrodes from the Tafel curve. The mixed potential is the potential at which the net current is zero, where the transition from oxidation to reduction and vice versa occurs. This is indicated by a change in sign convention for the current (either positive or negative). The bimetallic potential results to regulate the reaction rate through current conservation by adjusting the proton concentration on the surface of the electrodes [8]. The bimetallic potential can also be measured directed from the connected metals as a working electrode against a reference electrode [4, 17].

Farniya et al. [13] has also explored an unconventional way of determining the bimetallic potential, by integrating the electric field obtained from tracking positive and negative charged particles driven by a disk shaped Pt-Au bimetallic micropump. This approach determines the tangential potential ϕ_{tan}, which is the the variation of the electric potential along the surface of the electrode just outside the double layer. This differs from the electrochemical measurement where the electric potential is measured between the surface of the electrodes and the bulk.

The electric field is the gradient of the induced potential, whose directionality is defined by the proton flux and gradient. This has been demonstrated experimentally using negatively charged particles that become electrostatically trapped on the charged electrodes [39]. It was previously reported that the electric field originates from the anode and points towards the cathode [13, 12]. However, due to bulk electrolyte pH variation that impacts the proton gradient, the electric field can originate from either of the electrodes. The electric field can be experimentally determined from the measured catalytic current according to Ohm's law $\mathbf{E} = i/\sigma$, where i is the current density and σ is the conductivity of the electrolyte [34]. Another way to experimentally quantify the electric field is by using the one-particle correlation provided the electric field is determined from simulations, or the two-particle correlation [13] involving two different types of particles similar in size and having different surface charges within the same experimental condition. The different surface charges,

expressed by their corresponding zeta potentials result in distinct velocities, $\mathbf{u}$, from which the electric field magnitude can be estimated for a Pt-Au H_2O_2 system within some degree of uncertainty, by using the following equation:

$$\mathbf{E} = \frac{\eta(\mathbf{u}_{p_+} - \mathbf{u}_{p_-})}{\varepsilon(\zeta_{p_+} - \zeta_{p_-})} \tag{2.11}$$

where $\mathbf{E}$ is the electric field magnitude, ζ_{p_+} and ζ_{p_-} are the zeta potentials for the positive and negative tracer particles respectively, η is the fluid viscosity, ε is the permittivity of the fluid.

2.3.3 Proton gradient

Protons are generated during the oxidation reaction at the anode and migrate to the cathode where they are consumed by the reduction reaction. Over time the proton flux results in a steady state gradient that establishes fluid pumping via an electrical body force. This has been studied and confirmed using numerical modelling [8, 12, 29]. The chemomechanical actuation is not limited to hydrogen peroxide fuel based systems, but also hydrazine [17], and iodine [46] based systems, whose chemical conversion generates an ionic gradient of charged intermediates that triggers catalytic flow.

Fluorescence microscopy has emerged as a useful tool for experimentally probing the local proton dynamics generated during electrochemical reactions. Fluorescence microscopy has been used in the past to study heterogeneous reaction, water splitting and other dynamics that occurs at an electrode region [9, 7, 11, 25]. The major approach involves a label, a fluorescent agent or fluorophore, that is illuminated with a lightsource of a certain wavelength. The fluorophore becomes excited and emits light of an intensity that depends on the reactive processes that take place at the vicinity of an electrode. Based on this principle, Farniya et al. [13] locally probed the proton gradient for a Pt-Au H_2O_2 system, using confocal fluorescence microscopy in conjunction with Pyranine, a pH-sensitive dye molecule that exhibits dual-wavelength spectra and permits fluorescent ratiometric pH. The fluorescence intensity of the dye depends on the local proton concentration and it spatially resolves the proton concentration across the bielectrode during the electrochemical reaction (Fig. 2.4).

Fluorescence lifetime imaging (FLIM) is another fluorescence based approach that has been used in characterizing the proton gradient near the electrode surfaces. In this method, the lifetime of a suitable fluorophore is used in probing the proton distribution generated during the catalytic reaction. The lifetime

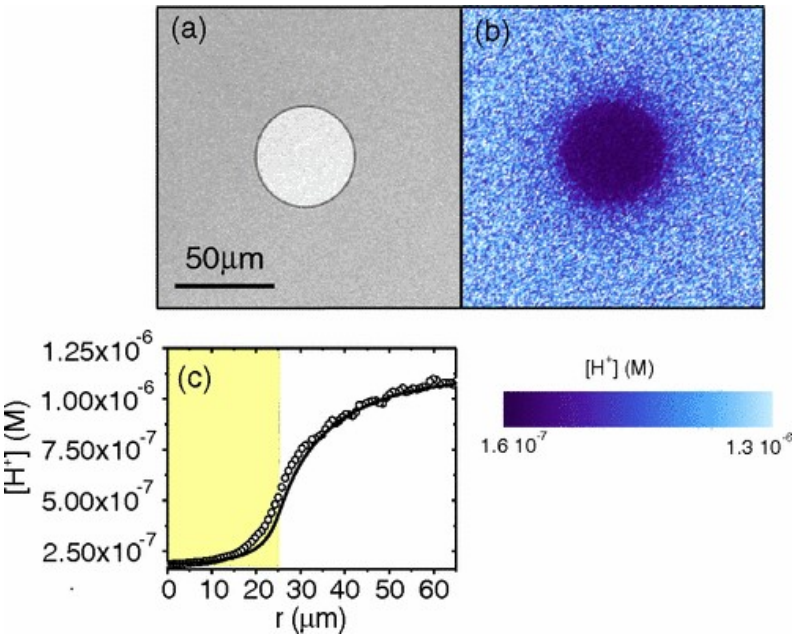

Figure 2.4: (a) Reflectance image of Au-Pt micropump involving no electrochemical reaction in the absence of hydrogen peroxide. (b) Fluorescence image that highlights the proton gradient across the bielectrode during electrochemical reactions (c) The concentration of proton along the radius of the Au-Pt bielectrode (circular form). Adapted with permission from [13]. Copyright 2013 American Physical Society.

is the measure of time for the excitation of a fluorophore to its emission. A key advantage of the FLIM technique lies in its robustness as a result of its relative lifetime insensitivity to variations in the dye concentration, excitation light intensity, and photobleaching [24]. In this thesis, LysoSensor probe was used in conjunction with FLIM to visualize and quantify the proton gradient for a Pt-Au and hydrogen peroxide based system. The LysoSensor probe spontaneously accumulates within the proton enriched regions and yields a higher lifetime signal as a result of the decreased quenching of their protonated weak basic chain [26, 19]. Using pH versus lifetime calibration, the proton distribution was quantified and confirmed the enrichment of protons at the anode and depletion at the cathode during the electrochemical reaction.

Despite these advancements, both fluorescence techniques have a common limitation, which is their inability to resolve the proton gradients at near-

surface regions typically less than 200 nanometers. Numerical study has shown that the proton gradient within the first few nanometers near the bielectrode surface is steeper than the actual quantification offered by FLIM and other techniques. One way to circumvent this is to use a Total internal reflection fluorescence system (TIRF). TIRF is a non-invasive technique that can be coupled with either confocal fluorescence microscopy or FLIM to selectively image fluorescent dye molecules within an evanescent field at the electrode surface region, which is typically less than 200 nm [14].

2.3.4 Electrohydrodynamic phenomena

Immobilized bielectrodes with heterogeneous catalytic properties generate convective flow patterns on a lengthscale of the heterogeneities themselves [17, 22, 34]. The flow pattern is consistent with an electroosmotic flow where fluid is driven from the anode to the cathode and recirculated to the upper region within a confined space due to continuity. The direction of the flow can be reversed from the cathode to the anode. This can be reaction-driven under lower anodic reactive regimes [4, 8] or by surface modification of the electrodes that varies the zeta potential and impacts the flow direction according to the Helmholtz-Smoluchowski formula [40].
The flow field is commonly visualized with tracer particles that passively follow the fluid flow. An example of a commonly used tracer particle is polystyrene beads, which can be functionalized with amine or carboxylate to tune the zeta potential of the particle. Such particles have been used to quantify the fluid velocity magnitude. The observed particle velocity magnitude $\mathbf{u}_p$ consists of the fluid flow component $\mathbf{u}_f$ combined with the electrophoretic velocity of the particle $\mathbf{u}_{ep}$. The electrophoretic velocity is generated due to the interaction between the surface charge of the particles and the induced electric field. Decoupling these two velocity components will yield the actual magnitude of catalytically induced fluid flow. This can be achieved by using the two-particle correlation that involves the use of two tracers having different electrophoretic mobilities under the exact experimental conditions [12, 41].

$$\mathbf{u}_{p_+} = \frac{\varepsilon}{\eta}\zeta_{p_+}E + \mathbf{u}_f \tag{2.12}$$

$$\mathbf{u}_{p_-} = \frac{\varepsilon}{\eta}\zeta_{p_-}E + \mathbf{u}_f \tag{2.13}$$

$$\mathbf{u}_f = \frac{\zeta_{p_+}\mathbf{u}_{p_-} - \zeta_{p_-}\mathbf{u}_{p_+}}{\zeta_{p_+} - \zeta_{p_-}} \tag{2.14}$$

The flow magnitude demonstrates a quasi-linear relationship with the electrolyte concentration [4], and mostly becomes saturated at higher concentrations [12]. The particle velocity encompasses both electrophoretic and diffusiophoretic components (see section 1.1).

2.3.5 Electrode choice and combination

The selection of suitable metals for a bimetallic system is integral to electrocatalytic conversion and the induced flow performance. The electrode pairing and combination under favorable electrolyte conditions can enhance the electrochemical reaction that generates the gradients necessary for chemomechanical actuation.
The electrode reactivity was estimated with the dimensionless Damköhler number Da whose variation creates reaction regimes that impact the flow output by several orders of magnitude [8]. The redox reaction involving the decomposition of H_2O_2 can occur preferentially on either of the electrodes depending on their mixed potential. Usually the metal with the higher mixed potential acts as the cathode while the other metal assumes the anodic role [45].
Wang et al. [45] investigated different electrode combinations to determine the most reactive pair that enhances electrocatalytic conversion. The metals that were considered are Rh, Pt, Ni, Pd, Au, Ru, Ag and Co, which are mostly transition metals. This class of metals are preferred because they are highly resistant to corrosion. The experiments were conducted using 5 wt. % H_2O_2 solution. The Rh-Au pair demonstrated the highest speed output followed by Pt-Au. However, in some cases Ru might become oxidized under high peroxide condition [1, 23] which impedes the catalytic activity. Hence the Pt-Au pair was adopted as a popular choice for a bimetallic model system [13, 35]. Ag-Au, Ni-Au, and Au-Co exhibited a lower catalytic performance, which was compounded by the instability exhibited by Co and Ag in hydrogen peroxide, as evidenced by their mixed potential. On the other hand Ni metal is the cheapest of all the aforementioned precious metals, and more work needs to be done to couple a low-cost suitable pair with Nickel that demonstrates good catalytic activity.

2.3.6 Fuel choice

Early catalytic micropump designs were fueled by the decomposition of hydrogen peroxide. However, its low conversion efficiency limits its potential for

practical applications [42]. Furthermore, the high rate of bubble nucleation involving oxygen production during oxidation reaction, especially under high concentrations, hinders its advancement for microfluidic-based applications. These challenges have necessitated the search for alternative electrolytes.
Hydrazine derivatives consisting of N_2H_4 and $N_2Me_2H_2$ have been studied in conjunction with Au-Pd bielectrodes [17]. The electrocatalytic mechanism is similar to H_2O_2, where the decomposition of hydrazine creates a gradient of charged intermediates that drives the fluid motion. Furthermore, the fluid flow direction was governed by the hydrazine derivative that powers the system. However hydrazine pose some safety issues, as its highly flammable, toxic and corrosive. The use of environmentally friendly electrolyte are more desired for electrocatlytic applications.
Wong and Sen [46] engineered a silver-platinum micropump that uses iodine as fuel. The electrochemical reaction mechanism proceeds with oxidation occurring at silver to yield Ag^+ and electrons. The electrons are transferred to platinum, while the reduction of iodine at platinum results to iodide ions that recombines with the silver ions to form AgI. A gradient of cations is established that generates the electric field that drives fluid flow. The reaction is reversible and the system is highly efficient and superior in performance than other forms of fuel based systems. Furthermore, the pumping speed can be enhanced by exposure to UV light that regenerates AgI to Ag.

2.3.7 Polyelectrolyte effects

The modification of the metallic surface properties has been explored to enhance the overall electrocatalytic output. Subramanian and Catchmark [40] modified the surface charge of a Au-Ag H_2O_2 system to control the direction of the induced fluid flow. The surface of the gold electrode was functionalized with carboxylic acid SAMs to yield a zeta potential of –60 mV or amine-terminated SAMs to obtain a zeta potential of 50 mV. The negatively charged gold surface resulted in a normal electroosmotic flow pattern where flow is driven from Au to Ag, while the flow pattern is reversed for the positively charged surface.
The possibility of enhancing the electrokinetic effects of Pt-Au bielectrode with Nafion was tested in the early stages of this work. Nafion membrane has a proton-exchange capability that excludes anionic species from reaching the electrode surface, thereby enabling its selectivity to cations. The goal here was to augment the proton supply needed for catalytic activities since the amount being generated during the electrochemical anodic reaction involving hydro-

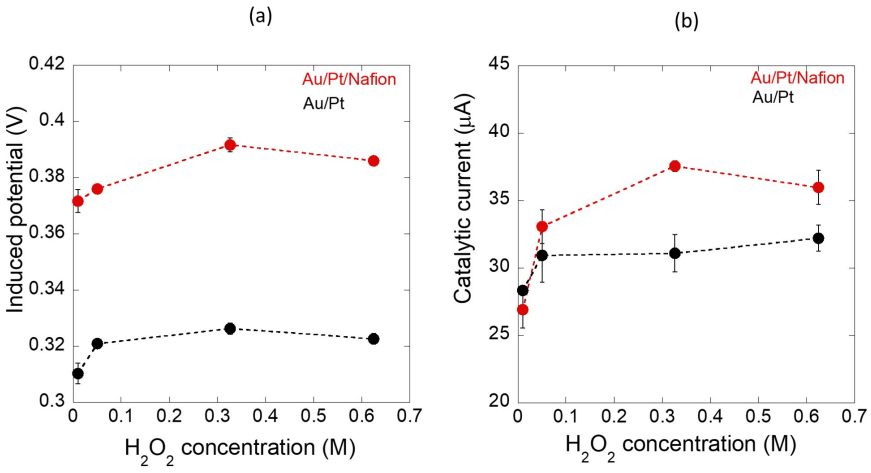

Figure 2.5: Comparison on electrocatalytic performance for Pt-Au bielecrode with and without Nafion surface coating in terms of (a) Potentiometric response (b) Amperometric response

gen peroxide is limited. A potentiometric enhancement was recorded that is associated with the Donnan potential generated by the Nafion membrane, together with a boost in catalytic current (see Figure 2.5)

2.3.8 Power Conversion efficiency

In this section, the fluid flow pumping performance for several immobilized electrocatalytic systems are evaluated. This is based on the conversion efficiency η_e, that relates the mechanical power P_{mech} output to the total chemical power input P_{chem}

$$\eta_e = \frac{P_{mech}}{P_{chem}} \tag{2.15}$$

where P_{mech} is defined as

$$P_{mech} = \mathbf{F}_{viscous}\mathbf{u}_f \tag{2.16}$$

$\mathbf{F}_{viscous} = \tau A$ is the viscous force associated to the catalytically induced flow $\mathbf{u}_f$ moving relative to the bielectrode, and is expressed as the product of the shear stress $\tau = \eta\dfrac{d\mathbf{u}}{dy}$ and the area A of the bielectrode. η is the dynamic

viscosity of the fluid medium. The total chemical power input P_{chem} (kJ/s) is defined as

$$P_{chem} = k_{fuel}\Delta G \tag{2.17}$$

where k_{fuel} is the rate of fuel consumption in mol/s. The fuels that were considered are hydrogen peroxide (H_2O_2) and Iodine (I_2). For the purpose of simplicity, n_{fuel} was determined based on the instantaneous consumption of the aforementioned fuel during electrochemical conversion. ΔG is the Gibbs free energy for the fuel conversion in kJ/mol expressed as

$$\Delta G = -nFE_{cell} \tag{2.18}$$

where n is the number of electrons transferred and F is the Faraday constant (96485 C/mol) and E_{cell} is the cell potential for the relevant electrochemical reaction. We compared the conversion efficiency for several immobilized

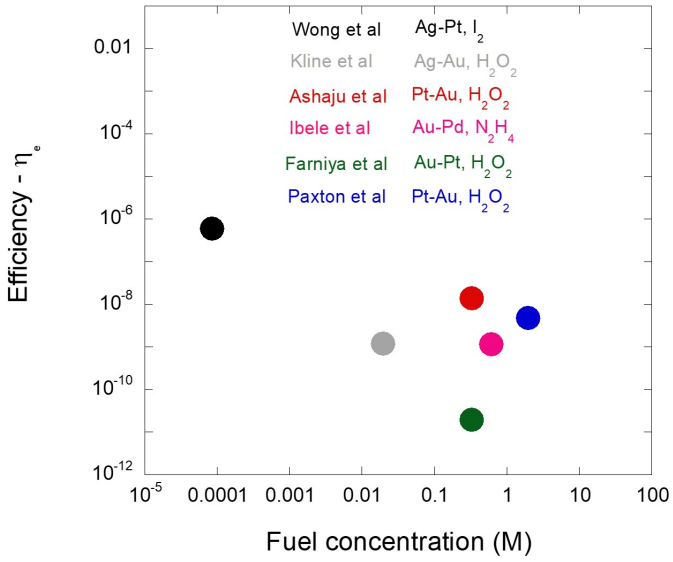

Figure 2.6: Power conversion efficiency for immobilized electrocatalytic systems at different fuel concentrations.

systems based on factors including electrode combination and electrolyte (see Fig. 2.6). The Ag-Pt I_2 bimetallic system powered by iodine solution appears relatively to be the most efficient, as it requires lesser chemical power input for the energy transduction process. Moreover, the flow velocity generated

by this system can be further enhanced using UV-light that influences the rate of the redox reaction occurring at the electrode-electrolyte interface. In general, a lower overpotential contributes to an efficient electrochemical conversion, which may be influenced by the electrolyte properties such as pH and concentration in conjunction with the electrode reactivity. The cell potential associated with redox half-reactions driven by the Ag-Pt I_2 bimetallic system is low compared to that of peroxide-based systems, due to a lower thermodynamic potential required for halide fuel conversion.

2.3.9 Applications

The fluid flow output in conjunction with the induced electric field serves as the basis upon which relevant applications involving immobilized electrocatalytic systems are developed. Hess and Jun developed a biomimetic membrane pump based on a Pt-Au bimetallic electrode [20]. They deposited Pt and Au on opposite sides of a polycarbonate membrane that generates flow (1 nL s^{-1}) across it, whenever the electrodes are connected. The chemical energy that powers the bielectrode is sourced from the surrounding hydrogen peroxide fuel (Fig. 2.7). Future development of this system is being targeted at compartmentless biofuel cells, where the use of an ion-exchange membrane is eliminated.

Naeem et al. [33] developed an oxygen microbubble generator that is based on Ti/Cr/Pt microtubes. The microtubes are fabricated by rolling up Ti/Cr/Pt nanomembranes that were previously immobilized on a silicon substrate [38]. During the decomposition of hydrogen peroxide, oxygen bubbles are generated and accumulate within the solution due to their buoyancy. The bubble nucleation is controlled by varying the peroxide concentration while surfactants are used in stabilizing the air-liquid interface and increasing the bubble frequency within the microtubes. The oxygen microbubble generator has the potential for oxygen supply in areas where needed.

Colloid crystals are relevant to applications in sensor devices [5, 16, 6] and photonic materials [37, 15, 47]. However, the controlled deposition of colloidal crystals still remains a challenge. Immobilized electrocatalytic microreactors provide a viable route towards reaching this goal [36, 18]. This was demonstrated by Farniya et al.[2] who manipulated and guided the crystallization of colloids, driven by the electrocatalytic reaction involving peroxide on Au-Pt bielectrodes. Furthermore, this process requires no external power source, as is driven primarily by the self-induced electric field that is generated during the electrochemical reaction involving hydrogen peroxide.

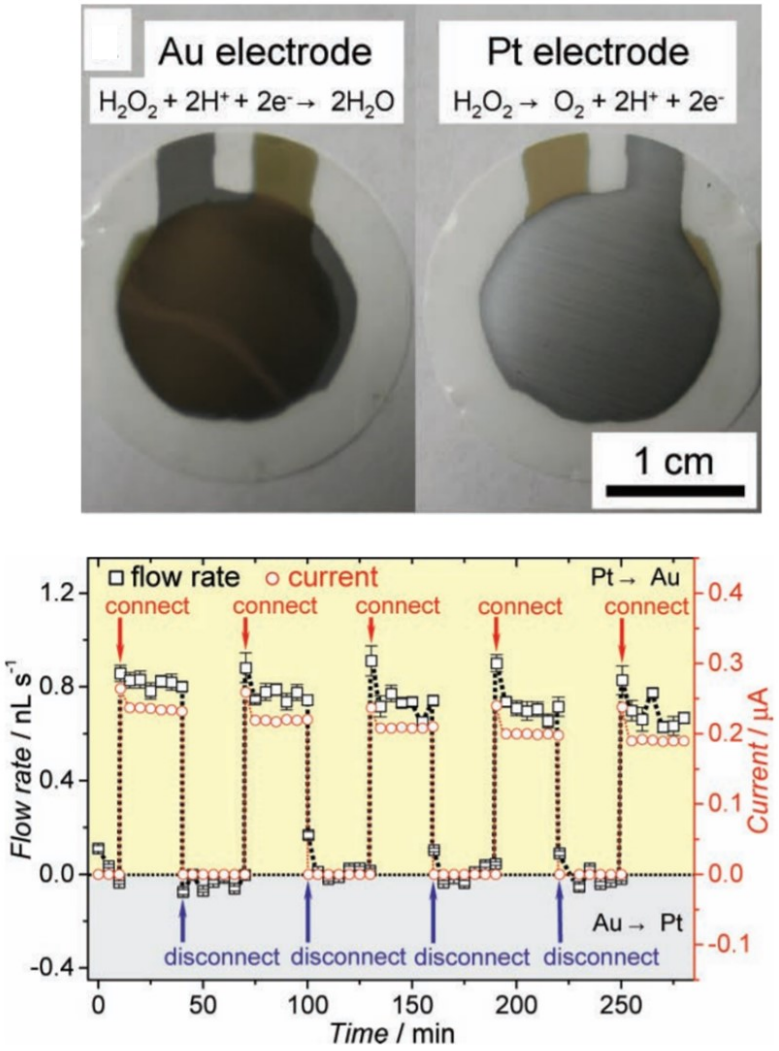

Figure 2.7: (a) A biomimetic pump that consists of platinum and gold electrodes that are deposited on opposite sides of a membrane. (b) Electrocatlytic current and flow magnitude as a function of time during the electrochemical reaction of the bielectrode with hydrogen peroxide solution. Adapted with permission from [20]. Copyright 2010 John Wiley and Sons.

References

[1] Aaltonen, T., Ritala, M., Tung, Y.-L., Chi, Y., Arstila, K., Meinander, K. and Leskelä, M. [2004]. Atomic layer deposition of noble metals: Explo-

ration of the low limit of the deposition temperature, *Journal of Materials Research* **19**: 3353–3358.

[2] Afshar Farniya, A., Esplandiu, M. J. and Bachtold, A. [2014]. Sequential tasks performed by catalytic pumps for colloidal crystallization, *Langmuir* **30**(39): 11841–11845.

[3] Anderson, J. L. [1989]. Colloid transport by interfacial forces, *Annual Review of Fluid Mechanics* **21**(1): 61–99.

[4] Ashaju, A. A., Wood, J. A. and Lammertink, R. G. H. [2021]. Electrocatalytic reaction-driven flow, *Phys. Rev. Fluids* **6**: 044004.

[5] Baksh, M. M., Jaros, M. and Groves, J. T. [2004]. Detection of molecular interactions at membrane surfaces through colloid phase transitions, *Nature* **427**(6970): 139–141.

[6] Ben-Moshe, M., Alexeev, V. L. and Asher, S. A. [2006]. Fast responsive crystalline colloidal array photonic crystal glucose sensors, *Analytical Chemistry* **78**(14): 5149–5157.

[7] Bowyer, W. J., Xie, J. and Engstrom, R. C. [1996]. Fluorescence imaging of the heterogeneous reduction of oxygen, *Analytical Chemistry* **68**(13): 2005–2009.

[8] Davidson, S. M., Lammertink, R. G. and Mani, A. [2018]. Predictive model for convective flows induced by surface reactivity contrast, *Physical Review Fluids* **3**(5): 1–16.

[9] Doneux, T., Bouffier, L., Goudeau, B. and Arbault, S. [2016]. Coupling electrochemistry with fluorescence confocal microscopy to investigate electrochemical reactivity: A case study with the resazurin-resorufin fluorogenic couple, *Analytical Chemistry* **88**(12): 6292–6300.

[10] *Electrophoresis* [2005]. John Wiley Sons, Ltd, chapter 9, pp. 295–361.

[11] Engstrom, R. C., Ghaffari, S. and Qu, H. [1992]. Fluorescence imaging of electrode-solution interfacial processes, *Analytical Chemistry* **64**(21): 2525–2529.

[12] Esplandiu, M. J., Afshar Farniya, A. and Reguera, D. [2016]. Key parameters controlling the performance of catalytic motors, *Journal of Chemical Physics* **144**(12).

[13] Farniya, A. A., Esplandiu, M. J., Reguera, D. and Bachtold, A. [2013]. Imaging the proton concentration and mapping the spatial distribution of the electric field of catalytic micropumps, *Physical Review Letters* **111**(16).

[14] Fish, K. N. [2009]. Total internal reflection fluorescence (tirf) microscopy, *Current Protocols in Cytometry* **50**(1).

[15] Galisteo-López, J. F., Ibisate, M., Sapienza, R., Froufe-Pérez, L. S., Blanco, [U+FFFD] and López, C. [2011]. Self-assembled photonic structures, *Advanced Materials* **23**(1): 30–69.

[16] Holtz, J. H. and Asher, S. A. [1997]. Polymerized colloidal crystal hydrogel films as intelligent chemical sensing materials, *Nature* **389**: 829–832.

[17] Ibele, M. E., Wang, Y., Kline, T. R., Mallouk, T. E. and Sen, A. [2007]. Hydrazine fuels for bimetallic catalytic microfluidic pumping, *Journal of the American Chemical Society* **129**(25): 7762–7763.

[18] Jan, L., Punckt, C., Khusid, B. and Aksay, I. A. [2013]. Directed motion of colloidal particles in a galvanic microreactor, *Langmuir* **29**(8): 2498–2505.

[19] Johnson, I. [2010]. *Molecular Probes Handbook: A Guide to Fluorescent Probes and Labeling Technologies*, Life Technologies Corporation.

[20] Jun, I.-K. and Hess, H. [n.d.]. A biomimetic, self-pumping membrane, *Advanced Materials* **22**(43): 4823–4825.

[21] Kline, T. R., Iwata, J., Lammert, P. E., Mallouk, T. E., Sen, A. and Velegol, D. [2006]. Catalytically driven colloidal patterning and transport, *The Journal of Physical Chemistry B* **110**(48): 24513–24521.

[22] Kline, T. R., Paxton, W. F., Wang, Y., Velegol, D., Mallouk, T. E. and Sen, A. [2005]. Catalytic micropumps: microscopic convective fluid flow and pattern formation, *Journal of the American Chemical Society* **127**(49): 17150–17151.

[23] Krier, C. and Jaffee, R. [1963]. Oxidation of the platinum-group metals, *Journal of the Less Common Metals* **5**(5): 411 – 431.

[24] Lakowicz, J. R. (ed.) [2006]. *Principles of Fluorescence Spectroscopy*, Springer US.

[25] Leenheer, A. J. and Atwater, H. A. [2012]. Imaging water-splitting electrocatalysts with pH-sensing confocal fluorescence microscopy, *Journal of The Electrochemical Society* **159**(9): H752–H757.

[26] Lin, H.-J., Herman, P., Kang, J. S. and Lakowicz, J. R. [2001]. Fluorescence lifetime characterization of novel low-ph probes, *Analytical Biochemistry* **294**(2): 118 – 125.

[27] Mitchell, P. [1972]. Self-electrophoretic locomotion in microorganisms: Bacterial flagella as giant ionophores, *FEBS Letters* **28**(1): 1–4.

[28] MORAN, J. L. and POSNER, J. D. [2011a]. Electrokinetic locomotion due to reaction-induced charge auto-electrophoresis, *Journal of Fluid Mechanics* **680**: 31–66.

[29] Moran, J. L. and Posner, J. D. [2011b]. Electrokinetic locomotion due to reaction-induced charge auto-electrophoresis, *Journal of Fluid Mechanics* **680**: 31–66.

[30] Moran, J. L. and Posner, J. D. [2014]. Role of solution conductivity in reaction induced charge auto-electrophoresis, *Physics of Fluids* **26**(4): 042001.

[31] Moran, J. L. and Posner, J. D. [2017]. Phoretic self-propulsion, *Annual Review of Fluid Mechanics* **49**(1): 511–540.

[32] Moran, J. L., Wheat, P. M. and Posner, J. D. [2010]. Locomotion of electrocatalytic nanomotors due to reaction induced charge autoelectrophoresis, *Physical Review E - Statistical, Nonlinear, and Soft Matter Physics* **81**(6): 1–4.

[33] Naeem, S., Naeem, F., Liu, J., Quiñones, V. A. B., Zhang, J., He, L., Huang, G., Solovev, A. A. and Mei, Y. [2019]. Oxygen microbubble generator enabled by tunable catalytic microtubes, *Chemistry An Asian Journal* **14**(14): 2431–2434.

[34] Paxton, W. F., Baker, P. T., Kline, T. R., Wang, Y., Mallouk, T. E. and Sen, A. [2006]. Catalytically induced electrokinetics for motors and micropumps, *Journal of the American Chemical Society* **128**(46): 14881–14888.

[35] Paxton, W. F., Kistler, K. C., Olmeda, C. C., Sen, A., St. Angelo, S. K., Cao, Y., Mallouk, T. E., Lammert, P. E. and Crespi, V. H. [2004]. Catalytic nanomotors: autonomous movement of striped nanorods, *Journal of the American Chemical Society* **126**(41): 13424–13431.

[36] Punckt, C., Jan, L., Jiang, P., Frewen, T. A., Saville, D. A., Kevrekidis, I. G. and Aksay, I. A. [2012]. Autonomous colloidal crystallization in a galvanic microreactor, *Journal of Applied Physics* **112**(7): 074905.

[37] Rinne, S. A., García-Santamaría, F. and Braun, P. V. [2008]. Embedded cavities and waveguides in three-dimensional silicon photonic crystals, *Nature Photonics* **2**: 52–56.

[38] Solovev, A. A., Sanchez, S., Mei, Y. and Schmidt, O. G. [2011]. Tunable catalytic tubular micro-pumps operating at low concentrations of hydrogen peroxide, *Phys. Chem. Chem. Phys.* **13**: 10131–10135.

[39] Subramanian, S. and Catchmark, J. M. [2007a]. Control of catalytically generated electroosmotic fluid flow through surface zeta potential engineering, *The Journal of Physical Chemistry C* **111**(32): 11959–11964.

[40] Subramanian, S. and Catchmark, J. M. [2007b]. Control of catalytically generated electroosmotic fluid flow through surface zeta potential engineering, *The Journal of Physical Chemistry C* **111**(32): 11959–11964.

[41] Tatsumi, K., Nishitani, K., Fukuda, K., Katsumoto, Y. and Nakabe, K. [2010]. Measurement of electroosmotic flow velocity and electric field in microchannels by micro-particle image velocimetry, *Measurement Science and Technology* **21**(10): 105402.

[42] Wang, W., Chiang, T.-Y., Velegol, D. and Mallouk, T. E. [2013]. Understanding the efficiency of autonomous nano- and microscale motors, *Journal of the American Chemical Society* **135**(28): 10557–10565.

[43] Wang, W., Duan, W., Sen, A. and Mallouk, T. E. [2013]. Catalytically powered dynamic assembly of rod-shaped nanomotors and passive tracer particles, *Proceedings of the National Academy of Sciences* **110**(44): 17744–17749.

[44] Wang, Y., Hernandez, R. M., Bartlett, D. J., Bingham, J. M., Kline, T. R., Sen, A. and Mallouk, T. E. [2006a]. Bipolar electrochemical mechanism for the propulsion of catalytic nanomotors in hydrogen peroxide solutions, *Langmuir* **22**(25): 10451–10456.

[45] Wang, Y., Hernandez, R. M., Bartlett, D. J., Bingham, J. M., Kline, T. R., Sen, A. and Mallouk, T. E. [2006b]. Bipolar electrochemical mechanism for the propulsion of catalytic nanomotors in hydrogen peroxide solutions, *Langmuir* **22**(25): 10451–10456.

[46] Wong, F. and Sen, A. [2016]. Progress toward light-harvesting self-electrophoretic motors: Highly efficient bimetallic nanomotors and micropumps in halogen media, *ACS Nano* **10**(7): 7172–7179.

[47] Zakhidov, A. A., Baughman, R. H., Iqbal, Z., Cui, C., Khayrullin, I., Dantas, S. O., Marti, J. and Ralchenko, V. G. [1998]. Carbon structures with three-dimensional periodicity at optical wavelengths, **282**(5390): 897–901.

Chapter 3

Theory and Numerical modelling

Numerical modelling and simulation provides the framework that bridges the gap between experiments and theory. The goal in this case is to obtain more insights and interpretation of our experimental observations regarding the electrocatalytic system. For this reason, a 2D numerical model was formulated that is based on Poisson-Nernst-Planck and Stokes equation, to resolve the electric and potential fields, the concentration and flux of ionic species with the resulting flow field. The numerical model also accounts for the dynamic zeta potential of individual electrodes that are sensitive to pH variations, likewise the self-ionization of water under bulk conditions.

3.1 Model description

The model development is based on a Pt-Au bimetallic electrode that was fabricated on a glass substrate through photolithography, metal sputtering, and liftoff. The glass substrate was spin-coated with positive photoresist, followed by exposure to UV-light through a photomask and development. Tantalum was pre-sputtered on the substrates to improve adhesion, before depositing platinum and gold metals through DC sputtering (MESA+ nanolab cleanroom in-house equipment,"TCOathy"). The photoresist negative pattern was removed via a liftoff process in acetone. A schematic diagram for the Pt-Au bielectrode is shown in figure 3.1.

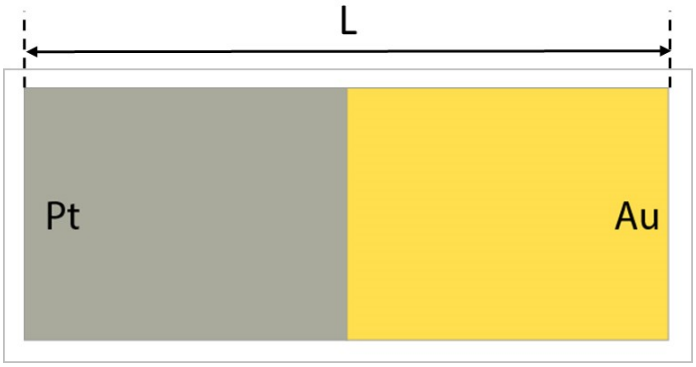

Figure 3.1: Schematics showing the fabricated (b) Pt-Au bimetallic electrode for flow characterization experiments, having a total length L = 10 mm.

For the model, We consider a bielectrode, 10 mm in length L that is fixed at the base of a chamber, 1.5 mm in height H that contains hydrogen peroxide

solution (H_2O_2). We chose a two-dimensional domain with an aspect ratio of $H/L = 0.15$. Although, aspect ratios of $H/L \geq 0.5$ does not affect the surface induced flow velocity, the selected aspect ratio $H/L = 0.15$ is representative of our experimental setup involving the bielectrode (H = 1500 μm, L = 10000 μm).

The bielectrode catalyzes the decomposition of hydrogen peroxide via oxidation and reduction reactions on Pt and Au respectively, leading to the generation and depletion of protons. The resulting proton flux evolves into a steady proton concentration gradient that combines an asymmetric charge distribution and induced electric field into an electrical body force that drives fluid flow. If we consider the presence of only H^+ and OH^- in the solution, due to electroneutrality condition, the bulk concentrations of H^+ and OH^- should be equal. However, the bulk pH of the solution was adjusted during the experimental studies using HCl acid, whose dissociation yields Cl^- as an additional non-reacting species. The ionic composition is expressed through acid/base equilibrium as will be shown in a later section, and accounted for in this model. In the next section, we introduce the differential equations that governs the chemo-mechanical actuation of the bimetallic system.

3.2 Governing equations

3.2.1 Transport of ionic species

The Nernst-Planck equation describes the distribution and mass transport of mobile ionic species (H^+, OH^-, and Cl^-) within a dilute system, and is based on the combination of fluxes including advection, diffusion, and electromigration,

$$\frac{\partial \tilde{c_i}}{\partial \tilde{t}} = -\tilde{\nabla} \cdot (\tilde{c_i}\tilde{\mathbf{u}}) + \tilde{\nabla} \cdot (\tilde{D_i}\tilde{\nabla}\tilde{c_i} + z_i F \tilde{\mu_i}\tilde{\nabla}\tilde{\phi}\tilde{c_i}) \tag{3.1}$$

where the tilde notation indicates dimensional variables. The first term on the right-hand side of equation 3.1 is the advective flux, $\tilde{\mathbf{j}_{advt}}$ which is due to the advective transport of species along with the flowing fluid whose velocity is $\tilde{\mathbf{u}}$, followed by the diffusive flux $\tilde{\mathbf{j}_D}$, which arises due to the gradients of species concentration that are generated during the electrochemical reaction, and is described by Fick's law

$$\tilde{\mathbf{j}_D} = -\tilde{D_i}\tilde{\nabla}\tilde{c_i} \tag{3.2}$$

where $\tilde{D_i}$ is the diffusion coefficient, and $\tilde{c_i}$ is the concentration of i^{th} ionic species. The third term on the right hand side of (3.1) is the electromigration

flux that describes the movement of i ionic species under the influence of a potential gradient. Where $\tilde{\mu}$ is the ionic mobility, which is defined by the Nernst-Einstein equation $\mu = \tilde{D}_i/RT$, R refers to the gas constant (8.314 J/K.mol), and T is the temperature.

3.2.2 Poisson's equation

The electric potential $\tilde{\phi}$ and its gradient, the electric field $\tilde{\mathbf{E}} = -\tilde{\nabla}\tilde{\phi}$, are governed by the Poisson's equation. It is derived from Gauss' law and relates the induced electric potential with the space charge density $\tilde{\rho}_e$ of the ionic species and the permittivity ε of the electrolyte medium ($\varepsilon = 7.10 \times 10^{-10}$ F/m). The Poisson equation also resolves the electric double layer that is formed at the interface between the bielectrode and the electrolyte under the assumption of a constant permittivity for the fluid medium. Poisson's equation is given by

$$\tilde{\nabla}^2\tilde{\phi} = \tilde{\rho}_e/\varepsilon \tag{3.3}$$

where $\tilde{\rho}_e = F\sum_{i=1}^{N} z_i\tilde{c}_i$, F is the Faraday's constant ($F = 96485$ C mol^{-1}) and z_i is the valence of the i^{th} ionic species.

3.2.3 Stokes' equation

The flow induced is governed by the continuity and Stokes equations under the assumption of a steady incompressible flow (equations 3.4 and 3.5). It is typically depicted as Stokes or creeping flow, and it exists under a low Reynolds regime ($Re \ll 1$) where viscous forces dominate over inertial forces. For this reason, the inertial term on the left-hand side of equation 3.5 is neglected ($\rho\frac{\partial \mathbf{u}}{\partial t} = 0$).

$$\tilde{\nabla}\cdot\tilde{\mathbf{u}} = 0 \tag{3.4}$$

$$0 = -\tilde{\nabla}\tilde{p} + \eta\tilde{\nabla}^2\tilde{\mathbf{u}} + \tilde{\rho}_e\tilde{\nabla}\tilde{\phi} \tag{3.5}$$

$\tilde{p}$ represents the pressure, and η is the dynamic viscosity of the fluid. The third term on the right-hand side of equation 3.5 describes the net electrical body that combines the potential gradient $\tilde{\nabla}\tilde{\phi}$ with the charge density $\tilde{\rho}_e$.

3.2.4 Dimensionless equations

The spatial coordinates and other length scales are normalized by the length of the bielectrode L. The velocity is scaled by the diffusion velocity $u_{diff} =$

D_0/L, giving $\mathbf{u} = \tilde{\mathbf{u}}/u_{diff}$, where D_0 is the diffusion coefficient of hydroxide ions ($D_0 = 5.273 \times 10^{-9}$ m^2/s). The concentration of ionic species is normalized by c_0, which is the bulk concentrations for H^+ and OH^- in pure water, giving $c_i = \tilde{c_i}/c_0$. The dimensionless electrostatic potential $\phi = \tilde{\phi}/V_T$ is obtained by scaling with the thermal voltage $V_T = \frac{RT}{F} \approx 0.025$ V, while the time $t = \tilde{t}/t_0$ is scaled by the diffusion time t_0, where $t_0 = L^2/D_0$.
The Stokes and continuity equations in their dimensionless forms are

$$0 = -\nabla p + \nabla^2 \mathbf{u} - \frac{\kappa}{2\epsilon^2}\rho_e \nabla\phi \tag{3.6}$$

$$\nabla \cdot \mathbf{u} = 0 \tag{3.7}$$

The inertial term on the left-hand side of equation 3.6 is neglected under low Reynolds regime ($\frac{1}{\mathrm{Sc}}\frac{\partial \mathbf{u}}{\partial t} = 0$), where Sc is the Schmidt number defined as $\mathrm{Sc} = \eta/\rho D_0$ typically $O(10^3)$, $\kappa = \frac{\varepsilon V_T^2}{\eta D_0} = 0.093$ is the electro-hydrodynamic coupling constant that is fixed by the electrolyte properties. The dimensionless Debye length ϵ is defined as $\epsilon = L_D/L$, where $L_D = \sqrt{\varepsilon V_T/2F\tilde{c}_\infty}$ is the Debye length for a symmetric electrolyte, $\tilde{c}_\infty$ is the bulk proton concentration and ε is the permittivity of water.
The dimensionless Poisson equation becomes

$$-2\epsilon^2 \nabla^2 \phi = \Sigma_i z_i c_i \tag{3.8}$$

while the dimensionless Nernst Planck equation is

$$\frac{\partial c_i}{\partial_t} + \nabla \cdot (\mathbf{u} c_i) = D_i \nabla \cdot (\nabla c_i + z_i c_i \nabla\phi) + R_i \tag{3.9}$$

where $R_i = \mathrm{Da}_b \left(\frac{K_w}{c_\infty^2} - c_{\mathrm{H^+}} c_{\mathrm{OH^-}} \right)$ is a bulk reaction term that enforces water self-ionization for H^+ and OH^-. $K_w = 1 \times 10^{-14}$ mol^2/m^6 is the water equilibrium constant. Da_b is the bulk Damköhler number defined as $\mathrm{Da}_b = k_{rb} L^2 \tilde{c}_\infty / D_0$, with k_{rb} as the water recombination reaction rate constant. The auto-ionization of water will be further discussed in a later section.

3.2.5 Surface reactivity pattern

The surface reactivity is characterized by the dimensionless Damköhler number Da that relates the electrocatalytic reaction timescale to diffusive transport timescale. It can be defined for individual electrodes in the catalytic system as the anodic Da_a and cathodic Da_c Damköhler (3.10) and (3.11) respectively.

Da_a and Da_c directly influence the oxidation and reduction reaction rate respectively, and the variation of these unique Da numbers will create reaction regimes that highlight the role of each electrode on proton generation and depletion.

$$\mathrm{Da}_a = \frac{k_a L c_{\mathrm{H_2O_2}}}{D_+ c_\infty} \tag{3.10}$$

$$\mathrm{Da}_c = \frac{k_c L c_\infty c_{\mathrm{H_2O_2}}}{D_+} \tag{3.11}$$

The anodic and cathodic rate constants are denoted by k_a and k_c respectively, $c_{\mathrm{H_2O_2}}$ is the concentration of hydrogen peroxide, D_+ is the proton diffusivity, and c_∞ is the bulk proton concentration that is set by the pH of the solution.

3.3 Boundary conditions

3.3.1 Electric potential boundary conditions

The electric double layer that is established at the interface between the electrolyte and the bielectrode is assumed to consist of two layers, namely the Stern layer and the diffuse layer (Figure 3.2). The Stern layer model resolves the internal part of the double layer consisting of immobile ions that are adsorbed on the surface of the bielectrode. This inner part is termed the Stern plane and the distance between the Stern plane and the electrode's surface is termed the Stern layer whose thickness is L_{Stn}. The diffuse layer consists of hydrated ions that move freely in the solution, whose distribution is influenced by the balance of electrostatic forces (attraction of counterions and repulsion of coions and to and fro the surface) and diffusion.
The Gouy-Chapman diffuse double layer and the Stern model was used to describe the double layer, by considering the ions as point charges within a constant dielectric medium, whose distribution is based on the Poisson-Boltzmann equation,

$$\varepsilon \nabla^2 \phi = -\sum_{i=1}^{N} z_i e c_\infty \exp(-\frac{z_i e \phi}{k_B T}) \tag{3.12}$$

where k_B is the Boltzmann's constant ($k_B = 1.38 \times 10^{-}23$ J/K), e is the elementary charge on an electron (1.602×10^{-19} C). This approach yields good and quantitative predictions provided the surface potential is below the

thermal voltage $V_T = 0.025$ V and the concentration of the electrolyte is not too high.

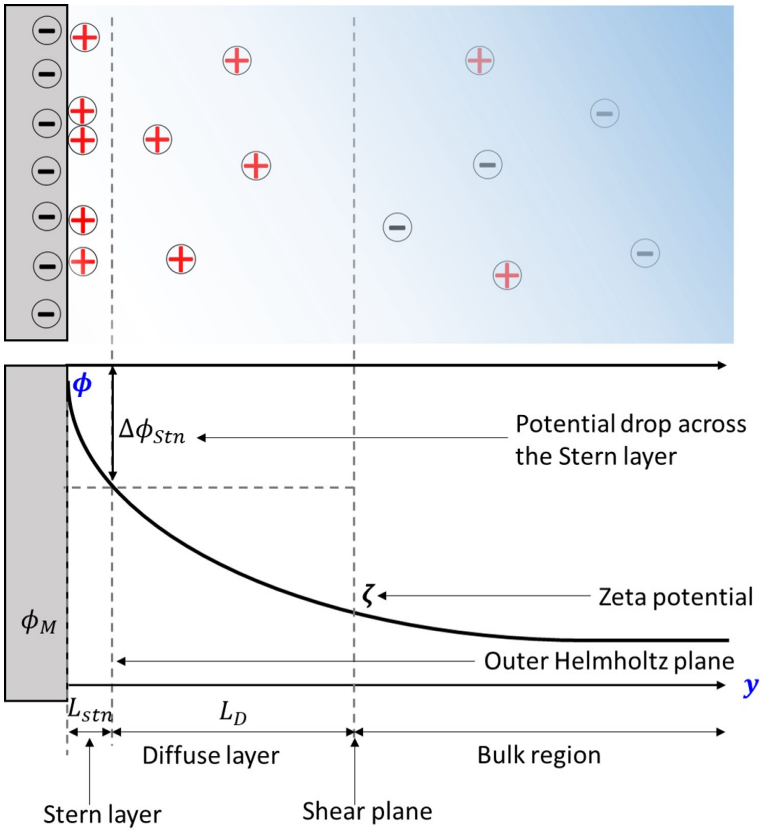

Figure 3.2: Schematics of the electric double layer.

The numerical model resolves the diffuse part of the double layer and considers the outer Helmholtz plane to be the closest point of approach for the ionic species towards the electrodes. The outer Helmholtz plane is located at the outer edge of the stern layer as seen in figure 3.2. The stern layer is accounted for by scaling the potential drop across the Stern layer $\Delta\phi_{Stn}$ with the zeta potential ζ and the ratio between the Stern layer thickness L_{Stn} with the Debye length L_D [5, 4].

$$\Delta\phi_{Stn} \approx \frac{L_{Stn}}{L_D}\zeta. \tag{3.13}$$

The potential drop across the stern layer $\Delta\phi_{Stn}$ is defined as

$$\Delta\phi_{Stn} = \zeta - \phi_{electrode}. \tag{3.14}$$

For an electrolyte having a low salt concentration, the Debye length, L_D is usually tens or hundreds of nanometers while the Stern layer thickness, L_{Stn} is typically less than 1 nanometer. As a result, $L_{Stn}/L_D \ll 1$ and $\Delta\phi_{Stn}$ becomes negligible. Hence, equation 3.14 becomes $\phi_{electrode} \cong \zeta$ [5].
The potential boundary conditions for each electrode ($y = 0$), based on their measured zeta potentials (see section S1) were dynamically coupled with the pH in the model, by using a mixed Neumann/Dirichlet boundary condition,

$$\phi_{Pt} = \zeta_{Pt}(pH), \tag{3.15}$$

$$\phi_{Au} = \zeta_{Au}(pH). \tag{3.16}$$

The potential boundary condition at the upper part of the domain is

$$\frac{\partial\phi}{\partial y} = 0 \tag{3.17}$$

3.3.2 Ionic species transport

In this section, the boundary conditions that concern the flux of ionic species at the bielectrode's surface are described. For the proton flux, the electrochemical reaction is defined by the Frumkin-Butler-Volmer equation which has been used for studying transport phenomena near electrodes in other works [5, 2, 3, 1].

$$j = k_a \tilde{c}_{\mathrm{H_2O_2}} \exp\left(\frac{(1-\alpha)nF\Delta\tilde{\phi_{Stn}}}{RT}\right) - k_c \tilde{c_{\mathrm{H_2O_2}}} \tilde{c}^2_{\mathrm{H^+}} \exp\left(\frac{-\alpha nF\Delta\tilde{\phi_{Stn}}}{RT}\right) \tag{3.18}$$

where j is the proton flux expressed from the measured current density through Faraday's law of electrolysis, $j = i/nFAz$, A is the surface area of the electrodes and n is the number of electrons transferred during the reaction. The anodic and cathodic reaction rate constants are denoted as k_a and k_c, respectively. The proton current is simplified based on the assumption that the irreversible electrocatalytic reaction proceeds in the forward direction under the Tafel regime, which gives us an oxidation reaction flux j_{pt} occurring at the anode

$$j_{Pt} = k_a \tilde{c}_{\mathrm{H_2O_2}} \tag{3.19}$$

and a reduction reaction flux j_{Au} that occurs at the cathode

$$j_{Au} = k_c \tilde{c}_{H_2O_2} \tilde{c}_{H^+}^2 \tag{3.20}$$

By equating the diffusive, electromigration, and advective fluxes to the electrocatalytic reaction flux, we obtain the dimensionless flux boundary condition for the platinum and gold electrodes as

$$n.j_{H^+} = n \cdot (D_{H^+} \nabla c_{H^+} + z_{H^+} c_{H^+} \nabla \phi - \mathbf{u} c_{H^+}) = \begin{cases} j_{Pt} = D_{H^+} \mathrm{Da}_a \\ j_{Au} = D_{H^+} \mathrm{Da}_c c_{H^+}^2 \end{cases} \tag{3.21}$$

where $\mathrm{Da}_a = \frac{k_a L \tilde{c}_{H_2O_2}}{\tilde{D}_+ \tilde{c}_\infty}$ and $\mathrm{Da}_c = \frac{k_c L \tilde{c}_\infty \tilde{c}_{H_2O_2}}{\tilde{D}_+}$ are the dimensionless anodic and cathodic Damköhler numbers, respectively.
The fluxes of the anionic species, OH^- and Cl^-, are set to zero as they are inactive during the electrocatalytic reaction.

$$n \cdot j_{OH^-} = n \cdot (D_{OH^-} \nabla c_{OH^-} + z_{OH^-} c_{OH^-} \nabla \phi - \mathbf{u} c_{OH^-}) = 0 \tag{3.22}$$

$$n \cdot j_{Cl^-} = n \cdot (D_{Cl^-} \nabla c_{Cl^-} + z_{Cl^-} c_{Cl^-} \nabla \phi - \mathbf{u} c_{Cl^-}) = 0 \tag{3.23}$$

The concentration of the ionic species in the bulk region depends on the pH of the electrolyte through $(-\log_{10}(c_\infty))$. This is applied as a Dirichlet boundary condition at the upper part of the simulation domain as

$$c_i = c_\infty(pH) \tag{3.24}$$

3.3.3 Fluid flow

A no-slip condition was applied for the Stokes equation on all boundaries, which is given as

$$\mathbf{u} = 0. \tag{3.25}$$

The velocity developments within the domain are thus a direct result from the body force generated within the non-electrically neutral layer near the electrode surface.

3.4 Equilibrium reactions

Water auto-ionization occurs, where water molecule deprotonates to yield an hydroxide ion OH^-. The hydrogen, H^+ nucleus recombines with another water molecule to form hydronium, H_3O.

$$H_2O \longleftrightarrow H^+ + OH^- \tag{3.26}$$

The ionization constant of water is given as

$$K_w = [H^+][OH^-] = 1 \times 10^{-14} M^2 \tag{3.27}$$

The auto-ionization is then applied as a bulk reaction term within the simulation domain as

$$R_i = Da_b \left(\frac{K_w}{\tilde{c}_\infty^2} - c_{H^+} c_{OH^-} \right) \tag{3.28}$$

where Da_b is the bulk Damköhler number defined as $Da_b = \frac{k_{rb} L^2 c_\infty}{D_0}$, k_{rb} is the water recombination reaction rate constant.
In the course of the experimental studies, the bulk pH of the hydrogen peroxide solution was adjusted using HCl acid. The dissociation of HCl in water leads to the generation of H^+ and Cl^- ions and is associated with a large dissociation constant K_a (3.29). Cl^- is included in the model as an inert species whose concentration is determined by the bulk pH of the electrolyte solution, via the added HCl.

$$K_a = \frac{[H^+][Cl^-]}{[HCl]} = 1.3 \times 10^6 \tag{3.29}$$

The variation of the electrolyte's bulk pH would impact the ionic strength of the solution and the overall electrokinetic phenomena. Hence, we derive a complete expression that accounts for the bulk pH effects coupled with the bulk concentration for each ionic species in the model.
We consider three limiting conditions. First, the water dissociation equilibrium must be satisfied ($K_w = 1 \times 10^{-14}$ M^2) (3.27). Secondly, mass balance must be established between the undissociated acid and its conjugate base Cl^-. Hence, their sum is constant and equivalent to the nominal concentration c_{nom} (3.30). The nominal concentration c_{nom} refers to the initial acid concentration used for adjusting the pH during experiments.

$$c_{nom} = [HCl] + [Cl^-] \tag{3.30}$$

Since HCl completely dissociates in water, we neglect the first term in the right-hand side of equation (3.30) to obtain

$$\mathrm{c}_{nom} = [\mathrm{Cl}^-] \tag{3.31}$$

Electroneutrality condition must hold for the ionic solution where the sum of the corresponding ionic species charges equates to zero.

$$[\mathrm{H}^+] = [\mathrm{OH}^-] + [\mathrm{Cl}^-] \tag{3.32}$$

Combining equations (3.27) (3.31) and (3.32) gives an expression that connects the proton concentration with the concentration of the acid c_{nom}.

$$[\mathrm{H}^+] = [\mathrm{OH}^-] + [\mathrm{c}_{nom}] \tag{3.33}$$

The OH^- concentration can be eliminated by combining Eqns. (3.27) and (3.33) to give

$$[\mathrm{H}^+] = \mathrm{c}_{nom} + \frac{K_w}{[\mathrm{H}^+]} \tag{3.34}$$

Equation (3.34) implies that the proton concentration is equal to the nominal acid's bulk concentration. By defining $\mathrm{c}_{nom} = \tilde{c}_\infty$, whose ionic strength is highly dependent on the starting pH of the peroxide solution, equation (3.34) can be reformulated in a quadratic form $[\mathrm{H}^+]^2 - c_\infty[\mathrm{H}^+] - K_w = 0$, whose positive root is

$$\mathrm{H}^+ = \frac{\mathrm{c}_\infty + \sqrt{[\mathrm{c}_\infty]^2 + [4\mathrm{K}_w]}}{2}. \tag{3.35}$$

3.5 Simulation details

The governing equations are solved using the finite element method (FEM) through the commercial software, COMSOL multiphysics 5.5. The model was divided into sub domains to implement a user controlled non-uniform meshing sequence that consists primarily of triangular elements. The bielectrode region was structured and refined using mapped mesh control to accurately capture the electric double layer and to resolve the electrical and concentration gradients occurring at the electrode-electrolyte interface (see Fig 3.3).
To confirm mesh independence, the simulation was run on mesh element number ranging from $1.5 \cdot 10^4$ to $2.6 \cdot 10^5$. Mesh independence is observed as from N=10^5 elements, and further mesh refinement yielded velocities that varied

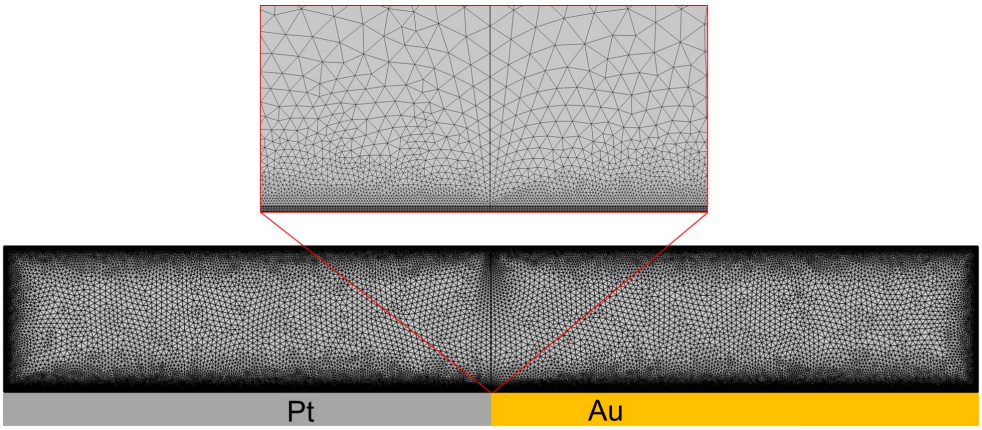

Figure 3.3: Mesh structure for the Pt-Au catalytic model. Inset: Zoom of the electrode region showing the mapped mesh structure.

less than 1%. To strike a compromise between solution accuracy and computation time, the element number was chosen at N=10^5. The model was computed using the PARDISO solver. Due to the non-linearity of the partial differential equations, the Poisson-Nernst-Planck equations were initially computed using a stationary solver and the resulting solution was used as initial values for the time-dependent solver that couples the Poisson-Nernst-Planck with Stokes' equations.

References

[1] Agar, J. [1967]. Double layer and electrode kinetics: by paul delahay, *Journal of Electroanalytical Chemistry and Interfacial Electrochemistry* **13**(4): 472.

[2] Bazant, M. Z., Chu, K. T. and Bayly, B. J. [2005]. Current-voltage relations for electrochemical thin films, *SIAM Journal on Applied Mathematics* **65**(5): 1463–1484.

[3] Biesheuvel, P., van Soestbergen, M. and Bazant, M. [2009]. Imposed currents in galvanic cells, *Electrochimica Acta* **54**(21): 4857 – 4871.

[4] Esplandiu, M. J., Afshar Farniya, A. and Reguera, D. [2016]. Key parameters controlling the performance of catalytic motors, *Journal of Chemical Physics* **144**(12).

[5] Moran, J. L. and Posner, J. D. [2011]. Electrokinetic locomotion due to reaction-induced charge auto-electrophoresis, *Journal of Fluid Mechanics* **680**: 31–66.

Chapter 4

Electrocatalytic Reaction Driven flow (ERDF)

[1]

Abstract

Immobilized electrocatalytic surfaces are capable of generating reaction driven fluid flow by electrochemical energy conversion. A well known system concerns the Au-Pt bimetallic motor driven by hydrogen peroxide conversion. In this work, we focus on experimental and numerical analyses that provide fundamental insight on the key elements that control the resulting transport characteristics in this system, including the generated electric field, reaction kinetics and diffusio-electroosmotic phenomena. The current between the electrodes and the induced potential that governs the reactive fluxes are measured electrochemically, while the fluid flow is analyzed using particle tracking velocimetry. Numerical simulations based on the Poisson-Nernst-Planck and Navier-Stokes equations reveal the interplay of the individual electrode surface reactivity, represented by the dimensionless Damköhler numbers, with the electrokinetic phenomena.

[1]Published as: **Abimbola A. Ashaju**, Jeffery A. Wood, and Rob G. H. Lammertink, *Electrocatalytic reaction-driven flow*, Phys. Rev. Fluids. **6**, 044004 (2021)

4.1 Introduction

Nature has engineered nanoscale biological motors in form of microorganisms and proteins, that are capable of converting chemical energy for complex molecular processes and biological functions [15, 19]. Inspired by nature, researchers became actively involved in developmental activities where structures are synthesized, manipulated and controlled at the molecular, atomic, and macromolecular scale for diverse applications. A good example is the locomotion of a catalytic nanorod within a fluid medium, which is powered by the conversion of chemical energy (fuel) that is harvested from the surrounding aqueous fluid [24, 23, 30]. The functionality of the nanorod has been adapted towards applications such as DNA detection, [33] cargo delivery, [14, 29, 7] and rotary electromechanical devices [14].

The autonomous motion of catalytic nanorods has been observed and reported in literature [24, 31, 16]. A single nanorod comprises of a bimetallic duo that catalyzes the decomposition of a fuel, thereby creating the necessary gradients (concentration, potential) for its motion. During the electrochemical reaction at the two metals (e.g. platinum and gold) with hydrogen peroxide solution, oxidation occurs at the anode (platinum) yielding protons, electrons and oxygen, while reduction takes place at the gold cathode where protons and electrons are consumed with water produced as a byproduct (figure 4.1). The resulting ion and electron flow generates an electric field that is coupled with the local non-neutral fluid, to create a body force that drives interfacial fluid motion.

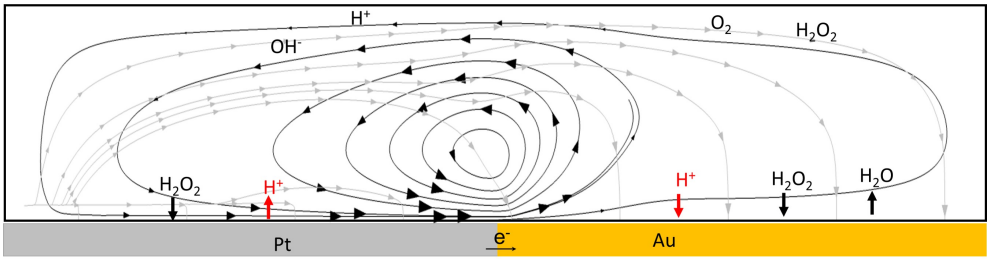

Figure 4.1: A schematic that describes a Au-Pt reactive pair that catalytically decomposes hydrogen peroxide yielding reactive ionic species, which generates an electric field (gray streamlines) that drives fluid flow (black streamlines).

Recent progress has expanded the application of nanomotors into microfluidics in form of an immobilized system [34]. An immobilized nano/micromotor can generate an interfacial convective fluid flow driven by electrochemical gradients that arise from electrocatalytic reactions. Immobilized micromotors (also known as micropumps) have been integrated into small confinements for microscale fluid flow applications, which are capable of improving mass transport in areas impacted by boundary layer resistance [17]. Despite these advancement, some issues still limit the practical usage of an immobilized micromotor, especially its low energy conversion [34]. Understanding the fundamental parameters that drive the electrocatalytic reaction is necessary to fully exploit the fluid flow generated by an immobilized micromotor.

The literature that concerns catalytic micropumps comprises both experimental and numerical studies. In the experimental part we consider the electrochemical reaction that generates the electric field, which drives fluid flow. The metallic electrodes and electrolyte constitute altogether an electrochemical cell, whose characterization yields insight on the reaction mechanism that occurs at the electrode-electrolyte interface. The electrochemical reaction that actuates the catalytic micropump has been validated through the direct measurement of the catalytic current between the electrodes during the decomposition of H_2O_2 [23]. Tafel plots for anodic and cathodic reactions from Au and Pt electrodes were obtained from voltammetry measurements [31], from which the mixed potential that balances reactive fluxes was inferred. Furthermore, the Tafel plots identify the role of each metals via the anodic and cathodic branch, respectively, and the corresponding conversion rate via the current.

The proton flux that creates the electrical body force, which drives fluid flow, has been studied experimentally. Farniya et al. [13] imaged the concentration gradient that is generated during the electrochemical reaction using confocal fluorescence microscopy. They visualized the spatial variation of protons across the bielectrode, and quantified the amount that was generated and consumed under steady state conditions. Moreover, they estimated the electrostatic potential distribution and electrode zeta potentials via the tracking of positively and negatively charged particles driven by a disk shaped Pt-Au catalytic micropump. Simulations were fit to experimental measurements using the reaction rate constants, ion impurities and surface ζ potential as fitting parameters. They imposed a fixed zeta potential value for the electrode in their simulations likewise that of the tracer particles for the fluid flow estimation and fluid pumping velocities up to 6 μm/s were deduced. A slight variation in electrolyte pH can have huge consequences for the electrostatic potential and

the fluid velocity as we will show.

Moran and Posner [20, 21] developed a scaling analysis and performed numerical simulations that describe the movement of bimetallic nanorods fueled by hydrogen peroxide decomposition. They described how the nanorods motion is driven by the coupling of charge density and electric fields, by solving the coupled Poisson-Nernst-Planck with Stokes equations and considered two specific forms of boundary conditions. First, they directly applied fixed fluxes on the electrodes and considered the rod to be uncharged by imposing a zero surface potential. Under this condition, the velocity field, albeit very small, near the rod showed a quadrupolar shape similar to induced charge electro-osmosis. Secondly, they relaxed the zero surface charge assumption and took into account the reaction kinetics, by introducing reactive flux expressions simplified from Butler-Volmer equations. This approach couples the reaction rate to the nanorods surface potential as well as the evolution of reactants concentrations on the nanorods surface and led to realistic and more significant velocity values. Both the sign and magnitude of the rod's surface potential were found to play a determining role in its motion according to these simulations.

Esplandiu et al. [12] studied the fundamental parameters that govern the operation of a bimetallic micropump and they attributed the fluid flow to be driven by self-induced electric field generated by the proton gradient across the electrodes. Their model ignored water auto-ionization reaction. Davidson et al. [9] numerically analyzed reactivity patterns defined by the dimensionless Damköhler number that generates and depletes protons, which were related to the catalytic output of the bimetallic micropump. They also developed a simplified analytical model to predict the induced potential which balances electrode reactive fluxes and velocity flow magnitude.

This work aims at performing a detailed experimental and numerical study of an immobilized electrocatalytic system under different surface reactivity regimes defined by the dimensionless Damköhler numbers. We characterize the electrochemical behavior of the electrocatalytic system through voltammetric Tafel analysis and direct potential measurement. Using particle tracking velocimetry we visualize the electro-hydrodynamic response of the system and quantify the convective fluid flow. The induced fluid flow scales directly with the electrode zeta potential and the electric field according to Helmholtz Smoluchowski equation. The zeta potential is highly sensitive to pH which impacts the overall electrokinetic output. For this reason we measure the bi-electrode zeta potential under pH conditions ranging from 2 to 10. Based on our experimental observations, a 2D numerical model that couples Pois-

son–Nernst–Planck and Navier–Stokes equations is solved for the potential, concentration and velocity field under several reactive regimes while using experimental electrochemical data as parameter input without any fitting parameter. Our numerical model advances existing numerical work by the inclusion of electrode zeta potential that was measured experimentally under varying pH conditions.

4.2 Experimental setup

4.2.1 Chip fabrication

The Au and Pt electrode patterns were fabricated on borosilicate glass wafers via photolithography, metal sputtering, and lift-off. For each lift-off, positive resist was spun on the glass wafer, followed by UV-exposure and development as described in [32]. Platinum and gold electrodes on Tantalum (5nm) an adhesive layer, were deposited by DC sputtering (MESA+ nanolab clearoom in-house equipment,"TCOathy"). Lift off was performed by sonication in acetone. To investigate the diffusio-electro-osmotic phenomena, two design variants were fabricated; interdigitated electrodes (IDE) and Pt-Au bimetallic electrodes (figure 4.2). The IDE consists of electrode fingers of alternating platinum and gold connected to separate terminals. These electrode fingers have an interspacing of 40 μm and an electrode width of 50 μm. Each terminal is wire bonded to a printed circuit board. The bimetallic electrode consists of both Pt and Au in direct contact that forms a galvanic pair with a total length of 10 mm (figure 4.2b). Prior to any experimental procedure, the electrodes were cleaned by rinsing with isopropyl alcohol and DI water. The electrodes were then subjected to oxygen plasma (plasma power = 100 W, oxygen gas pressure = 0.5 bar, 5 minutes) to remove organic contaminants and photoresist residues [13].

4.2.2 Electrochemical characterization

The electrochemical experiments were conducted in hydrogen peroxide solution (Sigma Aldrich) using an Autolab PGSTAT204 potentiostat, running NOVA 2.0 software. Two forms of experiments were performed, namely induced potential measurement (IPM) and Tafel analysis. IPM was performed by measuring the potential difference between the short-circuited electrodes and the electrolyte during the electrochemical reaction [22]. This is shown schematically in figure 4.3, where the Pt/Au-electrodes are connected to a

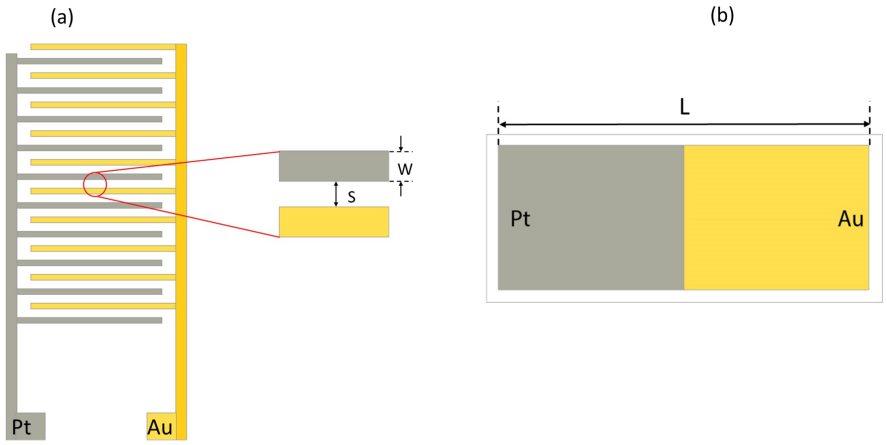

Figure 4.2: Schematics showing the fabricated (a) Interdigitated electrodes used for electrochemical measurement, with interspacing S = 40 μm and electrode width W = 50 μm. (b) Pt-Au bimetallic electrode for flow characterization experiments, having a total length L = 10 mm.

single working electrode terminal of the potentiostat and the induced potential was measured against a micro Ag/AgCl reference electrode (eDAQ model ET073).
Voltammetric experiments were performed for the Tafel analysis using a three-electrode system, where either of the two electrodes acts as the working electrode while the other is set as the auxiliary electrode (figure 4.3). The electrodes were polarized independently with potential sweeps within the oxidation and reduction range at a scan rate of 1 mV/s and their amperometric response is recorded [31].

4.2.3 Optical microscopy

Hydrogen peroxide solution (Sigma Aldrich) was diluted to the desired concentration using MilliQ water (Resistivity $\rho > 18$ MΩ.cm). We measured the conductivity of the peroxide solution that was prepared with D.I water, to be in the range of 10 to 30 μS/cm. Tracer particles (carboxylated-modified FluoSpheres^{TM}, and amidine latex beads, Fischer scientific), 1 μm in diameter, were seeded into the electrolyte and introduced into an imaging chamber (height H = 1500 μm) containing the bielectrode. The tracer particles were observed at 20x magnification using an inverted optical microscope (Carl Zeiss

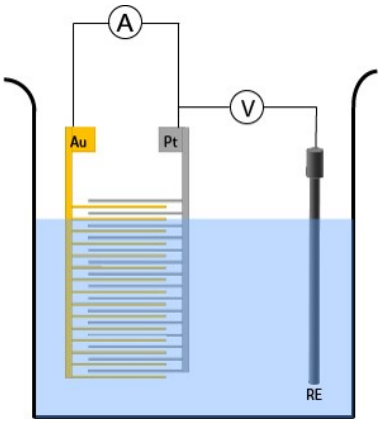

Figure 4.3: Schematic representation of the electrochemical setup with the interdigitated electrodes.

Axio Observer Z1) (figure 4.4), with images obtained at 10 fps. The particles trajectories were resolved using the general defocusing particle tracking (GDPT) technique [4].

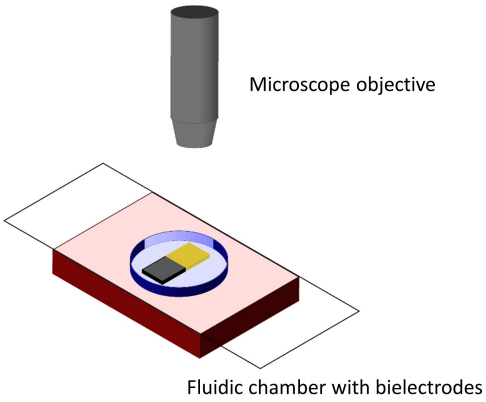

Figure 4.4: A schematic diagram of the fluid flow experiment. The bimetallic electrode is sealed within a fluidic chamber by a cover glass slide.

4.2.4 Tracer particles zeta potential measurement

The zeta potential of tracer particles used for fluid flow visualization was measured using a Zetasizer Nano ZS (Malvern instrument). Particle dispersions were prepared in MilliQ water and sonicated for 5 minutes. An AC electric field is applied to the colloidal dispersion and the particles electrophoretic velocity is determined through laser Doppler velocimetry (LDV). During LDV, the moving particles are excited by a laser beam and diffuse light at frequencies that differ from the incident light. The frequency shift is proportional to the particles velocity from which the electrophoretic mobility is determined ($\mathbf{u}_p = \mu_e E$). The zeta potential was calculated from the electrophoretic mobility by Henry's approximation, $\mu_e = \frac{2\varepsilon\zeta f(ka)}{3\eta}$ based on Smoluchowski approximation, where μ_e is the electrophoretic mobility, $f(ka)$ is the Henry's function, ε is the permittivity, ζ is the zeta potential and η is the viscosity of the fluid medium [27, 8].

4.3 Theory and Numerical Simulations

Numerical simulations were performed using COMSOL Multiphysics, a finite-element based solver. We simulated a two-dimensional model with an aspect ratio of $H/L = 0.15$, that is representative of our experimental setup involving the bielectrode (H = 1500 μm, L = 10000 μm). The catalytic decomposition of hydrogen peroxide on a platinum-gold catalytic system is considered through oxidation and reduction pathways, given as

$$\mathrm{H_2O_2} \longrightarrow 2\,\mathrm{H^+} + \mathrm{O_2} + 2\,\mathrm{e^-} \tag{4.1}$$

$$\mathrm{H_2O_2} + 2\,\mathrm{H^+} + 2\,\mathrm{e^-} \longrightarrow \mathrm{H_2O} \tag{4.2}$$

where oxidation occurs on platinum (the anode) and reduction takes place on gold (the cathode) [25].
We emphasize at this point that we focus on the simplest form of the electrochemical reaction that yields the generation and consumption of protons [20]. In our simulations we consider $\mathrm{H^+}$, $\mathrm{OH^-}$, as well as $\mathrm{Cl^-}$ that results from the dissociation of HCl acid during the adjustment of the electrolyte's bulk pH.

4.3.1 Poisson-Nernst Planck and Stokes equations

The electrokinetic phenomena exhibited by the Pt/Au system is solved and described by the coupled Poisson-Nernst-Planck and Stokes equations. This

approach has been used in other works to simulate the locomotion of nanorods [21] and catalytically induced flows [9, 12]. The dimensionless forms of the governing equations are presented in equations (4.3)-(4.6), more details on its derivation and transformation can be found in Druzgalski et al. [10].
The dimensionless Poisson equation (4.3) solves for the induced potential, whose gradient yields the electric field together with the local charge density. The Poisson equation is coupled with the ionic species transport to resolve the electrical double layer formed during the electrochemical reaction at the electrode-electrolyte interface. The dimensionless Debye length $\epsilon = \frac{L_D}{L}$ whose value is selected to ensure numerical stability, where L is the bielectrode total length, $L_D = \sqrt{\frac{\varepsilon V_T}{2F\tilde{c}_\infty}}$ is the Debye length, usually hundreds of nanometers for low salt concentration, $\tilde{c}_\infty$ is the bulk proton concentration.

$$-2\epsilon^2\nabla^2\phi = \Sigma_i z_i c_i \tag{4.3}$$

$\phi = \frac{\tilde{\phi}}{V_T}$ is the dimensionless electrostatic potential obtained by normalizing the electrostatic potential by the thermal voltage $V_T = \frac{RT}{F} \approx 25$ mV, T is the temperature, F is the Faraday constant ($F = 96485$ C mol^{-1}), and R is the universal gas constant (8.314 J/K.mol). The tilde symbol, ($\tilde{}$) implies a dimensional quantity.
The dimensionless Nernst-Planck equation describes the ionic species transport by solving the advection-diffusion and electro-migration contributions (4.4), where $\mathbf{u}$ is the fluid velocity and $c_i = \frac{\tilde{c}_i}{\tilde{c}_w}$ is the concentration of species i normalized by the bulk concentrations of H^+ and OH^- in pure water ($\tilde{c}_w = 1 \times 10^{-7}$ M), having a diffusion constant $D_i = \frac{\tilde{D}_i}{\tilde{D}_0}$ with valence z_i. $\tilde{D}_0$ is the diffusivity of hydroxide ($\tilde{D}_0 = 5.273 \times 10^{-9}$ m^2/s) ions chosen as an arbitrary reference value. $R_i = \mathrm{Da}_b \left(\frac{K_w}{\tilde{c}_\infty^2} - c_{H^+} c_{OH^-} \right)$ is a bulk reaction term that enforces water autoionization for H^+ and OH^-. K_w is the water ionization constant expressed as $K_w = [H^+][OH^-] = 1 \times 10^{-14}$ M^2. Da_b is the bulk Damköhler number defined as $\mathrm{Da}_b = \frac{k_{rb} L^2 \tilde{c}_\infty}{\tilde{D}_0}$, where k_{rb} is the water recombination reaction rate constant, c_{H^+} and c_{OH^-} are proton and hydroxide species concentrations.

$$\frac{\partial c_i}{\partial_t} + \nabla \cdot (\mathbf{u} c_i) = D_i \nabla \cdot (\nabla c_i + z_i c_i \nabla \phi) + R_i \tag{4.4}$$

The fluid flow is assumed laminar and incompressible, giving rise to the Stokes and continuity equations (4.5 and 4.6). The inertial term on the left-hand side

of equation 4.5 is neglected under low Reynolds regime ($\frac{1}{\mathrm{Sc}}\frac{\partial \mathbf{u}}{\partial t} = 0$), where Sc is the Schmidt number defined as $\mathrm{Sc} = \frac{\eta}{\rho \tilde{D}_0}$ and of $O(10^3)$. The electro-hydrodynamic coupling constant is defined as, $\kappa = \frac{\varepsilon V_T^2}{\eta \tilde{D}_0} = 0.093$ and is typically fixed by the aqueous electrolyte properties.

$$0 = -\nabla p + \nabla^2 \mathbf{u} - \frac{\kappa}{2\epsilon^2}\rho_e \nabla \phi \tag{4.5}$$

$$\nabla \cdot \mathbf{u} = 0 \tag{4.6}$$

4.3.2 Acid-base equilibria and initial concentrations

In our experimental study, we adjusted the starting pH of the hydrogen peroxide solution by the addition of HCl, yielding H^+ and Cl^-. Cl^- is included as inert species in the model whose initial concentration is fixed by the value of the bulk electrolyte pH. We derive an expression that relates the initial proton concentration, $\tilde{c}_{H^+}$ depending on the bulk pH and other limiting conditions involving water equilibrium and electroneutrality (4.7) (see chapter 3, section 3.4).

$$\tilde{c}_{H^+} = \frac{\tilde{c}_\infty + \sqrt{[\tilde{c}_\infty]^2 + [4K_w]}}{2} \tag{4.7}$$

4.3.3 Surface reactivity pattern

The surface reactivity is represented by the dimensionless Damköhler number Da that relates the electrocatalytic reaction timescales to diffusive transport timescales [20]. It can be defined for individual electrodes in the catalytic system as the anodic Da_a and cathodic Da_c Damköhler number shown in equation (4.8) and (4.9). Variation of these respective Da numbers will create reaction regimes that highlight the role of each electrode on proton generation and depletion.

$$\mathrm{Da}_a = \frac{k_a L \tilde{c}_{H_2O_2}}{\tilde{D}_+ \tilde{c}_\infty} \tag{4.8}$$

$$\mathrm{Da}_c = \frac{k_c L \tilde{c}_\infty \tilde{c}_{H_2O_2}}{\tilde{D}_+} \tag{4.9}$$

The anodic and cathodic rate constants are denoted by k_a and k_c respectively, $\tilde{c}_{H_2O_2}$ is the concentration of hydrogen peroxide, $\tilde{D}_+$ is the proton diffusivity constant ($\tilde{D}_+ = 9.3 \times 10^{-9}$ m^2/s), and $\tilde{c}_\infty$ is the bulk proton concentration that is fixed by the pH of the solution.

4.3.4 Boundary conditions

We apply a no-slip condition, $\mathbf{u} = 0$, on all boundaries. The electrical double layer induced during the electrochemical reaction at the electrode-electrolyte interface is divided into two regions, namely the Stern and diffuse layer [18]. Our model explicitly resolves the diffuse layer part of the electric double layer, while the Stern layer contribution is resolved by scaling the potential drop across the Stern layer ($\Delta\phi_{Stn}$) with the zeta potential ζ (4.11), and the Debye length [20, 12].

$$\Delta\phi_{Stn} = \zeta - \phi_{electrode} \tag{4.10}$$

$$\Delta\phi_{Stn} \approx \frac{L_{Stn}}{L_D}\zeta \tag{4.11}$$

At low salt concentrations $\frac{L_{Stn}}{L_D} \ll 1$, and $\Delta\phi_{Stn}$ is extremely small, hence $\phi_{electrode} \cong \zeta$, where L_{Stn} and L_D are the Stern layer and Debye thickness. The potential boundary condition at the surface of the electrodes (y=0) is defined by their respective zeta potential as $\phi_{Pt} = \zeta_{Pt}$, and $\phi_{Au} = \zeta_{Au}$. The zeta potential associated with each electrode has been experimentally deduced from the streaming current (see Appendix S1) and was found to be highly dependent on pH (Fig S1). For this reason, the potential boundary condition is coupled to the zeta potential of the appropriate electrode, which corresponds to a certain pH in the model using a mixed Neumann/Dirichlet boundary condition. The boundary condition at the upper boundary is defined as $\frac{\partial\phi}{\partial y} = 0$.
The initial concentration for individual ionic specie depends strongly on the bulk electrolyte pH ($-\log_{10}(\tilde{c}_\infty)$), and is applied as a Dirichlet condition at the uppermost boundary of the model. Anions are inactive during the electrocatalytic reaction, hence their flux is set to zero (4.12 and 4.13).

$$n \cdot j_{\mathrm{OH^-}} = n \cdot (D_{\mathrm{OH^-}} \nabla c_{\mathrm{OH^-}} + z_{\mathrm{OH^-}} c_{\mathrm{OH^-}} \nabla\phi - \mathbf{u} c_{\mathrm{OH^-}}) = 0 \tag{4.12}$$

$$n \cdot j_{\mathrm{Cl^-}} = n \cdot (D_{\mathrm{Cl^-}} \nabla c_{\mathrm{Cl^-}} + z_{\mathrm{Cl^-}} c_{\mathrm{Cl^-}} \nabla\phi - \mathbf{u} c_{\mathrm{Cl^-}}) = 0 \tag{4.13}$$

The electrochemical reaction flux that occurs at the electrode/electrolyte interface has been reformulated from the Frumkin-Butler-Volmer equation [20]. We apply the proton flux boundary condition on platinum and gold, which has been derived by matching the combined diffusive and electromigration fluxes with the electrocatalytic reaction flux [9], where $j_{\mathrm{H^+}}$ refers to proton flux across the electrodes (4.14), j_{Pt} and j_{Au} are defined as platinum and gold

surface proton flux respectively.

$$n.j_{\mathrm{H^+}} = n \cdot (D_{\mathrm{H^+}} \nabla c_{\mathrm{H^+}} + z_{\mathrm{H^+}} c_{\mathrm{H^+}} \nabla \phi - \mathbf{u} c_{\mathrm{H^+}}) = \begin{cases} j_{Pt} = D_{\mathrm{H^+}} \mathrm{Da}_a \\ j_{Au} = D_{\mathrm{H^+}} \mathrm{Da}_c c_{\mathrm{H^+}}^2 \end{cases} \tag{4.14}$$

4.3.5 Mesh independence

The commercial finite element method (FEM) software COMSOL Multiphysics 5.5 was used in solving the dimensionless governing equations. To confirm mesh independence, the simulation was run on mesh element number ranging from $1.5 \cdot 10^4$ to $2.6 \cdot 10^5$. Mesh independence is observed as from N=10^5 elements, and further mesh refinement yielded velocities that varied less than 1%. To strike a compromise between solution accuracy and computation time, the element number was chosen at N=10^5, with the mesh refined around the electrodes region to accurately capture the electric double layer and to resolve the electrical and concentration gradients occurring at the electrode-electrolyte interface.

4.4 Results and discussion

4.4.1 Electrochemical mechanism

When the interdigitated electrodes are connected and immersed in hydrogen peroxide solution, anodic and cathodic reactions occur [11]. A common potential is generated for the electrodes during the electrochemical reaction that balances reactive fluxes on both electrodes. By connecting and disconnecting interdigitated electrodes repeatedly at certain time intervals, the induced potential is always regenerated during the connected mode, while the open circuit potential for individual electrodes is observed during the off mode (figure 4.5a). Moreover, the induced potential shows sensitivity to the mode of operation and confirms the electrochemical decomposition of hydrogen peroxide as the basis for electrocatalytic actuation.
Figure 4.5b shows the Tafel plots for Pt and Au electrodes in 0.325 M H_2O_2, representing the electrochemical current versus the applied potential. In these measurements, the potential of each electrode is varied and the current response is obtained. The Tafel curve for each individual electrode consists of anodic and cathodic branches that corresponds to oxidation and reduction pathways, respectively. The sharp dip in each current response indicates the mixed potential where the net current is zero. At this potential, the transition

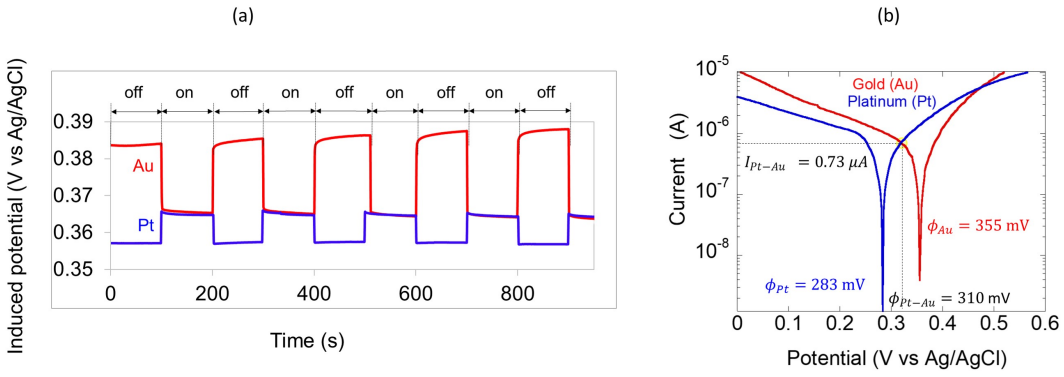

Figure 4.5: Representative plots for: (a) Induced potential vs time for the interdigitated electrodes in 0.325 M H_2O_2 during the on and off mode. (b) Tafel plots for Au-Pt interdigitated electrodes in 0.325 M H_2O_2.

from oxidation to reduction and vice versa occurs [3]. The mixed potential describes the role of each electrode if they are electrically connected and thus at the same potential [31]. Gold acts as the cathode, and platinum as the anode. The point at which both voltammetric profiles intersect yields the catalytic current (0.73 μA) and bimetallic potential (310 mV) arising from a connected platinum-gold electrode system.
The bimetallic potential that was obtained from the Tafel plots is comparable to the induced potential measurement. Accordingly, both techniques are appropriate for quantifying the induced potential that enforces current conservation across the bielectrode.

4.4.2 Fluid flow visualization and quantification

When a suspension of tracer particles and hydrogen peroxide was fed into the chamber, a combined mechanism of electrostatic and hydrodynamic interactions occurs near the electrode region (figure 4.6). The negatively charged particles migrate to both the Pt and Au electrodes and eventually become trapped owing to a strong electrophoretic force close to the surface of the bielectrode. They form patterns and aggregates that highlight the junction between Pt and Au electrodes (figure 4.6a). Near the surface, the particles are transported from Pt to Au while the opposite movement occurs at the upper

region of the channel, (figure 4.6b, supplementary material video 2 [1]).

The pattern of fluid movement is verified by imaging from the side view near the connected electrodes region. The particle transport tracks that are obtained by superimposing image frames (imageJ particle tracker) [26], confirms fluid flow from platinum to gold (figure 4.6c).

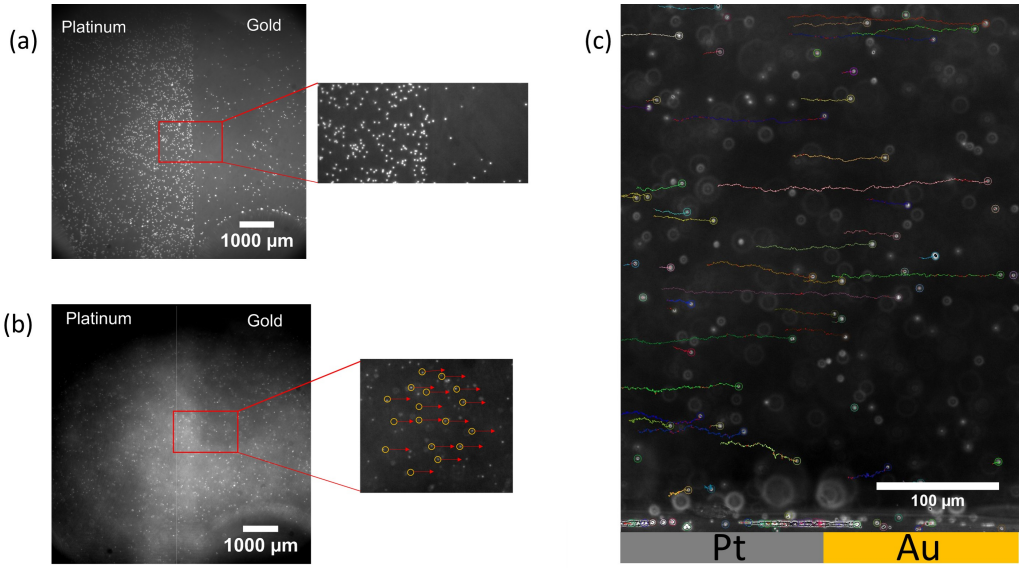

Figure 4.6: Fluid flow visualization by particle tracking. (a) Formation of colloidal patterns on the bimetallic electrode due to an electrostatic force. (b) Colloidal particles are driven by catalytically induced fluid flow near the electrode's surface region. (c) Particle tracks for fluid flow observed from the electrodes side view.

The observed particle velocities $\mathbf{u}_p$ consists of both the electrophoretic $\mathbf{u}_{ep}$ and the fluid flow $\mathbf{u}_f$ components (4.15). Decoupling these yields the actual magnitude of the catalytically induced fluid flow. This can be realized by using the two-particle correlation [13, 28], where two particles similar in size and having different electrophoretic mobilities can be used in determining the fluid flow under the same experimental conditions. The particle velocity for the different tracer particles (here positive and negative) are defined in 4.16

and 4.17 to yield the fluid flow velocity (Eq. 4.18).

$$\mathbf{u}_p = \mathbf{u}_{ep} + \mathbf{u}_f \tag{4.15}$$

$$\mathbf{u}_{p_+} = \frac{\varepsilon}{\eta}\zeta_{p_+}E + \mathbf{u}_f \tag{4.16}$$

$$\mathbf{u}_{p_-} = \frac{\varepsilon}{\eta}\zeta_{p_-}E + \mathbf{u}_f \tag{4.17}$$

$$\mathbf{u}_f = \frac{\zeta_{p_+}\mathbf{u}_{p_-} - \zeta_{p_-}\mathbf{u}_{p_+}}{\zeta_{p_+} - \zeta_{p_-}}, \tag{4.18}$$

where ζ_{p_+} and ζ_{p_-} correspond to the zeta potentials for the positive and negative tracer particles respectively (see Appendix S2), η is the fluid viscosity, and ε is the permittivity of the fluid (7.10×10^{-10} F/m).

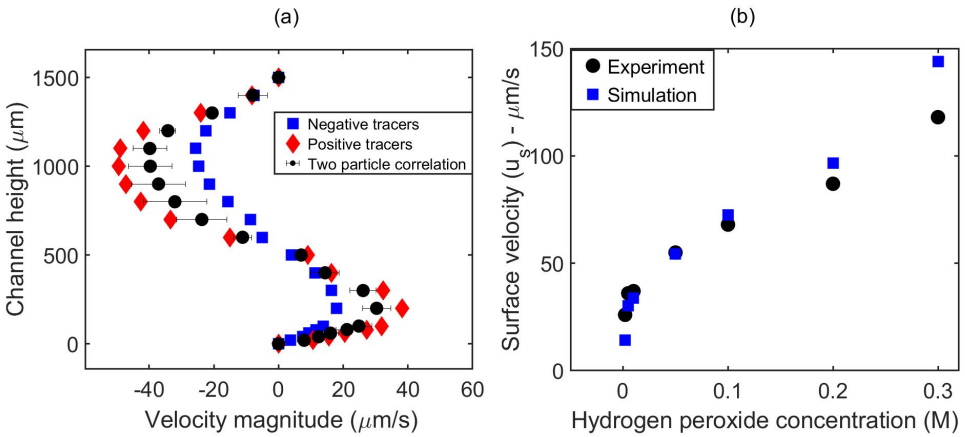

Figure 4.7: (a) Two particle correlation velocimetry used in determining the flow velocity, for 0.3 M H_2O_2, pH 6. The particle velocities are plotted as a function of the channel height. Flow near the surface of the bielectrode is driven from Pt to Au while the opposite movement is obtained at the upper part of the channel due to fluid continuity. Error bars represents standard deviations from triplicate measurements. (b) Comparison of experimentally estimated surface fluid velocity u_s with simulation result as a function of H_2O_2 concentration.

Figure 4.7a shows the particle velocity profiles along the channel height from the bielectrode junction. The velocity of the positive tracers exceeds that of the

negative tracers due to the interaction between the induced electric field and the zeta potential of the particles, which creates an electrophoretic force that enhances the movement of the positive particles. In the case of the negative tracers, the electrophoretic force retards the movement of the particles with respect to the fluid flow. The positive and negative tracers velocities were averaged at every height and solved with the two-particle correlation (4.18) to extract the fluid flow that presents a similar profile. The fluid flow at the bielectrode region is driven from the anode to the cathode in the positive sense, while the negative flow recorded at higher heights occurs in the opposite direction due to flow continuity within the confined channel.

We compare our estimated experimental fluid velocity (inferred from the particle tracer velocities) with our numerical simulation for the case of 0.3 M H_2O_2, pH 6. Figure S4 shows a strong quantitative similarity between both flow profiles, except for the near electrode region. The deviation results from a strong electrophoretic force that impacts particle motion around the electrode surface region.

We determined the electrophoretic force for both negative and positive tracers and compared these with the fluid drag force at each location in figure S3 (see appendix S3). At the lower part of the channel ($y \leq 400$ μm), the electrophoretic force becomes dominant. Near the surface of the bielectrode ($y \leq 25$ μm) the electrophoretic force becomes amplified by the strong electric field and affects the movement of the charged particles in conjunction with the fluid drag force. Very near the electrodes, the electrophoretic force can be an order of magnitude higher than the drag force, which results into fluid flow retardation and high offset between simulations and experimentally inferred velocities. To circumvent this problem, a simple analytical expression was fitted with the upper parabolic part of the experimental fluid flow velocity ($y \geqslant 600\mu m$) where the influence of the electrophoretic force is less severe (see appendix S3). The fit obtains a surface velocity u_s that is comparable with the maximum velocity obtained from the simulation (Fig S4). We investigated the dependence of the surface velocity on the concentration of hydrogen peroxide that fuels the reaction. Both experimental and simulation results indicate that the induced velocity increases with H_2O_2 concentration (figure 4.7b).

4.4.3 Numerical Simulations

In order to understand further our experimental observations, simulations were conducted using our electrochemically measured current 0.6 μA (for 2 mM

H_2O_2 and pH = 6) as an input parameter. The current was converted to molar flux (mol/m^2.s) and applied directly as an electrode boundary condition in the model. The effective rate constants for the oxidation and reduction reactions are extracted from the simulation results by applying the Frumkin-corrected Butler-Volmer equation (4.19) which has been adopted in other works for investigating transport phenomena near electrodes [6, 2, 20, 5].

$$j = k_a \tilde{c}_{\mathrm{H_2O_2}} \exp\left(\frac{(1-\alpha)nF\Delta\tilde{\phi_{Stn}}}{RT}\right) - k_c \tilde{c_{\mathrm{H_2O_2}}} \tilde{c}^2_{\mathrm{H^+}} \exp\left(\frac{-\alpha nF\Delta\tilde{\phi_{Stn}}}{RT}\right) \quad (4.19)$$

Here, $j_{\mathrm{H^+}}$ is the proton flux expressed from the measured current density through Faraday's law, n is the number of electrons transferred during the reaction, k_a is the anodic rate constant ($k_a = 1.63 \times 10^{-7}$ m/s) and k_c is the cathodic rate constant ($k_c = 5.16 \times 10^{-4}$ $\mathrm{m^7\ s^{-1}\ mol^{-2}}$). These rate constants are used in determining the respective Damköhler numbers, which are defined in (4.8) and (4.9). The Damköhler numbers are calculated to be $\mathrm{Da}_a = 350$ and $\mathrm{Da}_c = 1$ respectively. The zeta potential for gold and platinum electrodes that corresponds to the bulk electrolyte pH are directly inferred from Fig S1 to be approximately (-32 mV and -33 mV) respectively.

Figure 4.8a shows the pH profile that highlights the proton gradient that is spatially established across the electrodes during the steady-state reaction. Proton generation at the anode (Pt) is indicated by a low pH while protons are depleted at the cathode (Au). Figure 4.8b shows the induced electric potential, overlaid with electric field lines that results from the proton gradient. The electric field originates from the anode and points towards the cathode. The product of the electric field with local charge density creates a body force that drives fluid flow, whose magnitude appears to be maximum around the junction of the connected electrodes (figure 4.8c). The fluid flow streamlines confirm the direction of the fluid movement, from the anode to the cathode, and recirculated within a closed system to fulfil continuity. These electrokinetic observations are coupled, autonomous and self-driven by the electrocatalytic reactions.

Further simulations were performed by keeping either of the experimentally determined Damköhler numbers constant while solving the other over a specified range. The variation of these numbers, which may be difficult to realize experimentally, gives more insight to our experimental observations. The resulting axial velocities $u(y)$ are plotted along the vertical direction from the electrodes (figure 4.9).

In the case where Da_c is varied (Fig 4.9a), the induced velocity is inversely proportional to an increase in Da_c. At $Da_c > 1000$, the anodic oxidation

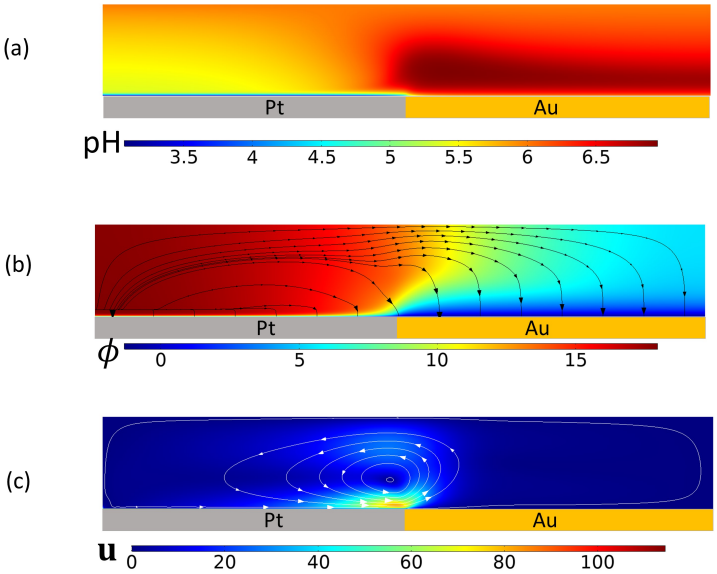

Figure 4.8: Simulation field results for $Da_a = 350$, $Da_c = 1$, 2mM H_2O_2, pH 6 (a) Proton spatial distribution indicated by pH value. (b) Dimensionless induced potential overlaid by electric field streamlines, generated by proton flux (arrows). (c) Dimensionless velocity magnitude with streamlines.

reaction limits the overall catalytic process because it is incapable of dealing with the cathodic demands. Consequently, the proton gradient that generates the electrical body force becomes weak, and the induced velocity reduces in magnitude.

The variation of Da_a presents interesting observations on the induced velocity (figure 4.9b). In the case of $Da_a \geqslant 100$, the velocity flow profiles are similar to the Da_c controlled reactions where the flow is driven from the anode to the cathode. At $Da_a < 100$ the flow becomes reversed and redirected from the cathode to anode (see inset of figure 4.9b and fig. S5). A similar trend was reported for a Pt-Au hydrogen peroxide system in pure water that is devoid of additional ionic species, which confirms the flow reversal to be reaction driven at lower anodic Damköhler numbers [9].

The possible flow reversal was explored experimentally by tuning some parameters in Eq.4.8 to generate a lower Da_a reactive regime. The parameters of interest are the concentration of H_2O_2 and the pH that impacts the bulk ion concentration $\tilde{c}_\infty$. Other parameters such as the diffusion coefficient and

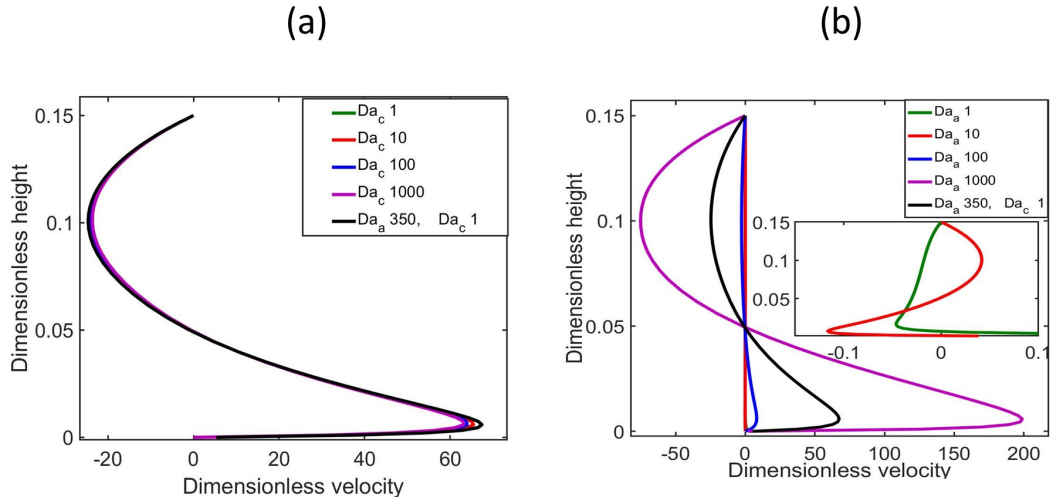

Figure 4.9: Variation of the axial flow velocity along the y-axis from electrodes junction for (a) Cathodic Damköhler numbers Da_c. (b) Anodic Damköhler number Da_a. Inset: flow reversal at $Da_a < 100$.

the bielectrode length are made constant in this regard. The rate constant depends on the reactivity and surface properties of the metal [9]. We prepared a solution of H_2O_2 and negative tracers, whose molarity (2 mM) and bulk pH (pH = 5) corresponds to a low anodic reactivity regime ($Da_a = 58$). The bulk pH was experimentally adjusted through the addition of HCl. During the electrocatalytic reaction, the fluid flow is indeed completely reversed, where negatively charged particles are observed to be transported from gold to platinum that contrasts the normal electroosmotic flow pattern (see supplementary material video 3 [1]).

The cause of the flow reversal is further traced by examining the ionic species concentration and pH profile at the electrodes and bulk region within the catalytic system (figure 4.10). At $Da_a < 100$, the amount of inert chloride ions dominates that of H^+ and OH^-, and it causes an imbalance in the charge density that that contributes to the flow reversal. As the oxidation rate is increased ($Da_a > 100$) the effect of chloride ions diminishes, and the normal flow from Pt to Au is obtained (figure 4.10a). The proton gradient that triggers the electrokinetic processes diminishes at lower Da_a regimes, thereby contributing to the observed flow reversal, while for higher Da_a numbers, the proton

gradient becomes more pronounced, which corresponds to the reaction regime where the normal flow is obtained (figure 4.10b).

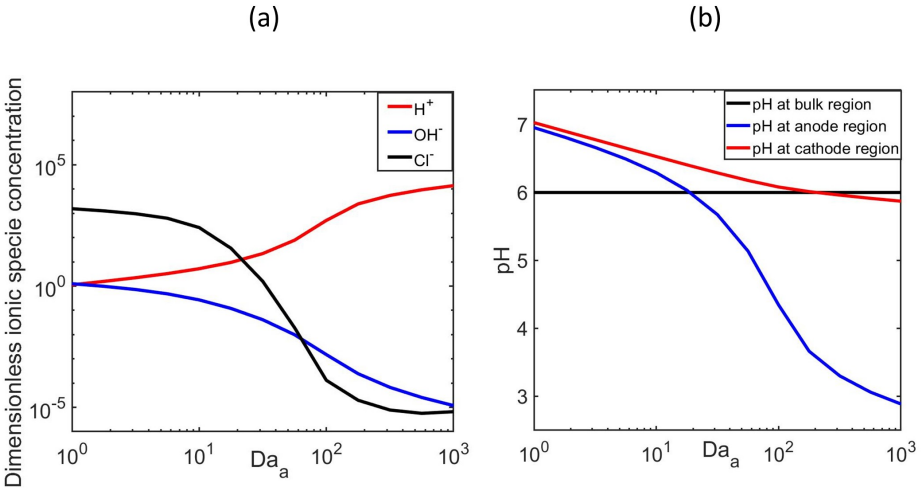

Figure 4.10: Effects of Da_a on (a) Ionic species concentration. (b) average pH at the electrodes and bulk region.

4.5 Conclusion

Electrocatalytic reaction driven flow has been studied by focusing on experimental and numerical analysis that give fundamental insights on the key elements. These include the generated electric field, reaction kinetics and diffusio-electro-osmotic phenomena that control the resulting mass transport characteristics. The electrocatalytic current between the electrodes and the induced potential that governs the reactive fluxes are measured electrochemically while the fluid flow is visualized via particle tracking. The velocity magnitude is influenced by changes in electrolyte concentration and pH. Numerical simulations reveal the synergy between the electrodes surface reactivity contrast which controls the production and depletion of protons with the resulting fluid flow. Flow reversal occurs at low anodic Damköhler numbers and is associated with a weak proton gradient coupled with a charge density imbalance. The key findings regarding the electrolyte concentration, bulk proton concentration and electrodes reactivity are crucial for electrocatalytic processes.

S1 Electrodes zeta potential measurement

Here we evaluated the zeta potential determined for gold and platinum electrodes from streaming current measurements. This was conducted within an adjustable cell using an electrokinetic analyzer equipment (SurPASS, Anton Paar). The streaming current is generated when a dilute electrolyte is driven by a pressure difference dp/L between two planar substrate containing the electrodes, while the zeta potential is computed using the Helmholtz-Smoluchowski equation.

$$\zeta = \frac{dI}{dp} \times \frac{\eta}{\varepsilon} \times \frac{L}{A} \tag{S1}$$

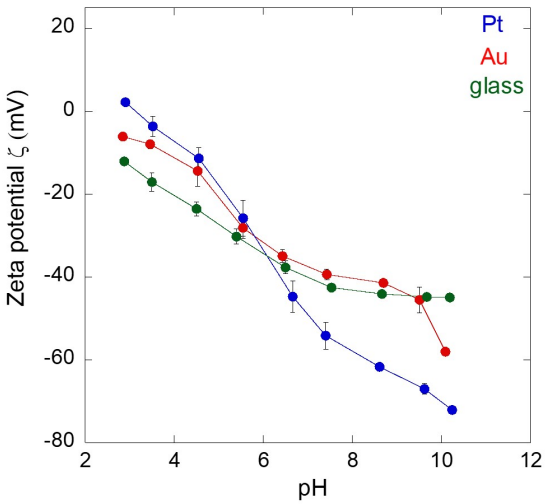

Figure S1: Zeta potential measurements as a function of pH for platinum, gold and glass.

The cell constant is denoted as L/A, where A is the cross-sectional area and L the channel length, and dI/dp is the streaming current change with applied pressure. The zeta potential was evaluated as a function of pH in a 5 mM KCl solution, by titrating the solution with NaOH or HCl (0.1 M) in order to vary the pH of the solution. The zeta potential measurement for the metals and glass are shown in figure S1 where the zeta potential becomes highly negative

at higher pH regime and less negative at lower pH.

S2 Tracer particles zeta potential measurement

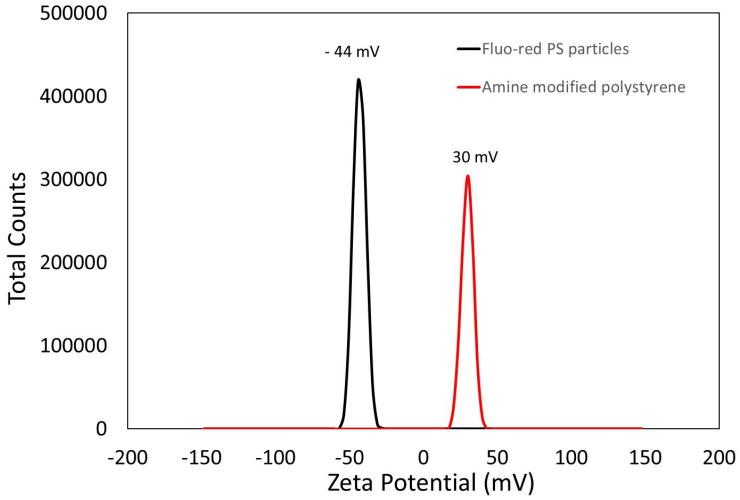

Figure S2: Tracer particles zeta potential distribution, negative particles (carboxylated-modified polystyrene), positive tracer particles (amidine modified polystyrene).

The mean zeta potential for negative and positive tracer particles (carboxyl-modified polystyrene, FluoSpheres^{TM}, and amidine latex beads, Fischer scientific), are measured in 5 mM KCl at pH 6 (figure S2). We found that the particles zeta potential is not severely affected by the pH range (5-6) within which our experiments were conducted.

S3 Comparison of experimental and numerical results for the velocity magnitude

The velocity of the tracer particles is described by Newton's second law

$$m_p \frac{d\mathbf{u}_p}{dt} = \mathbf{F}, \tag{S2}$$

where m_p is the particle mass and $\mathbf{F}$ is the net force acting on the particle and. The net force consists of both the drag force $\mathbf{F}_d$ and the electrophoretic

force $\mathbf{F}_{ep}$

$$\mathbf{F} = \mathbf{F}_d + \mathbf{F}_{ep} \tag{S3}$$

The drag force acting on the particles of radius r moving through peroxide solution with velocity $\mathbf{u}$ is expressed as

$$\mathbf{F}_d = 6\pi r\eta\mathbf{u} \tag{S4}$$

The electrophoretic force is derived based on the product of the Stokes' drag constant $d = 6\pi$ and the electrophoretic velocity $\mathbf{u}_{ep} = \frac{\varepsilon}{\eta}\zeta_{p+}\mathbf{E}$ as

$$\mathbf{F}_{ep} = 6\pi r\eta\mathbf{u}_{ep} \tag{S5}$$

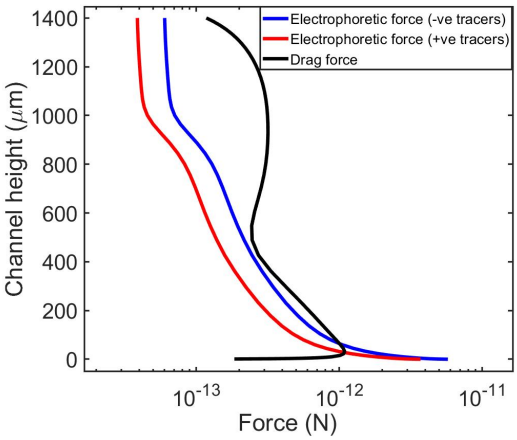

Figure S3: Variation of the forces acting on the tracer particles along the channel height.

Here we formulate a simple analytical expression that can be fitted with the upper parabola of the experimental fluid flow velocity to determine the surface velocity u_s along the channel height in the y-direction. We begin with a simplified form of the Stokes equation, where the advective-inertial term is neglected for a steady state condition and $\nabla p = 0$ to obtain a second order partial differential equation (PDE).

$$\eta\frac{\partial^2 u}{\partial y^2} = 0 \tag{S6}$$

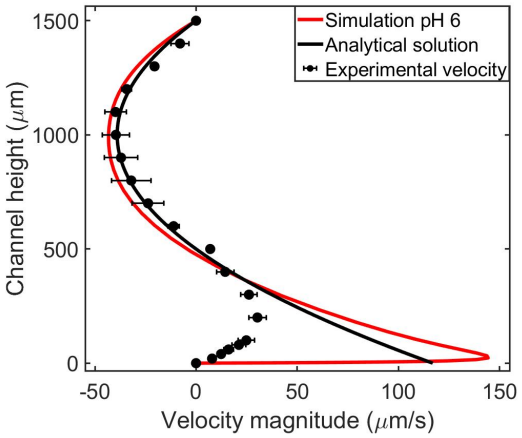

Figure S4: Velocity magnitude for Pt-Au bielectrode in 0.3 M H_2O_2 (pH 6) for experiments fitted with an analytical solution, and simulations. The filled symbols indicate experimental data, the red solid line depicts simulation data, and the solid black line is the analytical solution fitted to the experimental data.

This parabolic PDE can be reformulated in a form of a quadratic equation

$$a\tilde{y}^2 + b\tilde{y} + c = 0 \tag{S7}$$

Equation S6 is solved with boundary conditions u=u_s at $y = 0$, and u= 0 at $y = 1$. By integrating equation S6 along the channel height mass is conserved

$$\int_0^1 \left(a\tilde{y}^2 + b\tilde{y} + c\right)\, dy = 0 \tag{S8}$$

and solving for a and b gives

$$u(y) = u_s(3y^2 - 4y + 1) \tag{S9}$$

We have used this equation to fit the experimental velocity values in the upper part of the volume, in order to extract the surface velocity at the electrode.

S4 Fluid flow reversal

At $Da_a < 10$, the catalytically induced fluid flow is reversed and is driven from the cathode (Au) to the anode (Pt) (figure S5a). The flow magnitude generated at the bielectrode junction is lower and its direction differs from the normal electroosmotic flow pattern induced at $Da_a = 1000$ (figure S5b).

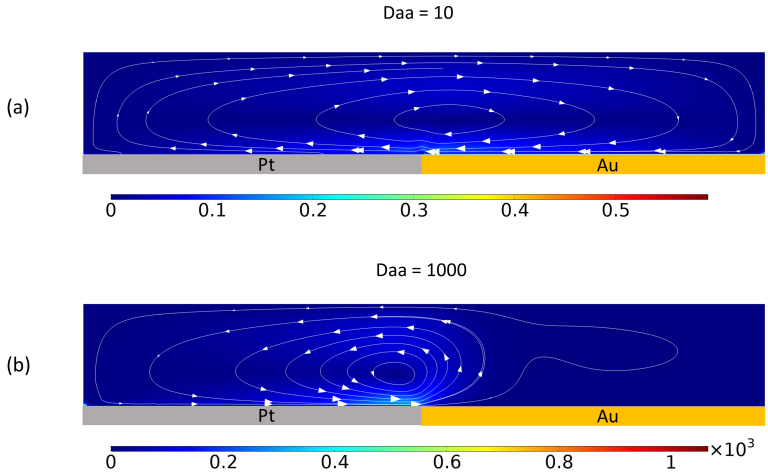

Figure S5: Flow Hysteresis generated by changes in Da_a as indicated by the velocity vector plot (a) flow reversal at $Da_a = 10$. (b) Electroosmotic flow at $Da_a = 1000$.

References

[1] [n.d.]. see Supplemental Material for movies 1 and 2 at `https://figshare.com/s/92c4056d7efd3bc90bdc`.

[2] Agar, J. [1967]. Double layer and electrode kinetics: by paul delahay, *Journal of Electroanalytical Chemistry and Interfacial Electrochemistry* **13**(4): 472.

[3] Bard, A. J. and Faulkner, L. R. [2015]. Electrochemical Methods: Fundamentals and Fundamentals and Applications, Vol. 8.

[4] Barnkob, R., Kähler, C. J. and Rossi, M. [2015]. General defocusing particle tracking, *Lab on a Chip* **15**(17): 3556–3560.

[5] Bazant, M. Z., Chu, K. T. and Bayly, B. J. [2005]. Current-voltage relations for electrochemical thin films, *SIAM Journal on Applied Mathematics* **65**(5): 1463–1484.

[6] Biesheuvel, P., van Soestbergen, M. and Bazant, M. [2009]. Imposed currents in galvanic cells, *Electrochimica Acta* **54**(21): 4857 – 4871.

[7] Burdick, J., Laocharoensuk, R., Wheat, P. M., Posner, J. D. and Wang, J. [2008]. Synthetic nanomotors in microchannel networks: Directional microchip motion and controlled manipulation of cargo, *Journal of the American Chemical Society* **130**(26): 8164–8165.

[8] Corbett, J. C., McNeil-Watson, F., Jack, R. O. and Howarth, M. [2012]. Measuring surface zeta potential using phase analysis light scattering in a simple dip cell arrangement, *Colloids and Surfaces A: Physicochemical and Engineering Aspects* **396**: 169 – 176.

[9] Davidson, S. M., Lammertink, R. G. and Mani, A. [2018]. Predictive model for convective flows induced by surface reactivity contrast, *Physical Review Fluids* **3**(5): 1–16.

[10] Druzgalski, C. L., Andersen, M. B. and Mani, A. [2013]. Direct numerical simulation of electroconvective instability and hydrodynamic chaos near an ion-selective surface, *Physics of Fluids* **25**(11).

[11] Duval, J., Kleijn, J. M. and Van Leeuwen, H. P. [2001]. Bipolar electrode behaviour of the aluminium surface in a lateral electric field, *Journal of Electroanalytical Chemistry* **505**(1-2): 1–11.

[12] Esplandiu, M. J., Afshar Farniya, A. and Reguera, D. [2016]. Key parameters controlling the performance of catalytic motors, *Journal of Chemical Physics* **144**(12).

[13] Farniya, A. A., Esplandiu, M. J., Reguera, D. and Bachtold, A. [2013]. Imaging the proton concentration and mapping the spatial distribution of the electric field of catalytic micropumps, *Physical Review Letters* **111**(16).

[14] Guo, J., Gallegos, J. J., Tom, A. R. and Fan, D. [2018]. Electric-field-guided precision manipulation of catalytic nanomotors for cargo delivery and powering nanoelectromechanical devices, *ACS Nano* **12**(2): 1179–1187.

[15] Hess, H. and Bachand, G. D. [2005]. Biomolecular motors, *Materials Today* **8**(12 SUPPL. 1): 22–29.

[16] Ibele, M. E., Wang, Y., Kline, T. R., Mallouk, T. E. and Sen, A. [2007]. Hydrazine fuels for bimetallic catalytic microfluidic pumping, *Journal of the American Chemical Society* **129**(25): 7762–7763.

[17] Jun, I.-K. and Hess, H. [n.d.]. A biomimetic, self-pumping membrane, *Advanced Materials* **22**(43): 4823–4825.

[18] Masliyah, J. H. and Bhattacharjee, S. [2005]. Electrokinetic and Colloid Transport Phenomena, John Wiley and Sons.

[19] Mickler, M., Schleiff, E. and Hugel, T. [2008]. From biological towards artificial molecular motors, *ChemPhysChem* **9**(11): 1503–1509.

[20] Moran, J. L. and Posner, J. D. [2011]. Electrokinetic locomotion due to reaction-induced charge auto-electrophoresis, *Journal of Fluid Mechanics* **680**: 31–66.

[21] Moran, J. L., Wheat, P. M. and Posner, J. D. [2010]. Locomotion of electrocatalytic nanomotors due to reaction induced charge autoelectrophoresis, *Physical Review E - Statistical, Nonlinear, and Soft Matter Physics* **81**(6): 1–4.

[22] Park, J. H., Zhou, H., Percival, S. J., Zhang, B., Fan, F.-R. F. and Bard, A. J. [2013]. Open circuit (mixed) potential changes upon contact between different inert electrodes–size and kinetic effects, *Analytical Chemistry* **85**(2): 964–970.

[23] Paxton, W. F., Baker, P. T., Kline, T. R., Wang, Y., Mallouk, T. E. and Sen, A. [2006]. Catalytically induced electrokinetics for motors and micropumps, *Journal of the American Chemical Society* **128**(46): 14881–14888.

[24] Paxton, W. F., Kistler, K. C., Olmeda, C. C., Sen, A., St. Angelo, S. K., Cao, Y., Mallouk, T. E., Lammert, P. E. and Crespi, V. H. [2004a]. Catalytic nanomotors: Autonomous movement of striped nanorods, *Journal of the American Chemical Society* **126**(41): 13424–13431.

[25] Paxton, W. F., Kistler, K. C., Olmeda, C. C., Sen, A., St. Angelo, S. K., Cao, Y., Mallouk, T. E., Lammert, P. E. and Crespi, V. H. [2004b]. Catalytic nanomotors: autonomous movement of striped nanorods, *Journal of the American Chemical Society* **126**(41): 13424–13431.

[26] Sbalzarini, I. and Koumoutsakos, P. [2005]. Feature point tracking and trajectory analysis for video imaging in cell biology, *Journal of Structural Biology* **151**(2): 182 – 195.

[27] Schätzel, K. and Merz, J. [1984]. Measurement of small electrophoretic mobilities by light scattering and analysis of the amplitude weighted phase structure function, *The Journal of Chemical Physics* **81**(5): 2482–2488.

[28] Tatsumi, K., Nishitani, K., Fukuda, K., Katsumoto, Y. and Nakabe, K. [2010]. Measurement of electroosmotic flow velocity and electric field in microchannels by micro-particle image velocimetry, *Measurement Science and Technology* **21**(10): 105402.

[29] Wang, J. [2012]. Cargo-towing synthetic nanomachines: Towards active transport in microchip devices, *Lab on a Chip* **12**(11): 1944–1950.

[30] Wang, W., Duan, W., Zhang, Z., Sun, M., Sen, A. and Mallouk, T. E. [2015]. A tale of two forces: Simultaneous chemical and acoustic propulsion of bimetallic micromotors, *Chemical Communications* **51**(6): 1020–1023.

[31] Wang, Y., Hernandez, R. M., Bartlett, D. J., Bingham, J. M., Kline, T. R., Sen, A. and Mallouk, T. E. [2006]. Bipolar electrochemical mechanism for the propulsion of catalytic nanomotors in hydrogen peroxide solutions, *Langmuir* **22**(25): 10451–10456.

[32] Wiedemair, J., van Dorp, H. D. S., Olthuis, W. and van den Berg, A. [2012]. Developing an amperometric hydrogen peroxide sensor for an exhaled breath analysis system, *Electrophoresis* **33**(21): 3181–3186.

[33] Wu, J., Balasubramanian, S., Kagan, D., Manesh, K. M., Campuzano, S. and Wang, J. [2010]. Motion-based dna detection using catalytic nanomotors, *Nature Communications* **1**(4).

[34] Zhou, C., Zhang, H., Li, Z. and Wang, W. [2016]. Chemistry pumps: a review of chemically powered micropumps, *Lab Chip* **16**: 1797–1811.

Chapter 5

Electrocatalytic Reaction Driven Flow: The role of pH on flow reversal

Abstract

Immobilized bimetallic structures generate fluid flow, which is typically driven from the anodic metal to the cathodic metal similar to an electroosmotic flow. However, under low reactive regimes, the generated flow becomes fully reversed which cannot be explained by the classical electroosmosis theory. This work aims at unraveling the origin and dynamics of this flow hysteresis through a combined experimental and numerical approach. The key electrocatalytic parameters that contribute to flow reversal are analyzed experimentally and numerically under low reactive regimes induced by bulk pH variations. The proton gradient that initiates chemomechanical actuation is probed using fluorescence lifetime imaging. The fluid flow dynamics under reactive regimes are visualized using particle tracking. Our numerical simulations elucidate the role of pH variations and additional ionic species (counterions) towards flow reversal. The combination of these techniques highlights the interplay between electrocatalytic and electrokinetic phenomena on the occurrence of flow reversal.

5.1 Introduction

Artificial micromotors are devices capable of converting energy to forces and movements. They have gained several attention aimed at replicating the complex functionalities of nature [27, 23, 32]. A good example concerns the autonomous motion of catalytic nanorods within a fluid medium that functions primarily on chemical energy conversion harvested from the surrounding aqueous fluid [25, 30]. Their motion is similar to the movement of the flagellum, bacteria, and other biological motors that are powered by chemical energy sourced from adenosine triphosphate (ATP) for vital functions in living organisms. The capabilities of micromotors have been extended through the immobilization of the nanorod in form of a micropump, to fluid flow driven by electrochemical gradients obtained from electrocatalytic reactions [24, 17, 14]. Electrocatalytic reaction driven flow (termed "ERDF") is driven by a self-induced electric field that is generated through a gradient of ionic intermediates, and powered by the decomposition of a fuel catalyzed by a bimetallic pair. A typical bimetallic system consists of platinum and gold electrodes, immobilized on a substrate, that catalyze the electrochemical decomposition of hydrogen peroxide through a series of redox half reactions (5.1 and 5.2). During oxidation reaction at the anode Pt, oxygen is produced, while protons and electrons are generated. Simultaneously, the electrons are transferred to and protons are consumed at the Au cathode via the reduction reaction. The proton flux evolves into a concentration gradient, which creates an electrical body force on the charged near-electrode liquid layer, that drives fluid flow (see Fig. 5.1).

$$\mathrm{H_2O_2} \longrightarrow 2\,\mathrm{H^+} + \mathrm{O_2} + 2\,\mathrm{e^-} \tag{5.1}$$

$$\mathrm{H_2O_2} + 2\,\mathrm{H^+} + 2\,\mathrm{e^-} \longrightarrow \mathrm{H_2O} \tag{5.2}$$

ERDF has been explored in various instances, such as the enhancement of mass transport across a membrane in a compartment-less fuel cell [16], oxygen generation [22], and colloidal crystallization [2, 26]. The reaction mechanism involving proton generation and consumption, as well as its impact on the reaction kinetics and the resulting fluid flow is not fully understood. The interplay between these coupled phenomena under different reaction regimes is the main focus of this thesis. Many studies have focused on the chemomechanical mechanism that drives ERDF, and they will be briefly highlighted. The fuel that powers chemical energy conversion has been a subject of interest in some studies. Hydrogen peroxide decomposition has been central to many proof-of-concept works, however other fuel substitutes such as hydrazine

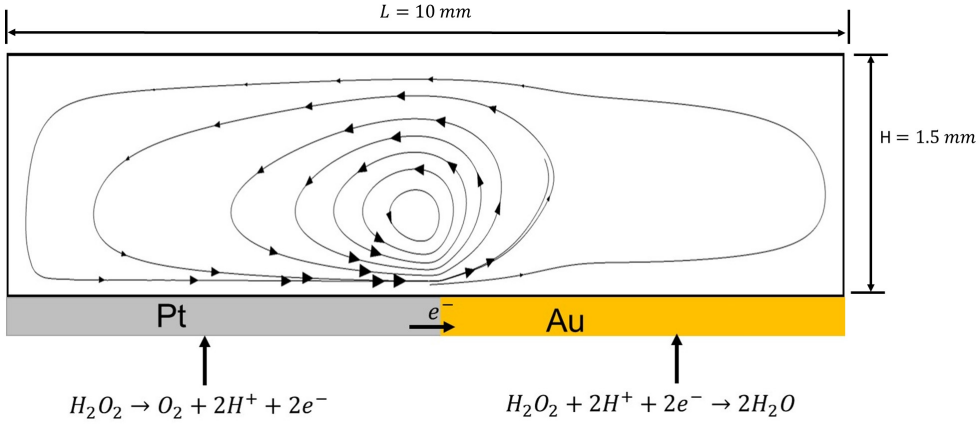

Figure 5.1: Schematic of the Pt-Au bimetallic system that catalyzes the decomposition of hydrogen peroxide.

derivatives and iodine have found relevance in generating ERDF, which eliminates the complexities of oxygen bubbles associated with peroxide decomposition [14, 33]. The reactivity of the bimetallic metals is central to an electrochemical conversion that generates ERDF. For this reason, highly reactive metallic pairs that promote electrocatalytic conversion have been researched as suitable alternatives to the classical Pt-Au bimetallic pair [31].

The electrochemical conversion has been characterized using direct current-potential measurements [24] and TAFEL analysis [31, 12], where the potential induced during the electrochemical reaction and the catalytic current that is associated with the reaction kinetics are measured. The resulting fluid flow concerned an electroosmotic flow pattern where the flow is driven from the anode to the cathode and recirculates within a confined system [24, 17]. The velocity magnitude, albeit highly sensitive to pH variations can be tuned by the fuel concentration [3].

Flow reversal occurs whenever the induced fluid flow that is typically driven from the anode to the cathode becomes redirected in the sense opposite to an electroosmotic flow. According to the Helmholtz Smoluchowski equation, the zeta potential ζ is an important parameter that contributes to electroosmotic flow velocity $\mathbf{u}$, and its sign convention dictates the flow direction. Subramanian and Catchmark [28] experimentally demonstrated flow reversal by re-engineering the zeta potentials of the bimetallic electrode [28]. They coated

the electrode surface with self-assembled monolayers that modifies the surface charge and the resulting zeta potential sign. For the case where the zeta potential of the electrode was made positive, the flow becomes reversed. The Helmholtz Smoluchowski equation for flow is given as $\mathbf{u} = -\frac{\varepsilon}{\eta}\zeta\mathbf{E}$, where ε is the permittivity of the fluid, $\mathbf{E}$ is the electric field.

Aside from the flow reversal governed by the zeta potential switch, flow reversal can be induced by the electric field reversal that stems from the electrocatalytic reaction. Ibele et al. [14] reported reversal of flow based on the fuel choice that impacts the induced potential and tangential electric field. Two variants of hydrazine were used for this purpose, N_2H_4 and $N_2Me_2H_2$ with a $Au - Pd$ bimetallic system. The electrodes exhibited different roles for these fuel variants as evidenced by their mixed potential, where Au having a higher mixed potential (-310 mV) for N_2H_4 assumes the cathodic role, and flow is driven towards it. In the case where $N_2Me_2H_2$ was used, the role of the electrodes became reversed and Pd having a higher mixed potential (-70 mV) act as the cathode with flow being driven from Au to Pd. Although, they described the flow direction as being governed by the resultant effects of the electrode zeta potential in conjunction with the zeta potentials of the colloidal particles, the different mixed potentials exhibited by the electrodes in different solutions, would create variations in the bimetallic potential, which have consequences for the electric field and strengthens the argument for a flow reversal that is driven by the electrocatalytic reaction.

In an earlier paper, we reported the observation of flow reversal under low anodic reactive regimes ($\mathrm{Da}_a < 100$) [3]. The anodic Damköhler number, Da_a, defines the rate at which oxidation reaction proceeds that leads to the generation of protons. The slow oxidation reaction becomes the overall limiting mechanism, and the proton gradient across the bielectrode is diminished. The proton gradient serves as the basis for the actuation of the bimetallic system and its weakened form has negative consequences for the induced electric field and body forces that drive the fluid flow. However, the dynamics of the proton gradient under reactive regimes and the effects on the fluid flow are yet to be fully understood. It is the aim of this study to investigate the interplay between these two main phenomena.

Fluorescence imaging has emerged as a useful tool for probing electrode-electrolyte interfacial processes [19, 10, 9, 5] as well as ion transport in systems [8, 4]. Such technique involves the use of an ionic chemical species that modulates directly or indirectly a fluorescence signal that emanates from a reaction mechanism. The modulation could be a change in quantum yield or emission

wavelength, which directly affects the amplitude of the signal [9]. Farniya et al. [12] employed fluorescence intensity based on ratiometric measurements to track the proton gradient during the catalytic reaction involving Pt-Au in H_2O_2. They showed that the proton concentration changes by almost an order of magnitude along the radial direction of the bielectrode. However, this technique has its limitation as the fluorophores have the tendency to photobleach, which affects the accuracy of the result. Moreover, fluorescence intensity is highly sensitive to the dye concentration which can be severely impacted by the surface induced electroosmotic flow. Fluorescence lifetime imaging (FLIM), on the other hand, is based on the average decay time of a fluorophore's excited state, depending on its interactions with ions and dynamics in the system [18]. FLIM offers key advantages over fluorescent intensity in terms of insensitivity to the fluorescent dye concentration and excitation intensity [6], and spatial-temporal resolution.
Based on these benefits, the reaction-induced proton gradient at the bielectrode/electrolyte interface was characterized with the fluorescence lifetime imaging (FLIM) technique. Furthermore, a two-dimensional model based on the Poison-Nernst-Planck and Stokes equations was formulated, to elucidate the role of the proton gradient on the induced electric field and other key elements that control the resulting mass transport characteristics. The reaction regimes that concerns ERDF and reversed flow are fully analyzed. A complete understanding of the reaction driven fluid flow opens more opportunities for fluid control and exploitation in targeted systems.

5.2 Experimental details

Pt-Au bimetallic and interdigitated electrodes were fabricated on planar glass substrates via photolithography, metal sputtering, and liftoff. The glass substrates were spin-coated with positive photoresist, followed by exposure to UV-light through a photomask and development. Tantalum was pre-sputtered on the substrates to improve adhesion, before depositing platinum and gold metals through DC sputtering (MESA+ nanolab cleanroom in-house equipment,"TCOathy"). The photoresist negative pattern was removed via a liftoff process in acetone. A schematic diagram for both design variants is presented in figure 5.2. Before any experimental measurements, the bielectrodes were cleaned of organic contaminants and photoresist residues by thoroughly cleaning and rinsing with isopropyl alcohol and DI water, followed by oxygen plasma treatment (plasma power = 100 W, oxygen gas pressure = 0.5 bar, 5 minutes).

The interdigitated electrode is designed primarily for electrochemical experiments and was bonded on a printed circuit board that allows connection to a potentiostat. The bimetallic electrodes are used for the FLIM and fluid flow characterization with the aid of an imaging chamber that confines the electrolyte solution with the immobilized bielectrode.

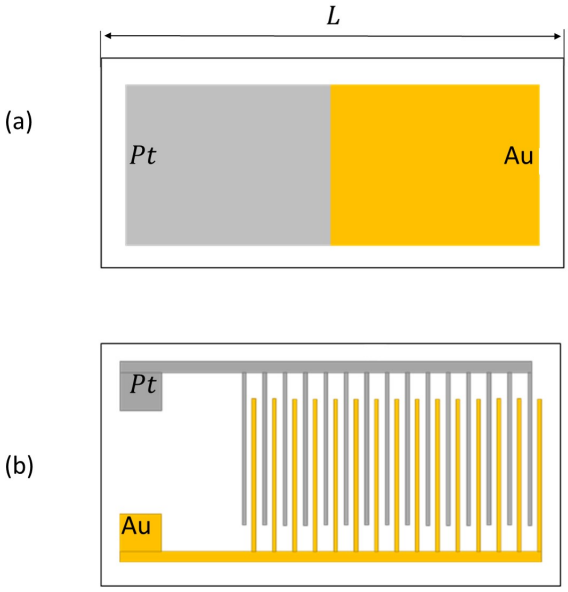

Figure 5.2: Schematic diagram showing the Pt-Au (a) Bimetallic electrodes with total length L = 10 mm. (b) Interdigitated electrodes with interspacing S = 40 μm and electrode width W = 50 μm.

5.2.1 Fluid flow visualization

To visualize the induced flow patterns, we introduced fluorescent particles (carboxylated-modified FluoSpheres^{TM}), 1 μm in diameter, in hydrogen peroxide solutions (Sigma Aldrich), which were prepared in MilliQ water ($\rho > 18$ MΩ.cm). The pH of the resulting mixture was adjusted with HCl or NaOH. The conductivity of the prepared solutions was measured with a conductivity probe (WTW Cond 3110, Weilheim, Germany) to be in the range of 10 to 30 μS/cm. The particle movement that was driven by the fluid flow was observed using an inverted optical microscope (Carl Zeiss Axio Observer Z1, 20x), while images were acquired at a frame rate of 10 fps. Image processing was con-

ducted using ImageJ and the particle displacement vectors were obtained with the open-source tool PIVlab [29].

5.2.2 Fluorescence Lifetime imaging of proton gradient

The proton concentrations close to the surface of the bielectrode were determined using fluorescence lifetime imaging microscopy (FLIM), (LIFA, Lambert Instruments). The FLIM setup consists of an image intensifier (TRiCAM), frequency generator and LED light source (3 W, emission wavelength of 460 nm), which are connected to a Zeiss Axio Vert A1 inverted microscope (Zeiss, Germany) that is equipped with a filter cube (443-493 nm band-pass excitation, 500-650 nm band-pass emission). Data acquisition and processing were performed under the frequency domain mode using LI-FLIM software. A homodyne detection method was used in extracting the phase shift and modulation depth data from the acquired fluorescence signal, by modulating the light source and the intensified camera at a modulation frequency of 40 MHz and a phase angle of 250 degrees. The modulation frequency f is the optimal frequency at which small changes of the lifetime for the sample being studied can generate large response in terms of the phase shift and modulation depth and is determined using $\frac{1}{2\pi\tau}$, where τ is the fluorescent lifetime. For every data acquisition, twelve images were obtained from different phase offsets, while the phase shift and modulation depth that yields the lifetime for each pixel were determined by fitting the fluorescence signal with a sine function. For the FLIM experiments, hydrogen peroxide solutions containing LysoSensor pH probe (LysoSensor green DND-189, ThermoFisher scientific) were used. The LysoSensor pH probe can fluoresce within an acidic to near-neutral medium (indicative of pH range 5-6). Before the FLIM measurements, calibration experiments were performed under bulk pH conditions to ascertain the relationship between the pH and the fluorescence lifetime of the LysoSensor probe. Samples consisting of the LysoSensor probe and pH buffers (phosphate buffer, Potassium hydrogen phthalate Thermo Fisher Scientific) were prepared within the pH range 4 to 9, while the pH was adjusted accordingly by HCl or NaOH.

The calibration curve for the fluorescence lifetime experiments was obtained for known pHs of LysoSensor-buffer solutions by fitting the plot of the lifetime vs. proton (H^+) concentration with the Boltzmann sigmoid equation (Fig.5.3)

$$\tau(ns) = A_2 + \frac{A_1 - A_2}{1 + e^{\frac{pH - pKa}{dx}}} \tag{5.3}$$

where A_1 and A_2 are the upper and lower limits of the fluorescence lifetime respectively, and dx is the slope at the inflection point. The calibration curve demonstrates a steep transition and a high sensitivity between pH 5 and 6 due to the quantum yield of the LysoSensor probe during protonation. The protonation process mitigates the fluorescence quenching of the dye molecule, by its weakly basic chain that results to an increase in fluorescent intensity and lifetime signals [20]. The Boltzmann sigmoid fit yielded an apparent pKa of 5.77, comparable to what was reported in other works [20, 15]

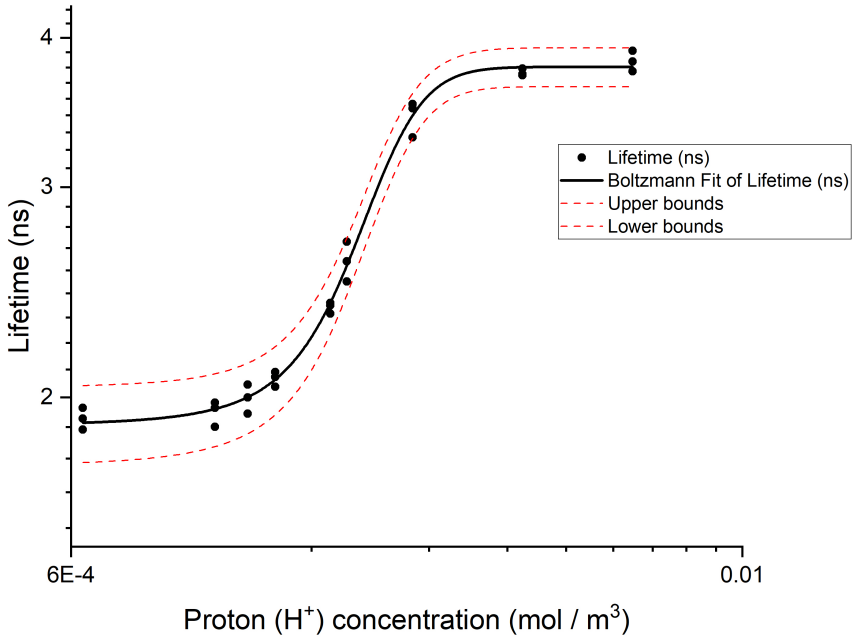

Figure 5.3: Lifetime vs proton concentration calibration curve for FLIM measurements on semi-log scale. Solid line corresponds to the best fit to a Boltzmann sigmoid model.

5.3 Theory and numerical simulation

Following our previous work, we developed a 2D numerical model that is based on the dimensionless Poisson-Nernst-Planck equations for the transport of ionic species, coupled with the Stokes equation for the fluid flow (see chapter 4). As shown in figure 5.1 the model is built with an aspect ratio of $H/L = 0.15$, that is representative of our experimental setup consisting of a channel depth $H = 1.5$ mm and bielectrode length $L = 10$ mm.

5.3.1 Governing equations

The concentration of ionic species are coupled with the induced potential ϕ through the Poisson's equation (5.4) to resolve the induced potential distribution.

$$-2\epsilon^2\nabla^2\phi = \Sigma_i z_i c_i \tag{5.4}$$

At the interface between the bielectrode and the electrolyte solution, a double layer is formed whose thickness is given by the Debye length $L_D = \sqrt{\frac{\varepsilon V_T}{2Fc_\infty}}$ and is normalized with the length of the bielectrode $\epsilon = \frac{L_D}{L}$. The thickness of the Debye length for the electrolyte at pH=6 is 304 nm.
The transport of ionic species is accounted for by the Nernst-Planck equation (5.5) by solving the advection, diffusion, and electromigration contributions involving the 1 : 1 electrolyte.

$$\frac{\partial c_i}{\partial t} + \nabla\cdot(\mathbf{u}c_i) = D_i\nabla\cdot(\nabla c_i + z_i c_i\nabla\phi) + R_i \tag{5.5}$$

where $\mathbf{u}$ is the velocity magnitude and c_i is the concentration of ion i whose diffusion coefficient and valence are D_i and z_i respectively. The self-ionization water is included as a bulk reaction R_i, defined as $R_i = \mathrm{Da}_b\left(\frac{K_w}{c_\infty^2} - c_{\mathrm{H}^+}c_{\mathrm{OH}^-}\right)$, where K_w is the water ionization constant expressed as $\mathrm{K}_w = [\mathrm{H}^+][\mathrm{OH}^-] = 1\times10^{-14}$ M^2. Da_b is the bulk Damköhler number defined as $\mathrm{Da}_b = \frac{k_{rb}L^2c_\infty}{D_0}$, k_{rb} is the water recombination reaction rate constant, c_{H^+} and c_{OH^-} are the concentrations of proton and hydroxyl species respectively.
The induced fluid flow is described by the dimensionless continuity and Stokes equations (5.6 and 5.7) and is assumed incompressible under steady-state conditions. The flow is characterized under low Reynolds regime, hence we set the nonlinear inertial term in 5.7 as $\frac{1}{\mathrm{Sc}}\frac{\partial\mathbf{u}}{\partial t} = 0$. Here, Sc is the Schmidt number defined as $\mathrm{Sc} = \frac{\eta}{\rho D_0}$ and of $O(10^3)$, D_0 is the diffusivity of hydroxide ions which

is an arbitrary reference value, $\kappa = \frac{\varepsilon V_T^2}{\eta D_0} = 0.093$ is the electro-hydrodynamic coupling constant.

$$\nabla \cdot \mathbf{u} = 0 \tag{5.6}$$

$$\frac{1}{\mathrm{Sc}} \frac{\partial \mathbf{u}}{\partial t} = -\nabla p + \nabla^2 \mathbf{u} - \frac{\kappa}{2\epsilon^2} \rho_e \nabla \phi \tag{5.7}$$

5.3.2 Boundary conditions

We impose a no-slip condition, $\mathbf{u} = 0$, on all boundaries for Stokes' equations. For the potential boundary condition, we apply a mixed Neumann/Dirichlet expression to resolve the potential field and the electric double layer, by coupling the potential boundary condition at the surface of the electrodes (y=0) to the zeta potential for the respective electrodes $\phi_{electrode} = \zeta_{electrode}$. The model resolves the diffuse part of the electric double layer, while the Stern layer is resolved by scaling the zeta potential ζ with the potential drop across the Stern layer ($\Delta\phi_{Stn}$) (5.8) and the ratio between Stern layer length L_{Stn} and the Debye length L_D (5.9).

$$\Delta\phi_{Stn} = \zeta - \phi_{electrode} \tag{5.8}$$

$$\Delta\phi_{Stn} \approx \frac{L_{Stn}}{L_D} \zeta \tag{5.9}$$

For the case of an electrolyte having a low salt concentration $\frac{L_{Stn}}{L_D} \ll 1$, and $\Delta\phi_{Stn}$ is extremely small, hence eq.5.8 becomes $\phi_{electrode} \cong \zeta$. At the upper boundary of the model (y=0.15), we apply $\frac{\partial \phi}{\partial y} = 0$. The proton flux that results from the electrocatalytic reaction is applied on the surface of the bielectrode according to

$$n.j_{\mathrm{H^+}} = n \cdot (D_{\mathrm{H^+}} \nabla c_{\mathrm{H^+}} + z_{\mathrm{H^+}} c_{\mathrm{H^+}} \nabla \phi - \mathbf{u} c_{\mathrm{H^+}}) = \begin{cases} j_{Pt} = D_{\mathrm{H^+}} \mathrm{Da}_a \\ j_{Au} = D_{\mathrm{H^+}} \mathrm{Da}_c c_{\mathrm{H^+}}^2 \end{cases} \tag{5.10}$$

where j_{Pt} and j_{Au} represents the platinum and gold surface proton flux respectively. The oxidation and reduction reaction that occurs at Pt and Au metals are characterized by the anodic Damköhler number $\mathrm{Da}_a = \frac{k_a L c_{\mathrm{H_2O_2}}}{D_+ c_\infty}$, and the cathodic Damköhler number $\mathrm{Da}_c = \frac{k_c L c_\infty c_{\mathrm{H_2O_2}}}{D_+}$ respectively. The flux of anionic species are set to zero at the surface of the bielectrode, giving

$$n \cdot j_{\mathrm{OH^-}} = n \cdot (D_{\mathrm{OH^-}} \nabla c_{\mathrm{OH^-}} + z_{\mathrm{OH^-}} c_{\mathrm{OH^-}} \nabla \phi - \mathbf{u} c_{\mathrm{OH^-}}) = 0 \tag{5.11}$$

$$n \cdot j_{\mathrm{Cl^-}} = n \cdot (D_{\mathrm{Cl^-}} \nabla c_{\mathrm{Cl^-}} + z_{\mathrm{Cl^-}} c_{\mathrm{Cl^-}} \nabla \phi - \mathbf{u} c_{\mathrm{Cl^-}}) = 0 \tag{5.12}$$

At the upper boundary of the model, we set the initial concentration for each ionic species $c_\infty i$ as a Dirichlet condition that is coupled to the bulk electrolyte pH through $(-\log_{10}(c_\infty))$. The pH of the electrolyte was adjusted during experimental studies with HCl. This was included in the model by using an expression that accounts for the bulk proton concentration due to bulk pH variations, electroneutrality, and other limiting conditions involving water self-ionization (5.10) (Full derivation can be seen in section 3.4).

$$\mathrm{H^+} = \frac{\mathrm{c_\infty} + \sqrt{[\mathrm{c_\infty}]^2 + [4\mathrm{K}_w]}}{2} \tag{5.13}$$

5.3.3 Simulation method

Simulations were performed based on the bimetallic current (0.06 $\mathrm{A/m^2}$) that was measured from Tafel plots obtained from electrochemical measurements for the case of 2 mM H_2O_2 at pH=6 (see section S1). The current was converted to reaction flux (in mol $\mathrm{m^{-2}\ s^{-1}}$) and applied directly to the electrode as a Dirichlet boundary condition. The effective rate constants for the redox reactions are extracted by using the Frumkin-corrected Butler-Volmer equation

$$j_{\mathrm{H^+}} = k_a c_{\mathrm{H_2O_2}} \exp(\frac{(1-\alpha)nF\Delta\phi_{Stn}}{RT}) - k_c c_{\mathrm{H_2O_2}} c_{\mathrm{H^+}}^2 \exp(\frac{-\alpha nF\Delta\phi_{Stn}}{RT}) \tag{5.14}$$

where $j_{\mathrm{H^+}}$ is the proton flux expressed from the measured current density through Faraday's law, n is the number of electrons transferred during the reaction. k_a represents the anodic rate constant ($k_a = 1.63 \times 10^{-7}$ m/s) and k_c is the cathodic rate constant ($k_c = 5.16 \times 10^{-4}\ \mathrm{m^7\ s^{-1}\ mol^{-2}}$). Both rate constants are used in determining the Damköhler numbers, found to be $\mathrm{Da}_a = 350$ and $\mathrm{Da}_c = 1$ respectively (see Eqs 4.8 and 4.9).

Numerical computations were performed using the finite element method (FEM) method in COMSOL Multiphysics 5.5. The mesh near the electrode/electrolyte interface was refined to resolve the double layer and to capture the gradients that occur within this region. The model domain is discretized into approximately 10^5 elements, as further mesh refinement yielded relatively no significant change in the maximum velocities.

5.4 Results and discussion

The fluid dynamics that are characterized by the movements of the suspended tracer particles in hydrogen peroxide solution are shown in Fig. 5.4. The electrolyte solution contained 0.3 M hydrogen peroxide, at pH 5.8 and 4.2. The particle movements were recorded at about 300 μm above the junction of the bielectrode to ascertain the directionality of the flow. At this location, the particles passively follow the flow such that the resulting particle trajectories are considered to be the fluid flow streamlines (Fig. 5.4a).
Under bulk pH 5.8 condition, the particles are observed to be transported from Pt to Au (see supplementary movie 1, [1]), and the displacement vector confirms the nature of the fluid flow to be electroosmotic that moves in the direction of the cathode from the anode (Fig. 5.4b). Gold in this case serves as the cathode based on its higher mixed potential, as shown in the Tafel curve (Fig. S1). The magnitude of the particle velocity is in the order of 10^{-6} m/s. However, the movements of the charged particles appear to be slightly retarded around $y \leq 100\mu$m, due to the electrophoretic force that originates from the induced electric field around this region (Fig. S2a).
At bulk pH 4.2 the pumping direction is completely inverted and particles are advected from Au to Pt, which indicates a completely reversed flow (Fig. 5.4c, supplementary movie 2 [1]). The particle velocity in this case is an order of magnitude lower than the case of pH=5.8. The movement of the particles, in this case, is observed to be completely affected by the electrophoretic force throughout the channel that becomes substantial when compared to the drag force, and even stronger near the surface of the bielectrode, $y \leq 25$ μm (Fig. S2b). The dominance of the electrophoretic force under these conditions make the extraction of the surface-induced fluid velocity more challenging.
The fluid flow features that are obtained from both bulk pH conditions indicate different reaction regimes that result in diverse flow behaviors. The reaction regimes, which we characterized by the dimensionless anodic Damköhler number Da_a, controls the generation of proton that influences the proton gradient. The proton gradient plays an important role in fluid flow generation via the self-induced electric field as will be shown in the subsequent sections.

5.4.1 Fluorescence lifetime Imaging

In this section, we present fluorescent lifetime results that characterize the reaction-induced proton concentration by FLIM. To prevent the disturbance of the fluorescence lifetime signal, the concentration of H_2O_2 was kept very

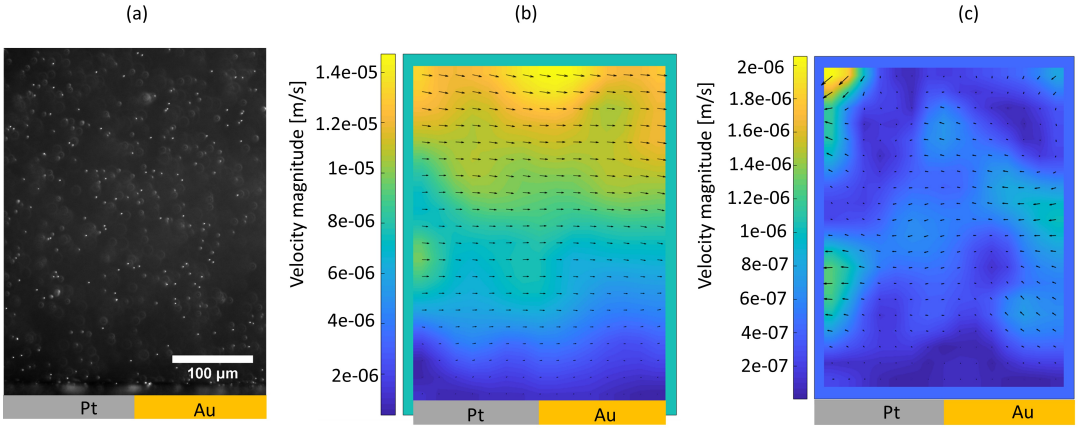

Figure 5.4: (a) Fluid flow visualization by particle movements in 0.326 M H_2O_2 (b) Displacement vectors for fluid flow at bulk pH 5.8 (c) Displacement vectors for the reversed flow at bulk pH 4.2

dilute (2 mM), which minimizes the growth rate of the oxygen bubbles during the reaction.

We first evaluated the performance of the bielectrode using the FLIM technique, by performing a blank test in the absence of hydrogen peroxide with LysoSensor and water solution (Fig. 5.5a). The spatial distribution of the fluorescence lifetime across the bielectrode region in the absence of H_2O_2 appears to be nearly homogeneous as the average lifetime for both electrodes was ≈ 2, which implies no proton asymmetry across the electrodes.

Figure 5.5b shows the spatial variation of the fluorescence lifetime obtained across the bielectrode during the electrochemical reaction involving H_2O_2 (2 mM) at pH 5.8. An increase in the fluorescence lifetime signal is seen near the Pt region by a unit that indicates the enrichment of protons H^+. In this case, the LysoSensor probe within the acidified regions becomes protonated, resulting in an increased lifetime signal. On the other hand, we observed a lower fluorescence lifetime signal near the Au region that indicates a reduction of proton concentration. In general, the average lifetime data demonstrates the establishment of a steady-state proton concentration gradient across the bielectrode, which is necessary for electrocatalytic actuation.

We explored the nature of proton distribution associated with a lower anodic reactive regime by changing the pH of the solution to 4, which corresponds to

$Da_a = 58$. the result is shown in Fig 5.5c. It can be seen from Fig 5.5c that the

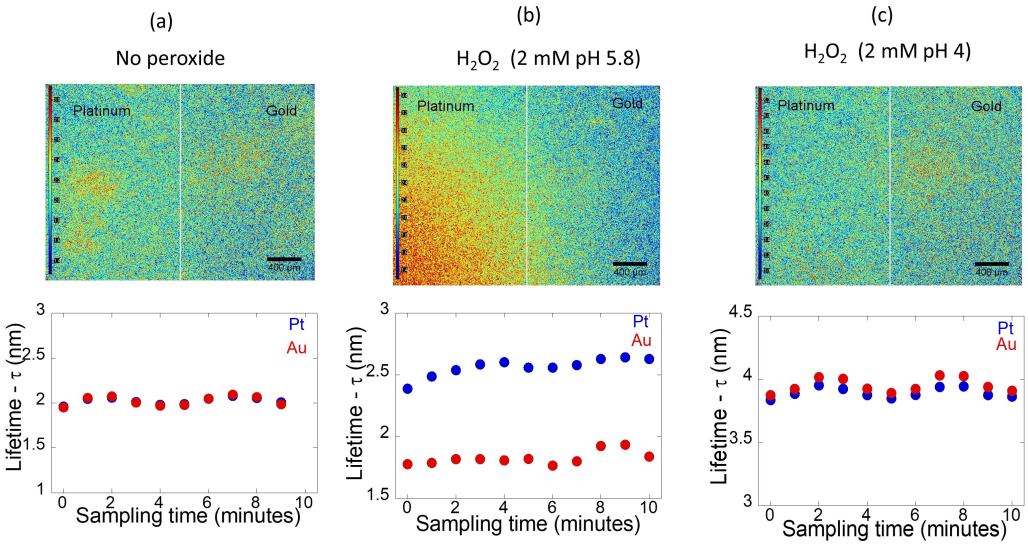

Figure 5.5: Fluorescence lifetime of Pt-Au for (a) No Hydrogen peroxide reaction (b) 2 mM H_2O_2, pH 5.8 (c) 2 mM H_2O_2, pH 4

fluorescence signal across the bielectrode is nearly homogeneous and the proton gradient appears to be diminished. The FLIM result that was obtained for the testcase of bulk pH 5.8 matches well with the simulation result whose solution bulk pH is 5.6. The slight pH deviation occurs due to the unstableness of the unbuffered electrolyte that creates a change in the concentration of H^+ ions. Moreover, the simulation data suggests the establishment of a steeper gradient at the surface of the bielectrode, which highlights the limitation of FLIM towards resolving the near-surface region of the bielectrode (Fig. 5.6). One way to circumvent this would be to couple total internal reflection fluorescence (TIRF) with FLIM to access the near-surface region [13].

5.4.2 Electrocatalytic Reaction Induced Flow Regimes

In this section, we characterized reaction regimes under bulk pH variations and studied their influence on the resulting flow dynamics numerically. The reaction regimes are defined by the reactivity ratio between the anodic and

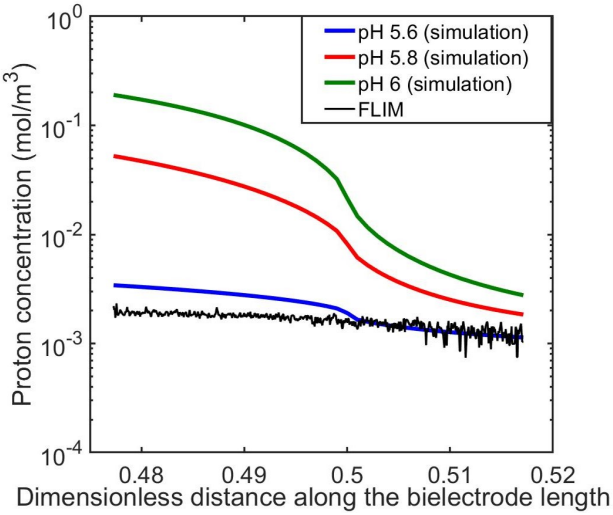

Figure 5.6: Proton concentration profile along the junction of the bielectrode for simulation and FLIM results.

cathodic Damköhler numbers (Da_a/Da_c), and varied to create regimes with different limiting mechanism that controls the overall electrocatalytic process. For each reactivity ratio, simulations were performed by varying the anodic Damköhler number that controls the proton generation rate. The maximum induced velocity is obtained at the junction of the bielectrode max(u(x = 0.5, y = 0)) and plotted versus Da_a numbers (Fig.5.7).

It can be seen for every reactivity ratio in Fig.5.7 that the flow generated under bulk pH 4 is completely reversed, while at pH 7 the normal flow direction is obtained. Fig. 5.7d shows the Da_a transition regimes under different bulk pH conditions below which the flow becomes fully reversed, and above which an electroosmotic flow is obtained. The transition points vary inversely with the electrolyte bulk pH, which indicates the dominance of reactive timescales over diffusion, towards the reestablishment of normal flow under reaction regimes that are prone to flow reversal. This result highlights the interplay between the electrocatalytic and diffusion-reaction towards the generation of surface induced flow, and the conservation of current under bulk pH variations.

We examine further the proton concentration gradient associated with the induced velocities for the case of $Da_a/Da_c = 1$ at bulk pH values of 4, 5.5, and 7. The variation of both Damköhler numbers within this fixed ratio represents

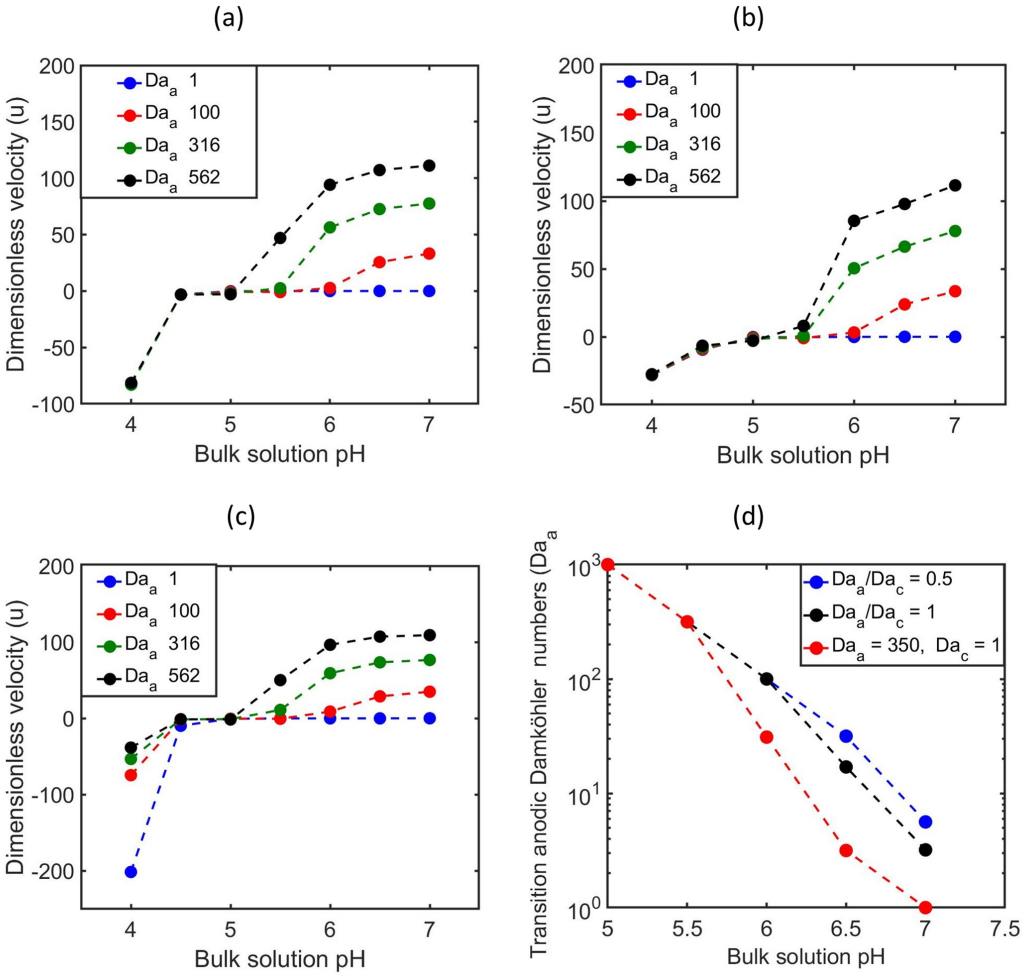

Figure 5.7: Dimensionless velocity magnitude plotted versus pH for reactivity ratio (a) $Da_a/Da_c = 0.5$ (b) $Da_a/Da_c = 1$ (c) $Da_a = 350$, $Da_c = 1.11$ (d) Transition Da_a numbers that indicates the transition from reversed to normal flow and vice versa under different solution pHs. The dotted dashed lines are for visualization purpose only.

the variation of the concentration of H_2O_2. The proton concentration here is defined by the average local pH at the electrode and bulk regions and presented

in (Fig. 5.8). For the case of the bulk pH 7, the proton concentration gradient builds up from the bulk pH and becomes more pronounced with increasing Da_a (Fig. 5.8a). In Fig. 5.8b the local proton concentration for a bulk pH 5.5 presents two distinct forms. At reaction regimes associated with flow reversal, $Da_a \leq 177$, the bulk pH profile falls outside the bounds of the pH profile for the anode and cathode due to the absence of charge asymmetry in the non-neutral zone, whereas from $Da_a \geq 316$, which is under the electroosmotic flow regime, the proton gradient offers a similar behavior as for bulk pH 7 and demonstrates sensitivity to the increased reaction rate . In Fig. 5.8c, the proton gradient obtained for the bulk pH 4 becomes diminished and the flow under this regime is fully reversed.

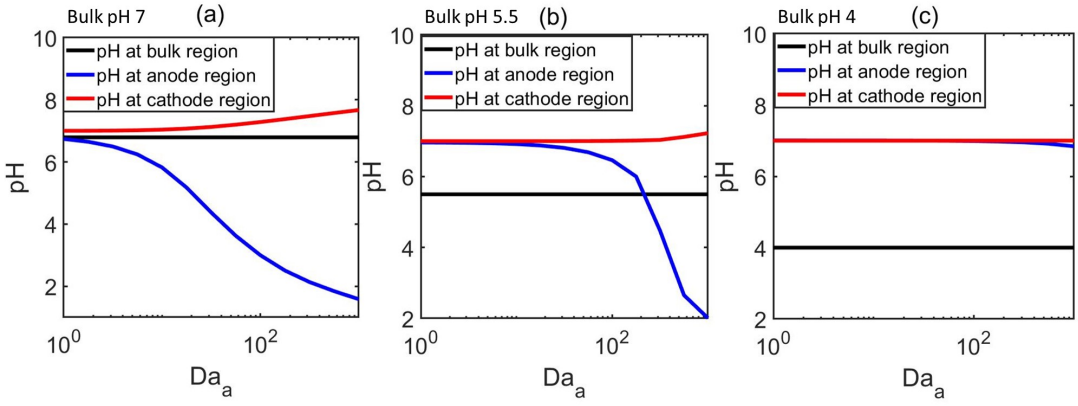

Figure 5.8: Average pH versus Da_a evaluated at regions of interest for (a) pH 7 (b) pH 5.5 (c) pH 4

Under steady-state conditions, the reactive current is constant. To achieve this the system adjusts the cathodic reaction rate via the proton surface concentration through an induced potential, as the reaction rate at the anode is fixed by the concentration of hydrogen peroxide [7].
The induced potential at different reaction regimes under different bulk pHs for the case of $Da_a/Da_c = 1$ are presented in Fig. 5.9. The potential induced for bulk pH 4 is completely negative and it corresponds to the completely reversed flow that is generated for the reactive regimes under within this bulk pH. Due to the excess of protons that is available by the bulk pH, the induced potential for this case shifts more negative to enforce proton depletion via the

reduction reaction. For the case of the bulk pH 7, the induced potential for bulk pH 7 is mostly positive except at $\mathrm{Da}_a \leq 10$ where the oxidation reaction rate is completely lowered and and the space charge density at the electrode is dominated by anions. For the bulk pH 5.5, the induced potential flips from negative to positive at $\mathrm{Da}_a = 316$, which is associated with the transition from reversed to normal flow (see figure 5.8b).

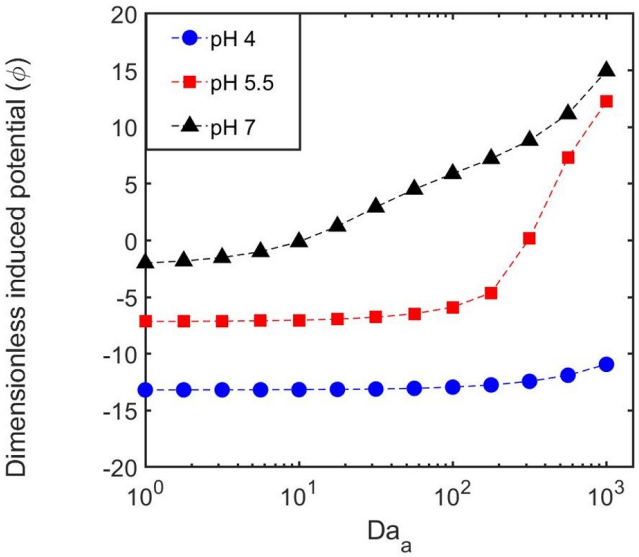

Figure 5.9: Effects of Da_a on the induced potential. The dotted dashed lines are for visualization purpose only

We observed some interesting features regarding the electric field due to the proton gradient dynamics. Typically, the electric field is induced by the current of protons that originates from the anode towards the cathode. There exists an apparent source of electric field lines where the electric field contributions from the proton flux and the surface charges are superposed [21, 11, 7]. The location of the apparent source of the field lines can be influenced by the dynamics of the proton gradient under reaction regimes. In Fig. 5.10 the electric field lines and flow field are presented for reaction regimes under bulk pH 5.5. For the case of $\mathrm{Da}_a = 3.1$ where flow is fully reversed, the apparent source of the field lines is situated above Au (Fig.5.10a). In Fig. 5.10b the flow field and electric field lines are presented for the transition Da_a reaction regime under bulk pH 5.5, where the flow is fully reversed at $\mathrm{Da}_a < 316$ and

the flow is driven from the anode to the cathode at $Da_a > 316$. The onset and transition to either of the two aforementioned flow forms is characterized by the generation of a pair of counter-rotating vortices. The apparent source of the electric field lines for this case is doubled and situated above both electrodes. In (Fig.5.10c) at $Da_a = 1000$, the apparent source of electric field lines is situated above Pt and points the cathode in accordance with the local flux of proton. For this case an electroosmotic flow is generated.

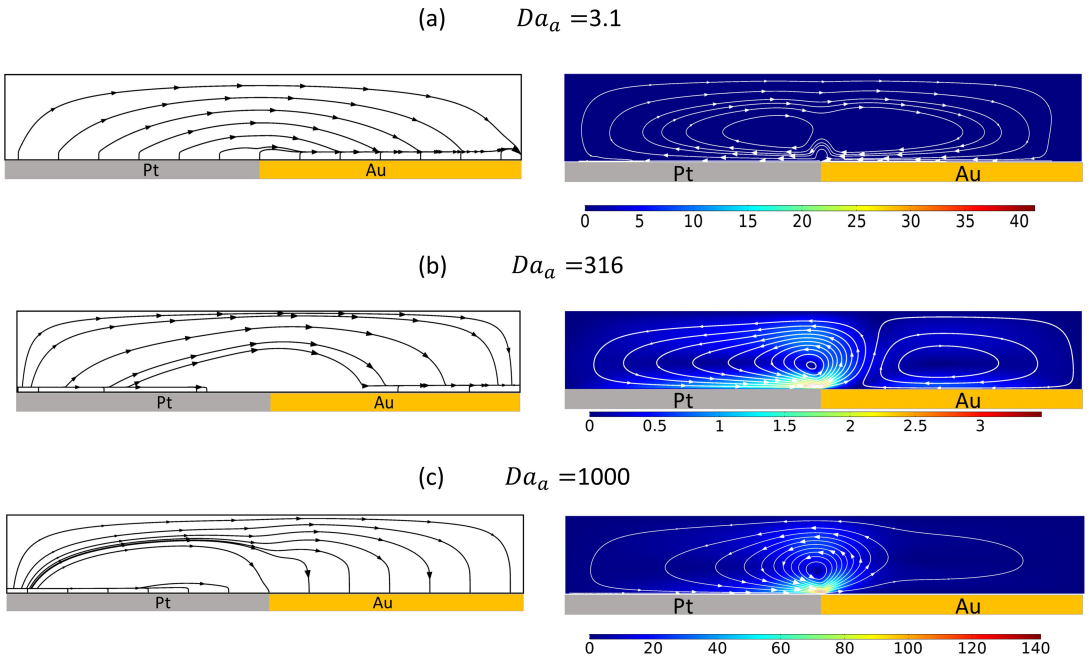

Figure 5.10: Dynamics of the electric and flow field under reaction regimes (a) $Da_a = 3.1$ (b) $Da_a = 316$ (c) $Da_a = 1000$

5.5 Conclusion

Electrocatalytic reaction-driven flow has been studied for different anodic reaction regimes (Da_a) via concentration and bulk pH variations, using experimental and numerical analysis that highlights its dependence on the proton concentration gradient. The fluid flow is visualized using particle tracking,

while the reaction-induced proton gradient is spatially mapped across the bi-electrode with fluorescence lifetime imaging microscopy. Our numerical simulations show that the reversed flow is primarily influenced by the dynamics of the proton concentration gradient that strongly impacts the electric field, in conjunction with charge density imbalances within the non-neutral zones. The transition reaction regime at which the flow is transformed from its reversed to a normal form was presented. It highlights the manner in which the electrocatalytic system enforces a steady state condition, through the interplay between diffusive and reaction timescales, and via the induced potential that adjusts the surface concentration of H^+ ions that affects the resulting advective flow and controls the overall electrocatalytic process. The proton gradient which is the basis for chemomechanical actuation was investigated using fluorescence lifetime imaging, which highlights an asymmetry of proton established across the electrodes during electrocatlytic reactions. The proton assymetry is impacted by the reaction regimes under bulk pH conditions, where flow reversal occurs at pH$\leq$4.5. These results are relevant and crucial towards the exploitation ERDF for potential applications such as micromixing.

S1 Electrochemical measurement

Electrochemical measurement was performed using an Autolab PGSTAT204 potentiostat, running NOVA 2.0 software, with a three-electrode cell comprising the platinum and gold interdigitated electrode with a micro Ag/AgCl reference electrode (eDAQ model ET073) in 2 mM H_2O_2. Either of Pt or Au electrode was subjected to potential sweeps with the oxidation and reduction range with a scan rate of 1 mV/s and the resulting current response is recorded.

The Tafel plot curve was obtained by plotting the current in log form versus the potential and is presented in Fig. S1. Based on the mixed potential theory, the gold electrode having the higher mixed potential acts as the cathode while platinum assumes the anodic role [31]. The intersection point between the mixed potentials of both electrodes yields the catalytic current (0.6 μA) and the bimetallic potential (169 mV).

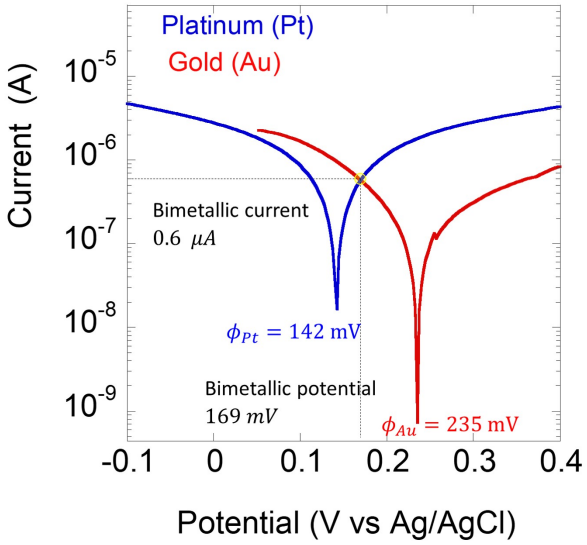

Figure S1: Tafel plots for Pt-Au interdigitated electrodes in 2 mM H_2O_2

S2 Electrophoretic force

The net force that drives the movement of the charge tracer particles comprises the drag and electrophoretic forces

$$\mathbf{F} = \mathbf{F}_d + \mathbf{F}_{ep} \tag{S1}$$

where the drag force $\mathbf{F}_d$ that acts on the particles of radius r that is transported within the solution is

$$\mathbf{F}_d = 6\pi r\eta\mathbf{u}. \tag{S2}$$

The electrophoretic force $\mathbf{F}_{ep}$ due to the electric field $\mathbf{E}$ and the electrophoretic velocity $\mathbf{u}_{ep} = \frac{\varepsilon}{\eta}\zeta_{p_+}\mathbf{E}$ is

$$\mathbf{F}_{ep} = 6\pi r\eta\mathbf{u}_{ep} \tag{S3}$$

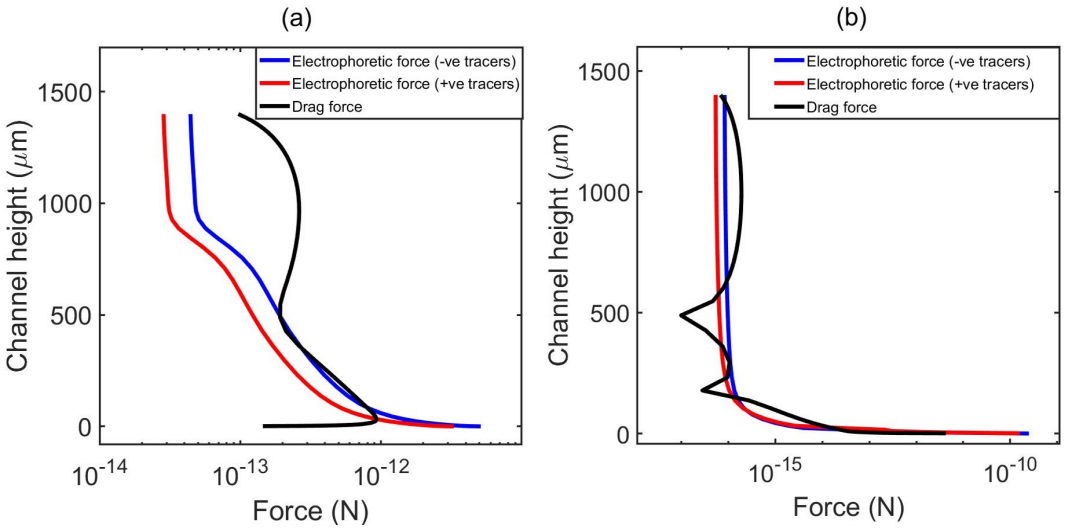

Figure S2: Variation of the forces acting on the tracer particles within hydrogen peroxide solution, 0.326 M, along the channel height, for (a) Bulk pH 5.8 (b) Bulk pH 4.2

References

[1] [n.d.]. see Supplemental Material for movies 1 and 2 at `https://figshare.com/s/13204d5064245d2c3aaf`.

[2] Afshar Farniya, A., Esplandiu, M. J. and Bachtold, A. [2014]. Sequential tasks performed by catalytic pumps for colloidal crystallization, *Langmuir* **30**(39): 11841–11845.

[3] Ashaju, A. A., Wood, J. A. and Lammertink, R. G. H. [2021]. Electrocatalytic reaction-driven flow, *Phys. Rev. Fluids* **6**: 044004.

[4] Benneker, Anne M., W. J. A. T. P. A. and Lammertink, R. G. H. [2016]. Observation and experimental investigation of confinement effects on ion transport and electrokinetic flows at the microscale, *Scientific Reports* **6**: 37236.

[5] Bowyer, W. J., Xie, J. and Engstrom, R. C. [1996]. Fluorescence

imaging of the heterogeneous reduction of oxygen, *Analytical Chemistry* **68**(13): 2005–2009.

[6] Datta, R., Heaster, T. M., Sharick, J. T., Gillette, A. A. and Skala, M. C. [2020]. Fluorescence lifetime imaging microscopy: fundamentals and advances in instrumentation, analysis, and applications, *Journal of Biomedical Optics* **25**(7): 1 – 43.

[7] Davidson, S. M., Lammertink, R. G. and Mani, A. [2018]. Predictive model for convective flows induced by surface reactivity contrast, *Physical Review Fluids* **3**(5): 1–16.

[8] de Valença, J., Jõgi, M., Wagterveld, R. M., Karatay, E., Wood, J. A. and Lammertink, R. G. H. [2018]. Confined electroconvective vortices at structured ion exchange membranes, *Langmuir* **34**(7): 2455–2463.

[9] Doneux, T., Bouffier, L., Goudeau, B. and Arbault, S. [2016]. Coupling electrochemistry with fluorescence confocal microscopy to investigate electrochemical reactivity: A case study with the resazurin-resorufin fluorogenic couple, *Analytical Chemistry* **88**(12): 6292–6300.

[10] Engstrom, R. C., Ghaffari, S. and Qu, H. [1992]. Fluorescence imaging of electrode-solution interfacial processes, *Analytical Chemistry* **64**(21): 2525–2529.

[11] Esplandiu, M. J., Afshar Farniya, A. and Reguera, D. [2016]. Key parameters controlling the performance of catalytic motors, *Journal of Chemical Physics* **144**(12).

[12] Farniya, A. A., Esplandiu, M. J., Reguera, D. and Bachtold, A. [2013]. Imaging the proton concentration and mapping the spatial distribution of the electric field of catalytic micropumps, *Physical Review Letters* **111**(16).

[13] Fish, K. N. [2009]. Total internal reflection fluorescence (tirf) microscopy, *Current Protocols in Cytometry* **50**(1).

[14] Ibele, M. E., Wang, Y., Kline, T. R., Mallouk, T. E. and Sen, A. [2007]. Hydrazine fuels for bimetallic catalytic microfluidic pumping, *Journal of the American Chemical Society* **129**(25): 7762–7763.

[15] Johnson, I. [2010]. *Molecular Probes Handbook: A Guide to Fluorescent Probes and Labeling Technologies*, Life Technologies Corporation.

[16] Jun, I.-K. and Hess, H. [n.d.]. A biomimetic, self-pumping membrane, *Advanced Materials* **22**(43): 4823–4825.

[17] Kline, T. R., Paxton, W. F., Wang, Y., Velegol, D., Mallouk, T. E. and Sen, A. [2005]. Catalytic micropumps: microscopic convective fluid flow and pattern formation, *Journal of the American Chemical Society* **127**(49): 17150–17151.

[18] Lakowicz, J. R. (ed.) [2006]. *Principles of Fluorescence Spectroscopy*, Springer US.

[19] Leenheer, A. J. and Atwater, H. A. [2012]. Imaging water-splitting electrocatalysts with pH-sensing confocal fluorescence microscopy, *Journal of The Electrochemical Society* **159**(9): H752–H757.

[20] Lin, H.-J., Herman, P., Kang, J. S. and Lakowicz, J. R. [2001]. Fluorescence lifetime characterization of novel low-ph probes, *Analytical Biochemistry* **294**(2): 118 – 125.

[21] Moran, J. L. and Posner, J. D. [2011]. Electrokinetic locomotion due to reaction-induced charge auto-electrophoresis, *Journal of Fluid Mechanics* **680**: 31–66.

[22] Naeem, S., Naeem, F., Liu, J., Quiñones, V. A. B., Zhang, J., He, L., Huang, G., Solovev, A. A. and Mei, Y. [2019]. Oxygen microbubble generator enabled by tunable catalytic microtubes, *Chemistry An Asian Journal* **14**(14): 2431–2434.

[23] Pantaloni, D., Clainche, C. L. and Carlier, M.-F. [2001]. Mechanism of actin-based motility, *Science* **292**(5521): 1502–1506.

[24] Paxton, W. F., Baker, P. T., Kline, T. R., Wang, Y., Mallouk, T. E. and Sen, A. [2006]. Catalytically induced electrokinetics for motors and micropumps, *Journal of the American Chemical Society* **128**(46): 14881–14888.

[25] Paxton, W. F., Kistler, K. C., Olmeda, C. C., Sen, A., St. Angelo, S. K., Cao, Y., Mallouk, T. E., Lammert, P. E. and Crespi, V. H. [2004]. Catalytic nanomotors: Autonomous movement of striped nanorods, *Journal of the American Chemical Society* **126**(41): 13424–13431.

[26] Punckt, C., Jan, L., Jiang, P., Frewen, T. A., Saville, D. A., Kevrekidis, I. G. and Aksay, I. A. [2012]. Autonomous colloidal crystallization in a galvanic microreactor, *Journal of Applied Physics* **112**(7): 074905.

[27] Soong, R. K., Bachand, G. D., Neves, H. P., Olkhovets, A. G., Craighead, H. G. and Montemagno, C. D. [2000]. Powering an inorganic nanodevice with a biomolecular motor, *Science* **290**(5496): 1555–1558.

[28] Subramanian, S. and Catchmark, J. M. [2007]. Control of catalytically generated electroosmotic fluid flow through surface zeta potential engineering, *The Journal of Physical Chemistry C* **111**(32): 11959–11964.

[29] Thielicke, W. and Stamhuis, E. J. [2014]. PIVlab – towards user-friendly, affordable and accurate digital particle image velocimetry in MATLAB, *Journal of Open Research Software* **2**.

[30] Wang, W., Duan, W., Zhang, Z., Sun, M., Sen, A. and Mallouk, T. E. [2015]. A tale of two forces: Simultaneous chemical and acoustic propulsion of bimetallic micromotors, *Chemical Communications* **51**(6): 1020–1023.

[31] Wang, Y., Hernandez, R. M., Bartlett, D. J., Bingham, J. M., Kline, T. R., Sen, A. and Mallouk, T. E. [2006]. Bipolar electrochemical mechanism for the propulsion of catalytic nanomotors in hydrogen peroxide solutions, *Langmuir* **22**(25): 10451–10456.

[32] Weibel, D. B., Garstecki, P., Ryan, D., DiLuzio, W. R., Mayer, M., Seto, J. E. and Whitesides, G. M. [2005]. Microoxen: Microorganisms to move microscale loads, *Proceedings of the National Academy of Sciences* **102**(34): 11963–11967.

[33] Wong, F. and Sen, A. [2016]. Progress toward light-harvesting self-electrophoretic motors: Highly efficient bimetallic nanomotors and micropumps in halogen media, *ACS Nano* **10**(7): 7172–7179.

Chapter 6

Electrocatalytic Reaction Induced colloidal aggregation

Abstract

A surface driven flow is generated during electrocatalytic reaction by a platinum-gold bielectrode within hydrogen peroxide. This flow can be experimentally visualized and quantified using micron-sized particles that are transported by the flow field. The tracer particles, which possess an inherent surface charge, also interact with the induced electric field and exhibit a collective behavior at the surface of the electrodes where they aggregate. The underlying mechanism for the aggregation dynamics demonstrated by these catalytic pump systems has so far been lacking. In this work, the aggregation dynamics and kinetics were experimentally investigated. Using numerical simulations, we demonstrate that the self-driven particle aggregation is controlled by a positive dielectrophoretic force, mediated by the reaction-induced electric and flow field. These results contribute to the fundamental knowledge on immobilized bimetallic systems.

6.1 Introduction

Electrocatalytic micromotors exhibit locomotion within an aqueous medium. They are powered by the conversion of chemical energy that is sourced from their local environment. This has been demonstrated by the autonomous motion of Pt-Au catalytic nanorods within an aqueous solution containing hydrogen peroxide (see Fig. 6.1a). The Pt-Au bielectrode catalyzes the decomposition of hydrogen peroxide via surface reactions, leading to the establishment of concentration and electrical potential gradients that propel the nanorods. If the motility of the nanorod is restricted by immobilizing it on a substrate and the electrochemical reaction is allowed to proceed, based on Galilean invariance, an interfacial fluid flow will be generated within the immediate surroundings of the immobilized nanorod, which is also referred to as an electrocatalytic micropump (see Fig. 6.1b).

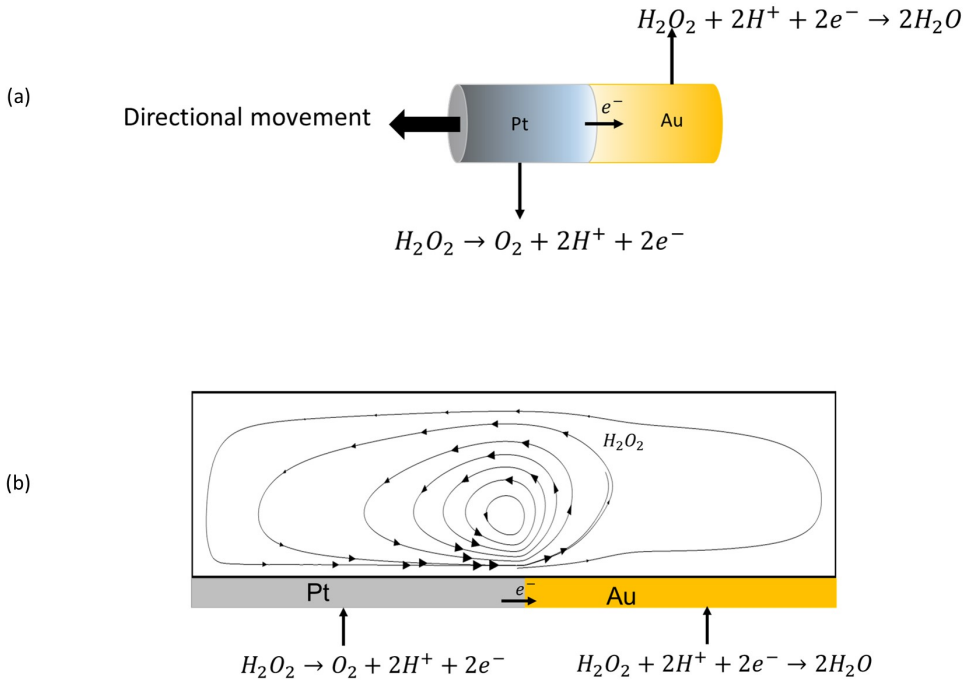

Figure 6.1: Schematic diagram of (a) Pt-Au bimetallic nanorod (b) A Pt-Au bimetallic micropump that generates an interfacial flow driven by electrochemical reaction.

The fluid flow is driven by an electric body force generated by an induced electric field acting on a net charge distribution, which both arise from a proton concentration gradient that is established during the electrochemical reaction involving the decomposition of hydrogen peroxide. The reaction proceeds via oxidation and reduction pathways where oxidation occurs at the anode (platinum) leading to the generation of protons and oxygen, and reduction occurs at the cathode (gold) involving the consumption of protons and production of water as a by-product.

The induced fluid flow is typically visualized using tracer particles. However, these particles, which possess their inherent surface charge and zeta potential, are affected by the electric field through an electrophoretic force that results in particle migrations. Moreover, the particles begin to aggregate and form assemblies at the surface of the electrodes.

The combined electrohydrodynamic mechanism, especially the aggregation and patterning of the particles close to the electrode surface, has been observed for electrocatalytic micromotors and micropumps. Wang and his team [34, 16] reported on the attachment of particles on bimetallic (Au-Pt) and trisegmented nanorods (Au-Ru-Au). The collective dynamics between these two classes of objects was attributed to an electrostatic force that is generated by the electric field [35]. As soon as a moving nanorod approaches the charged particles, the particles are attracted towards the rod leading to aggregation and formation of raft assemblies on the nanorod. Their modeling approach considered the nanorod as being uncharged, while the shear plane potential was made to float.

The dynamic interactions between the an immobilized bimetallic system and colloidal particles occur irrespective of the combination of metals (Au-Pt, Au-Pd, Au-Ag, and Au-Cu) and fuel (H_2O_2, N_2H_4 and HCl) used in powering the system [20, 14, 9, 27, 15]. In most cases, particles are observed to aggregate and concentrate at the junction of the connected electrodes. The consensus for this behaviour is that the particle attachment and aggregation are primarily driven by an electrohydrodynamic force. The induced flow transports the particles towards the surface of the electrodes where they become trapped and aggregate under the influence of the self-generated electric field.

The directed transport of colloidal particles has been demonstrated for applications involving cargo transport [33] and biological assays [4], biosensors [32] and optics [10]. In the aforementioned applications, the collective transport and aggregation kinetics of the particles are controlled by an externally applied field. In the case of the immobilized electrocatalytic systems where the

particle collective dynamics is self-driven, it is crucial to fully understand the underlying mechanism to fully exploit this behavior for relevant applications. In this study, we present quantitative analyses that pertain to the aggregation dynamics of particles at bimetallic electrocatalytic junctions for different timescales and electrolyte concentrations. We present a set of governing equations, that describes the physics underlying the aggregation mechanism of particles at the surface of an immobilized bimetallic system by a DC-dielectrophoretic (DEP) force. The results elucidate the reaction-induced colloidal aggregation mechanism and highlights the role of the dielectrophoretic force.

6.2 Theory and numerical modelling

Dielectrophoresis is an electrokinetic phenomenon exploited for several lab-on-chip applications that ranges from sorting, separation, manipulation and concentration of microparticles, as well as cells and viruses [2, 18, 19, 28]. When a dielectric particle is exposed to a nonuniform electric field, it becomes polarized and as a result, the surface charges are reoriented inducing a dipole [26]. The interaction between a dipole and an electric field gradient creates a dielectrophoretic force, $\mathbf{F}_{DEP}$ [5]. For the immobilized electrocatalytic system the $\mathbf{F}_{DEP}$ force is strongly dependent on the reaction-induced electric field which can be indirectly influenced by geometry of the electrodes. To understand and predict the interaction between the dielectrophoretic force and the tracer particles, we developed 2D models including Pt-Au bielectrodes. The bimetallic and interdigitated electrodes are immersed into a solution of hydrogen peroxide and tracer particles and confined within a chamber of depth h. Figure 6.2 presents a schematic diagram of an immobilized Pt-Au bielectrode that catalyzes the decomposition of hydrogen peroxide via redox reactions. Oxidation occurs at the Pt end that generates protons, oxygen molecules and electrons. The electrons are directly transferred to Au to complete the circuitry. During the reduction reaction at the Au electrode, protons are consumed and combined with hydrogen peroxide to create water. The flux of protons between the electrodes establishes a proton concentration gradient that generates an electric field $\mathbf{E}$, and combines with the net charge distribution to form a body force that drives the interfacial fluid flow. The flow, which was visualized with tracer particles, is driven from platinum towards gold under normal electrocatalytic steady state conditions and recirculates within a closed system.

The charged particles that are close to the surface of the bielectrode are

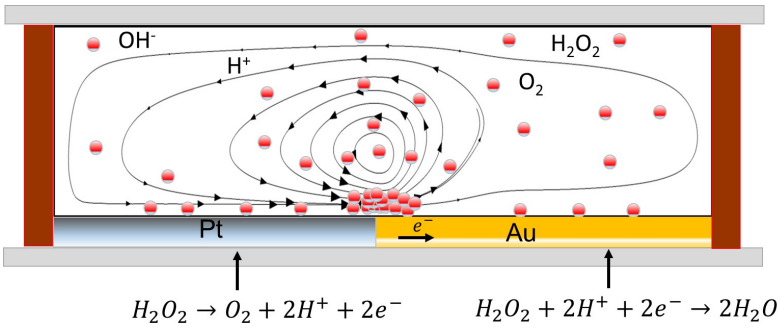

Figure 6.2: Schematic diagram of Pt-Au microreactor, that drives the movement and aggregation of colloidal particles during electrocatalytic reaction.

trapped and aggregated at the junction of the bielectrode. The dielectrophoretic force acting on the particle is expressed as [18]

$$\mathbf{F}_{DEP} = -2\pi\varepsilon r^3 k_{cm}(\mathbf{E}\cdot\nabla\mathbf{E}) \tag{6.1}$$

where ε is the fluid's permittivity, r is the radius of a particle and k_{cm} is Clausius-Mossotti (CM) factor that is defined in terms of the conductivity for the particle σ_p and the fluid medium σ_f as

$$k_{cm} = \frac{\sigma_p - \sigma_f}{\sigma_p + \sigma_f} \tag{6.2}$$

If $\sigma_p > \sigma_f$, the dielectric particle will be attracted towards the region of high electric field strength (positive dielectrophoresis) and if $\sigma_p < \sigma_f$ the particles are drawn to a weak electric field region (negative dielectrophoresis). According to O'Konski [24], the conductivity of a particle is defined as

$$\sigma_p = \sigma_b + 2\frac{K_s}{r} \tag{6.3}$$

where K_s denotes the surface conductance which is about 1 nS for latex particles [13], σ_b represents the bulk conductivity of polystyrene, which has been proven to be $\sigma_b \approx 0$ [8, 24]. The surface conductance with particle radius $r = 0.5\ \mu m$ results in an effective particle conductance of 40 μS/cm. The conductivity of the fluid medium was in the measured in the range of 5-30 μS/cm, leading to positive dielectrophoresis.

6.2.1 Governing equations

Here we present the governing equations that resolve the ionic species concentration field with the induced potential and electric field, the resulting flow field, and trajectories of the colloidal particles.
Under the assumption of a dilute solution limit, the concentration of ionic species (H^+, OH^-, Cl^-) are solved by the Nernst-Planck equation,

$$\mathbf{u} \cdot \nabla c_i = \nabla \cdot (D_i \nabla c_i + z_i F \mu_i \nabla \phi c_i) \tag{6.4}$$

where $\mathbf{u}$ represents the fluid velocity, c_i is the molar concentration for i^{th} species, having a diffusion constant D_i with valence z_i, and ϕ is the electrostatic potential. The potential distribution in conjunction with the space charge density ρ_e is described by the Poisson equation,

$$\nabla^2 \phi = \rho_e / \varepsilon \tag{6.5}$$

where, $\rho_e = \sum_{i=1}^{N} F z_i c_i$. The gradient of the induced potential gives rise to the electric field described as, $\mathbf{E} = -\nabla \phi$.
The Stokes and continuity equations describe the fluid flow for an incompressible Newtonian fluid operating under a lower Reynolds regime ($Re \ll 1$),

$$0 = -\nabla p + \eta \nabla^2 \mathbf{u} + \rho_e \nabla \phi \tag{6.6}$$

$$\nabla \cdot \mathbf{u} = 0 \tag{6.7}$$

The movement of the particles is described by Newton's law of motion,

$$\frac{d(m_p)\mathbf{u}}{dt} = \mathbf{F}_d + \mathbf{F}_{ep} + \mathbf{F}_{DEP} \tag{6.8}$$

where m_p is the mass of the particle and $\mathbf{F}_d$ is the drag force that acts on the particles of radius r moving with velocity $\mathbf{u}$ through peroxide solution with viscosity η [6], given as

$$\mathbf{F}_d = \frac{1}{\tau_p} m_p M (\mathbf{u} - \mathbf{v}) \tag{6.9}$$

τ_p is the response time of the particle velocity in seconds, $\mathbf{v}$ is the velocity of the particles (m/s). M is a correction for the wall effects given as

$$M = \left(1 + \frac{1}{1 - \frac{9}{16}\alpha + \frac{1}{8}\alpha^3 - \frac{45}{256}\alpha^4 - \frac{1}{16}\alpha^5}\right)(I - P(\mathbf{n})) + \frac{1}{1 - \frac{9}{8}\alpha + \frac{1}{2}\alpha^3} P(\mathbf{n}) \tag{6.10}$$

where I denotes the identity matrix, $P(\mathbf{n})$ defines the projection operator onto the wall normal, $\mathbf{n}$, $\alpha = \frac{r}{l_w}$, and l_w is the distance from the center of the particle to the nearest wall [12].
The electrophoretic force $\mathbf{F}_{ep}$ is defined as

$$\mathbf{F}_{ep} = 6\pi r\eta \mathbf{u}_{ep}, \tag{6.11}$$

where $\mathbf{u}_{ep}$ is the electrophoretic velocity of the particles [17].
The drag, electrophoretic and dielectrophoretic force exert a net resultant force on the particles resulting in its acceleration. The particles in this case are assumed to be spherical in shape. Gravitational force is neglected since the particles are assumed to be neutrally buoyant.

6.2.2 Boundary conditions

A no-slip condition, $\mathbf{u} = 0$ is applied to the top and bottom boundaries. The trajectories of the particle on the surface of the particle was set to stick condition to represent the particle trapping and aggregation. A symmetry boundary condition is applied on the left and right walls of the bimetallic system model. For the interdigitated electrode we imposed a periodic boundary condition on the left and right walls to indicate a repeated pattern for Pt and Au for which we simulate a single period. For the potential boundary conditions, we solved explicitly the diffuse part of the electric double layer. The potential drop across the Stern layer is described by

$$\Delta\phi_{Stn} = \zeta - \phi_{electrode} \tag{6.12}$$

which scales with the ratio between the Stern layer length L_{Stn} and the Debye length L_D as well as the zeta potential of the electrode $\zeta_{electrode}$ as

$$\Delta\phi_{Stn} \approx \frac{L_{Stn}}{l_D}\zeta \tag{6.13}$$

where $L_D = \sqrt{\varepsilon V_T/2Fc_\infty}$ is usually hundreds of nanometer and c_∞ is the bulk proton concentration. For an electrolyte having a low salt concentration, $\frac{L_{Stn}}{L_D} \ll 1$, and as a result $\Delta\phi_{Stn}$ in equation 6.12 becomes negligible. Equation 6.12 is applied at the surface of Pt and Au ($y = 0$) in terms of their respective zeta potentials as $\phi_{Pt} = \zeta_{Pt}$, and $\phi_{Au} = \zeta_{Au}$. The upper boundary of the model is set as $\frac{\partial\phi}{\partial y} = 0$.

The reactive current that runs through the electrodes has been experimentally measured [3], and is described by the Frumkin-Butler-Volmer equation

$$j = k_a c_{\mathrm{H_2O_2}} \exp(\frac{(1-\alpha)nF\Delta\phi_{Stn}}{RT}) - k_c c_{\mathrm{H_2O_2}} c_{\mathrm{H^+}}^2 \exp(\frac{-\alpha nF\Delta\phi_{Stn}}{RT}) \quad (6.14)$$

from which the reaction kinetics and proton flux are determined. The proton reaction flux is expressed from the measured current density, $j = i/nFAz$, where A is the surface area of the bielectrode, n is the number of electrons transferred during the reaction, and k_a and k_c are the anodic and cathodic rate constant respectively. By considering the forward direction of the irreversible redox reaction, the proton reaction flux for the anodic reaction is expressed as

$$j_{pt} = k_a c_{\mathrm{H_2O_2}} \quad (6.15)$$

and the cathodic reaction is given as

$$j_{Au} = k_c c_{\mathrm{H_2O_2}} c_{\mathrm{H^+}}^2 \quad (6.16)$$

The flux of anions ($\mathrm{OH^-}$, $\mathrm{Cl^-}$) at the surface of the electrodes ($y = 0$) are set to zero since they do not participate in the electrochemical reaction.

6.2.3 Numerical method and simulation

The 2D models were partitioned into subdomains to implement a user-controlled nonuniform mesh that consists of triangular elements. A uniform mesh was imposed at the tangential x-direction within the lower part of the model, using mapped meshing control. This results into refinements that resolve the electric double layer and other gradients at the surface of the electrodes.
The governing equations are solved using COMSOL Multiphysics 5.5, a finite element based commercial solver. At the beginning of the simulation, the steady Nernst-Planck and Poisson equations are computed without the flow field to generate initial conditions for the system, which were used in solving the coupled governing equations sequentially until the solution converges. The results are implemented as initial values for a time-dependent solver used in resolving the particle trajectories, where time-stepping is performed using a generalized alpha implicit method.

6.3 Experimental method

The colloidal aggregation experiments were performed using platinum-gold bielectrodes that are immobilized on glass substrates. The bielectrodes were

fabricated as follows: positive resist was spin-coated on a glass wafer, followed by exposure to UV-light through a photomask and development. Both platinum and gold electrodes were sputtered on Tantalum (5 nm) which was predeposited on the glass wafer (MESA+ nanolab clearoom in-house equipment,"TCOathy"). Undesired metal residues were removed during lift-off process by ultrasonification in acetone. Both Pt-Au interdigitated (IDE) electrodes and Pt-Au bimetallic electrodes were fabricated by this method (see figure 6.3).

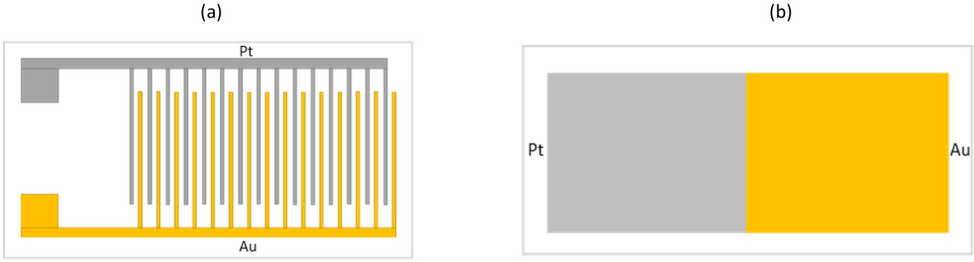

Figure 6.3: Schematic diagram of Pt-Au microreactor, that drives the movement and aggregation of colloidal particles during electrocatalytic reaction. (a) Pt-Au Interdigitated electrode. (b) Pt-Au bimetallic electrode

The interdigitated electrodes were bonded to a printed circuit board. This configuration allows us to control the electrochemical reaction. For the bimetallic electrodes, Pt and Au form a galvanic pair that maintains a continuous contact between each electrode. Hydrogen peroxide (Sigma Aldrich) solutions of known concentrations were prepared in MilliQ water ($\rho > 18$ MΩ.cm). The pH of the resulting solutions were adjusted accordingly using HCl in the range pH 5 to 6, and the conductivity was measured with a conductivity probe (WTW Cond 3110, Weilheim, Germany) to be in the range of 5 to 30 μS/cm. Particle dispersions were prepared by seeding the hydrogen peroxide (10 ml) solution with 2.5 wt% (1 μl) fluorescent microparticles (PS-FluoRed-Fi329 by Microparticles GmbH), 1 μm in diameter, and introduced into a confined hybrid chamber that contains the Pt-Au bimetallic electrode. The motion and aggregation of the particles are observed with an inverted optical microscope (Carl Zeiss Axio Observer Z1, 20x). Image frames were recorded with a CCD camera with a frame rate of 10 fps. Image analysis was done using open access

software, ImageJ [30]. The image frames were digitized by converting to 8 bits. The contrast and brightness were adjusted and the image background was subtracted to isolate the particles. A standard maximum entropy threshold was applied to identify the particles. The total number of aggregated particles are counted and the aggregated size is analyzed.

6.4 Results and discussion

6.4.1 Experimental results

The movement and collective dynamics of the particles are observed with the microscope. The tracer particles are transported near the surface of the electrodes (at a relative height $\approx$ y=10 μm) by the induced fluid flow from the anode (platinum) to the cathode (gold) (see supplementary movie1 [1]). The particles close to the junction of the connected electrodes become trapped, and the population grows in clusters. Figure 6.4 shows the time series for the particle aggregation at the junction of a Pt-Au bimetallic electrode. With time, the aggregates builds up and slightly extends above the surface of the bielectrode.

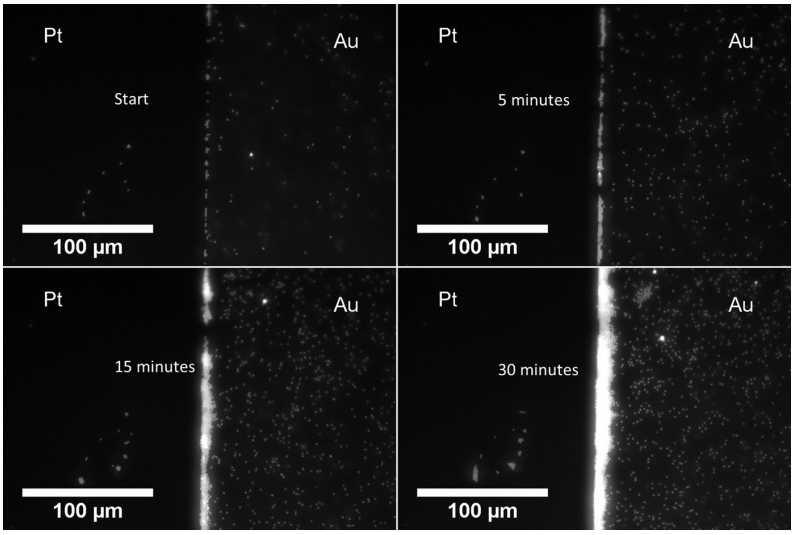

Figure 6.4: Time series colloidal aggregation at the junction of Pt-Au bimetallic electrode.

To confirm the dependence of the particle trapping and aggregation on the

electrocatalytic reaction, the experiment was repeated using interdigitated electrodes, where the reaction is monitored and controlled by an external current measurement. During the connected mode, the particles close to the surface of the electrodes are migrating towards the platinum electrode where they maintain their Brownian motion (figure 6.5a). At longer timescales, the particles are observed to aggregate and grow into clusters (see Supplementary movie 4 [1]). As soon as the electrodes are disconnected, the particles are released from the aggregated structure and slowly disperse again into the bulk region (figure 6.5b, supplementary movie 5 [1]). To understand what is happening, we refer back to the electrochemical behaviour of the Pt-Au interdigited electrodes in hydrogen peroxide solution (see 4.4.1). During the connected mode, a bimetallic potential is induced following the balanced reactive fluxes on the electrodes. The thus generated electric field plays two main roles. First, it drives the fluid flow in conjunction with the space charge density in an electroosmotic fashion. Secondly, it interacts with the particles to create (dielectro)phoretic forces that affect the movement of the particles.

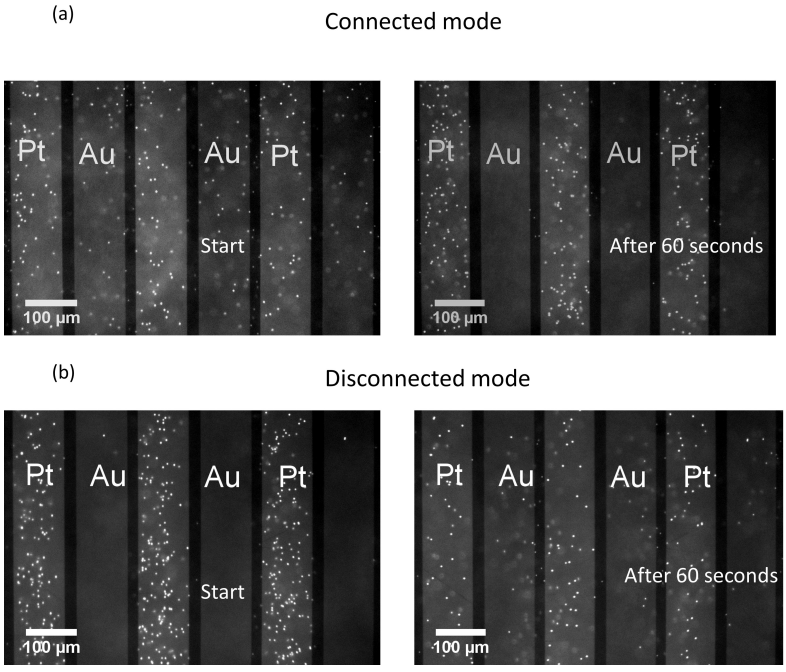

Figure 6.5: (a) Colloidal trapping at the platinum electrode during the connection mode (b) Release of the particles during the disconnected mode

Now that we know that the particle aggregation dynamics is controlled by the reaction-induced electric field, we quantify the aggregation dynamics by estimating the surface coverage (the total area of the aggregated particles vs. the total surface area of the electrode) from the aggregated particles monolayer formed during the first minutes of the aggregation process. The surface coverage is plotted as a function of time for different H_2O_2 concentrations (0.05 M, 0.108 M and 0.163 M) and shown in figure 6.6a. The clear trend depicts the increase in aggregation rate with increase in H_2O_2 concentration. To elucidate

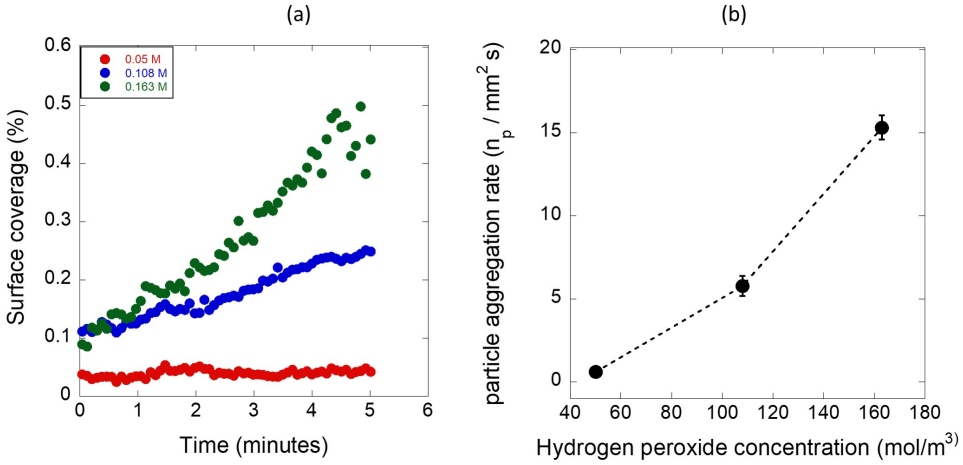

Figure 6.6: Effects of H_2O_2 concentration on (a) percentage surface coverage by the particles (b) aggregation rate constant. Data points for the rate constant are averaged from three experiments. Dashed line serves as guide to the eyes.

the influence of H_2O_2 on the aggregation kinetics, we determined the aggregation rate constant from the number of aggregated particles n_p that is fitted with a linear regression, which yielded the slope that corresponds to the aggregation rate. This was evaluated during the first five minutes of the aggregation process before the particles form multilayers. Figure 6.6b suggests that the aggregation rate increased rapidly at higher peroxide concentrations owing to the increase in field strength due to the impact of the peroxide concentration on the electrochemical reaction rate.

6.4.2 Particle aggregation by DC dielectrophoresis

Our numerical simulations provide more insights on the particle aggregation behaviour at the surface of the electrodes. We start by analyzing the reaction-induced electric field that drives the particle aggregation. Figure 6.7 shows the electric field lines across the Pt-Au bimetallic and interdigitated electrodes, combined with the induced potential (color). In both cases, the electric field as well as the induced potential is generated by the proton gradient that originates from the electrochemical reaction involving the decomposition of H_2O_2. The induced potential acts to balance the reactive current from the electrodes through the variation of the proton concentration at the electrode's surface [7]. We see in figure 6.7 that the electric field originates from platinum

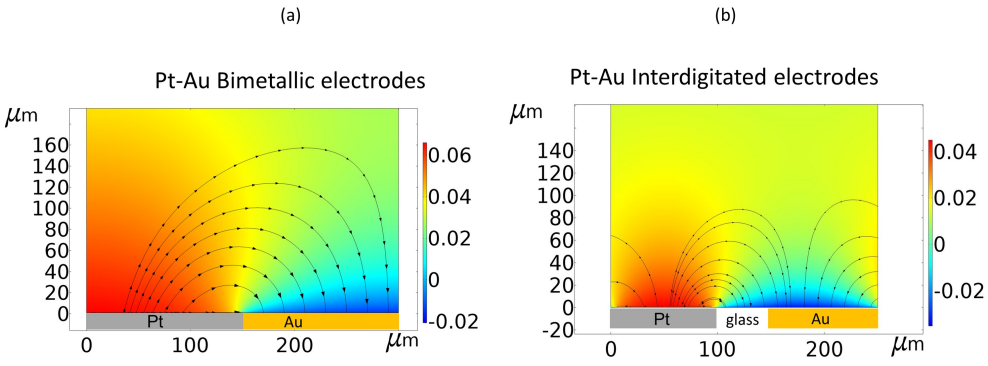

Figure 6.7: Electrocatalytically induced electric potential (in volts and colorscale), overlaid with the electric field streamlines for (a)Pt-Au bimetallic electrodes (b)Pt-Au interdigitated electrodes

and the field line extends towards gold. The apparent source of the electric field, which is rooted at platinum is the region where the field contributions from the reaction-induced proton gradient and surface charges intersects [23]. The direction of the field lines is dictated by the proton current across the bielectrode as well as the gradient of the induced potential.
Figure 6.8a shows the tangential electric field profile along the length of the bimetallic electrode whose gradient is maximum at the junction where both electrodes maintain a continuous contact. The physical inhomogeneity at the midpoint increases the electric field strength that creates the DEP force. The electric field combined with the charge density drives the fluid flow that transports the particles near the surface of the electrode during recirculation (figure

6.8b), within the range of the positive dielectrophoretic force, where they become trapped and aggregate into clusters. The charged particles are capable of generating electroosmotic flow due to interactions between the induced electric field and the double layer of the surface of the particles [31, 11], which act to entrain nearby particles on the electrode. But they were not computed in the model as they are hardly visible in this case (see video 1 and 2 [1]).
Different strategies have been previously adopted to increase the local field to concentrate particles within the high field region. A common method is to use insulating structures that generate spatial non-uniformity in the local electric field known as insulator based dielectrophoresis (iDEP), which increases the intensity of the field that strongly affects the particles [25, 22, 18]. In another instance, a scratch was introduced on the surface of an ITO electrode, which increased the local current density by a factor of two compared to unscratched electrodes, and promotes an higher field strength that traps colloidal particles within the scratched region [29]. In the case of the interdigitated electrode,

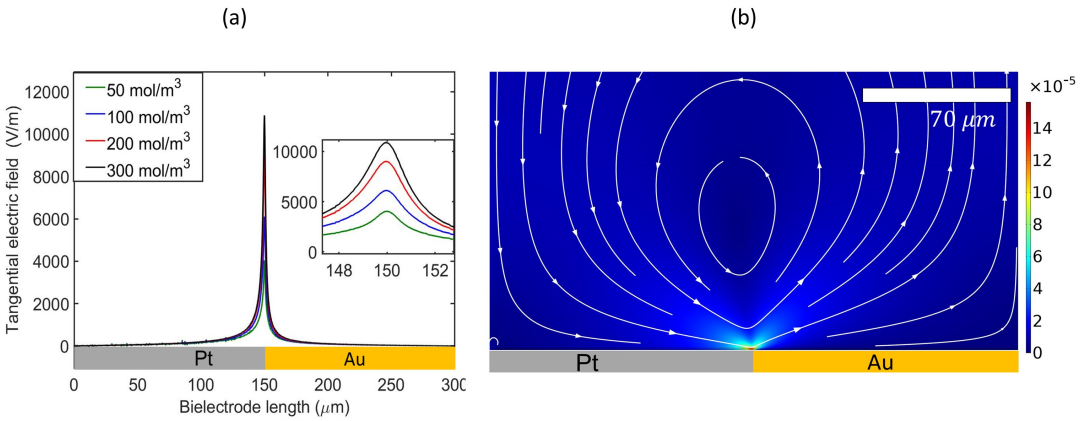

Figure 6.8: (a) Tangential electric field along the Pt-Au bimetallic electrode surface (b) Fluid flow pattern driven by the electric field gradient near the platinum-gold junction. The velocity magnitude is given in m/s

the tangential electric field is maximum at the end of the platinum electrode just before the spacing between Pt and Au, and the resulting flow streamlines that is driven by the field gradient buildup from this region, which transport particles close to the platinum end of the interdigitated electrode where they eventually aggregate (see Figure S2).

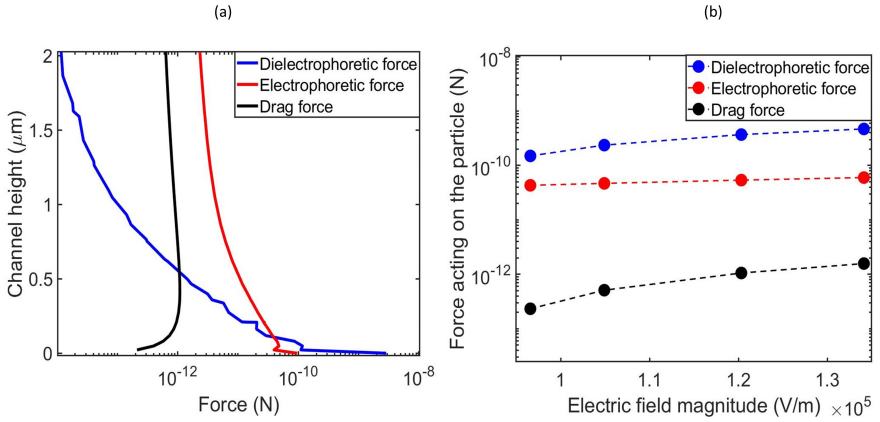

Figure 6.9: (a) Magnitude of the different forces acting on the particles. The magnitude of the forces are averaged at every height of the channel height from the junction of the bielectrode (b) The maximum of the forces acting on the particles as a function of the induced electric field magnitude along the channel height from the junction of the electrodes.

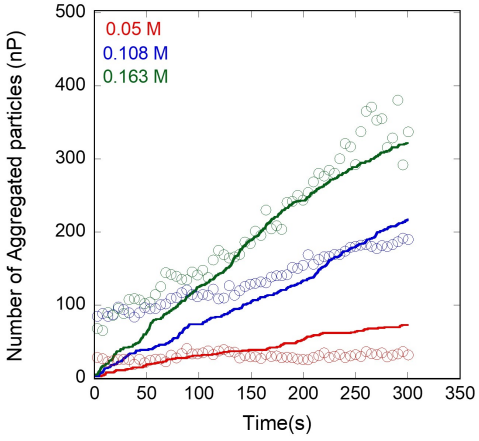

Figure 6.10: Comparison of the experimentally determined number of particles (open symbols) with simulation results (solid lines) for different H_2O_2 concentrations.

Figure 6.9a shows the average distribution of forces acting on the particles that are plotted from the bielectrode junction along the channel height. At

several microns from the surface region, ($y > 1\mu m$), the electrophoretic and drag forces dominate the DEP force. At y $\leq$ 1 μm, the DEP force is amplified by the high electric field strength and gradient and becomes more significant. At the surface region, the DEP force surpasses the other two forces by almost three orders of magnitude. As a result, the particles that are transported by the flow field are impacted by both the drag force and the electrophoretic force, and as soon as they are within range of the positive DEP force, they are pulled towards the region of the maximum local electric gradient where they aggregate.

The maximum of each force contribution was determined for different electrolyte conditions and plotted versus the induced electric field (figure 6.9b). All forces were greater than the Brownian force acting on the particle, which was determined to be in the order of magnitude 10^{-15}N (see supplementary section S3). We see that the positive DEP force exerts the most dominant force on the particles, which occurs at the bielectrode junction.

The number of particles that are aggregated at the junction of the Pt-Au bimetallic electrodes are determined numerically and compared with our experimental results for different H_2O_2 concentrations (see figure 6.10). The model is able to capture the aggregation dynamics, while predicting the number of aggregated particles in the same order of magnitude.

6.5 Conclusion

In this chapter, we studied the dynamics of the reaction-driven colloidal trapping and aggregation by a Pt-Au bimetallic catalytic system. We showed that the aggregation of the particles occurs under the influence of a positive dielectrophoretic force that is mediated by a self-induced electric field. The particle aggregation kinetics were studied experimentally and found to scale with the concentration of the fuel that drives the electrocatalytic reaction which generates the induced electric field. Numerical modelling elucidates the role of the drag and electrophoretic force that directly influences the movement of the particles further away from the surface region, while they aggregate under the effect of a positive dielectrophoretic force at the surface. Our combined experimental and numerical approaches shed light on the underlying mechanism of the reaction-induced particle aggregation and advance the knowledge on the transport mechanism by immobilized electrocatalytic systems.

S1 Quantification of particle aggregation

The percentage surface coverage is defined as

$$\frac{A_p}{A_s} \times 100 \tag{S1.1}$$

where $A_s = L \times W$ is the surface area of the bielectrode (figure S1), L is the length of the bielectrode ($L = 300\mu m$), and W is the width ($W = 200\mu m$). A_p denotes the total area of the aggregated particles, $A = \Sigma\pi r^2$, where r is the radius of a particle. The number of aggregated particles (np) is defined as

$$n_p = \frac{A_p}{\pi r^2}. \tag{S1.2}$$

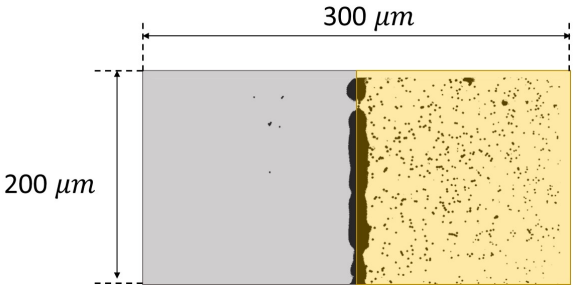

Figure S1: Schematic that describes the surface area of the bimetallic electrode

S2 Simulation details for the interdigitated electrodes

The following are the simulation results that are computed for the interdigitated electrodes. Figure S2 shows the tangential electric field distribution across the surface region of the electrodes, whose magnitude is highest at the platinum node and is sensitive to the increase in the concentration of hydrogen peroxide that fuels the electrocatalytic reaction.

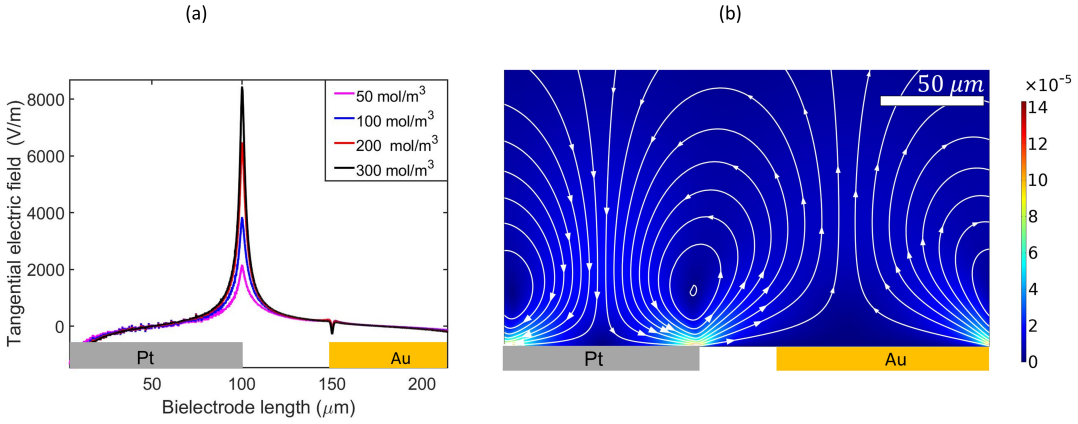

Figure S2: (a) Tangential electric field distribution across Pt-Au interdigitated electrodes (b) Velocity field streamlines for the platinum-gold interdigitated electrode driven by the induced electric field. The velocity magnitude is given in m/s

Consequently, the induced dielectrophoretic force is maximum at the surface of the platinum electrode (figure S3) and dominates over the drag and electrophoretic force at the surface region of the interdigitated electrodes (figure S4).

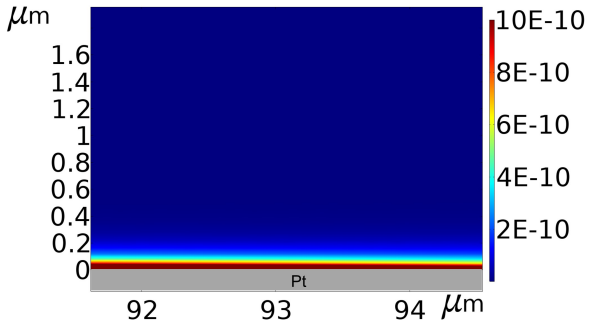

Figure S3: 2D surface plot for the dielectrophoretic force which is maximum at the platinum node of the interdigitated electrodes

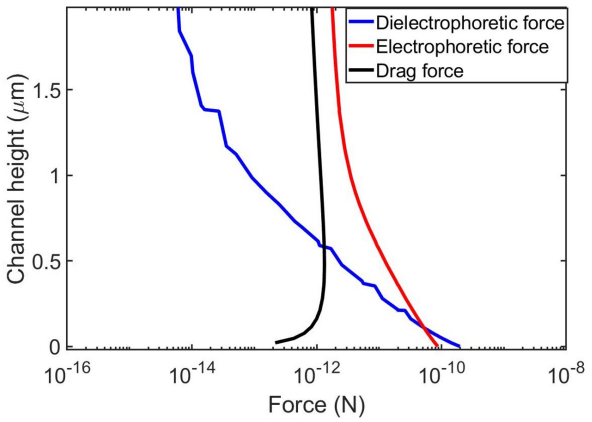

Figure S4: Variation of the forces acting on the particles along the channel height from the surface of the interdigitated electrode

S3 Brownian force

Brownian movements were observed for the particles in the absence of the drag, and electrophoretic forces, especially for the interdigitated electrodes, during the off-mode where the aggregated particles break apart and slowly disperse into the bulk fluid medium. The Brownian force is given by [21]

$$\mathbf{F}_B = \xi \sqrt{\frac{12\pi k_B \eta T r}{\Delta t}} \tag{S3.1}$$

where ξ is a dimensionless vector of independent, normally distributed random numbers, k_B is the Boltzmann's constant ($k_B = 1.38 \times 10^{-23}$ J/K), Δt is the timestep size ($\Delta t = 1$ s), T is the absolute temperature of the fluid (T = 293 K).
The resultant Brownian force acting on the particles is determined to be approximately 8.85×10^{-15} N.

S4 Supplementary movies

Four supporting movies are provided that illustrate the particle trapping and aggregation dynamics for the bimetallic and interdigitated electrodes.
Movie one shows the transport of colloidal particles by the catalytically induced flow field from platinum to gold. Movie two shows the time-lapse for

particle trapping and aggregation at the junction of the Pt-Au bimetallic electrode. Movie three shows the aggregation of particles on the surface of the platinum electrode during the connected mode for the interdigitated electrodes. Movie four shows the aggregation of the particles into clusters at longer time periods. Movie five shows the behavior of the particles under the disconnected mode of operation. The aggregates break into singlets, and the particles slowly disperse back into the bulk region.

References

[1] [n.d.]. see Supplemental Material for movies 1 - 5 at `https://figshare.com/s/8ce6e06f77db5199dc0f`.

[2] Adekanmbi, E. O., Giduthuri, A. T. and Srivastava, S. K. [2020]. Dielectric characterization and separation optimization of infiltrating ductal adenocarcinoma via insulator-dielectrophoresis, *Micromachines* **11**(4): 340.

[3] Ashaju, A. A., Wood, J. A. and Lammertink, R. G. H. [2021]. Electrocatalytic reaction-driven flow, *Phys. Rev. Fluids* **6**: 044004.

[4] Bachand, G., Rivera, S., Carroll-Portillo, A., Hess, H. and Bachand, M. [2006]. Active capture and transport of virus particles using a biomolecular motor-driven, nanoscale antibody sandwich assay, *Small* **2**(3): 381–385.

[5] Castellanos, A., Ramos, A., González, A., Green, N. G. and Morgan, H. [2003]. Electrohydrodynamics and dielectrophoresis in microsystems: scaling laws, *Journal of Physics D: Applied Physics* **36**(20): 2584–2597.

[6] Clift, R., Grace, J. and Weber, M. [2005]. *Bubbles, Drops, and Particles*, Dover Civil and Mechanical Engineering Series, Dover Publications.

[7] Davidson, S. M., Lammertink, R. G. and Mani, A. [2018]. Predictive model for convective flows induced by surface reactivity contrast, *Physical Review Fluids* **3**(5): 1–16.

[8] Ermolina, I. and Morgan, H. [2005]. The electrokinetic properties of latex particles: comparison of electrophoresis and dielectrophoresis, *Journal of Colloid and Interface Science* **285**(1): 419–428.

[9] Farniya, A. A., Esplandiu, M. J. and Bachtold, A. [2014]. Sequential tasks performed by catalytic pumps for colloidal crystallization, *Langmuir* **30**(39): 11841–11845.

[10] Galisteo-López, J. F., Ibisate, M., Sapienza, R., Froufe-Pérez, L. S., Blanco, Á. and López, C. [2010]. Self-assembled photonic structures, *Advanced Materials* **23**(1): 30–69.

[11] Guelcher, S. A., Solomentsev, Y. and Anderson, J. L. [2000]. Aggregation of pairs of particles on electrodes during electrophoretic deposition, *Powder Technology* **110**(1): 90–97.

[12] Happel, J. and Brenner, H. [1981]. *Low Reynolds number hydrodynamics*, Springer Netherlands.

[13] Hughes, M. P., Morgan, H. and Flynn, M. F. [1999]. The dielectrophoretic behavior of submicron latex spheres: Influence of surface conductance, *Journal of Colloid and Interface Science* **220**(2): 454–457.

[14] Ibele, M. E., Wang, Y., Kline, T. R., Mallouk, T. E. and Sen, A. [2007]. Hydrazine fuels for bimetallic catalytic microfluidic pumping, *Journal of the American Chemical Society* **129**(25): 7762–7763.

[15] Jan, L., Punckt, C., Khusid, B. and Aksay, I. A. [2013]. Directed motion of colloidal particles in a galvanic microreactor, *Langmuir* **29**(8): 2498–2505.

[16] Jewell, E. L., Wang, W. and Mallouk, T. E. [2016]. Catalytically driven assembly of trisegmented metallic nanorods and polystyrene tracer particles, *Soft Matter* **12**(9): 2501–2504.

[17] Kang, K. H., Xuan, X., Kang, Y. and Li, D. [2006]. Effects of dc-dielectrophoretic force on particle trajectories in microchannels, *Journal of Applied Physics* **99**(6): 064702.

[18] Kang, Y., Li, D., Kalams, S. A. and Eid, J. E. [2007]. DC-dielectrophoretic separation of biological cells by size, *Biomedical Microdevices* **10**(2): 243–249.

[19] Khoshmanesh, K., Nahavandi, S., Baratchi, S., Mitchell, A. and Kalantar-zadeh, K. [2011]. Dielectrophoretic platforms for bio-microfluidic systems, *Biosensors and Bioelectronics* **26**(5): 1800–1814.

[20] Kline, T. R., Paxton, W. F., Wang, Y., Velegol, D., Mallouk, T. E. and Sen, A. [2005]. Catalytic micropumps: microscopic convective fluid flow and pattern formation, *Journal of the American Chemical Society* **127**(49): 17150–17151.

[21] man Kim, M. and Zydney, A. L. [2004]. Effect of electrostatic, hydrodynamic, and brownian forces on particle trajectories and sieving in normal flow filtration, *Journal of Colloid and Interface Science* **269**(2): 425–431.

[22] Martínez-López, J. I., Moncada-Hernández, H., Baylon-Cardiel, J. L., Martínez-Chapa, S. O., Rito-Palomares, M. and Lapizco-Encinas, B. H. [2009]. Characterization of electrokinetic mobility of microparticles in order to improve dielectrophoretic concentration, *Analytical and Bioanalytical Chemistry* **394**(1): 293–302.

[23] Moran, J. L. and Posner, J. D. [2011]. Electrokinetic locomotion due to reaction-induced charge auto-electrophoresis, *Journal of Fluid Mechanics* **680**: 31–66.

[24] O'Konski, C. T. [1960]. Electric properties of macromolecules. v. theory of ionic polarization in polyelectrolytes, *The Journal of Physical Chemistry* **64**(5): 605–619.

[25] Ozuna-Chacón, S., Lapizco-Encinas, B. H., Rito-Palomares, M., Martínez-Chapa, S. O. and Reyes-Betanzo, C. [2008]. Performance characterization of an insulator-based dielectrophoretic microdevice, *Electrophoresis* **29**(15): 3115–3122.

[26] Pohl, H. A. [1951]. The motion and precipitation of suspensoids in divergent electric fields, *Journal of Applied Physics* **22**(7): 869–871.

[27] Punckt, C., Jan, L., Jiang, P., Frewen, T. A., Saville, D. A., Kevrekidis, I. G. and Aksay, I. A. [2012]. Autonomous colloidal crystallization in a galvanic microreactor, *Journal of Applied Physics* **112**(7): 074905.

[28] Qian, C., Huang, H., Chen, L., Li, X., Ge, Z., Chen, T., Yang, Z. and Sun, L. [2014]. Dielectrophoresis for bioparticle manipulation, *International Journal of Molecular Sciences* **15**(10): 18281–18309.

[29] Ristenpart, W. D., Jiang, P., Slowik, M. A., Punckt, C., Saville, D. A. and Aksay, I. A. [2008]. Electrohydrodynamic flow and colloidal patterning near inhomogeneities on electrodes, *Langmuir* **24**(21): 12172–12180.

[30] Schneider, C. A., Rasband, W. S. and Eliceiri, K. W. [2012]. NIH image to ImageJ: 25 years of image analysis, *Nature Methods* **9**(7): 671–675.

[31] Solomentsev, Y., Böhmer, M. and Anderson, J. L. [1997]. Particle clustering and pattern formation during electrophoretic deposition: a hydrodynamic model, *Langmuir* **13**(23): 6058–6068.

[32] Velev, O. D. and Kaler, E. W. [1999]. In situ assembly of colloidal particles into miniaturized biosensors, *Langmuir* **15**(11): 3693–3698.

[33] Wang, J. [2012]. Cargo-towing synthetic nanomachines: Towards active transport in microchip devices, *Lab on a Chip* **12**(11): 1944.

[34] Wang, W., Chiang, T.-Y., Velegol, D. and Mallouk, T. E. [2013a]. Understanding the efficiency of autonomous nano- and microscale motors, *Journal of the American Chemical Society* **135**(28): 10557–10565.

[35] Wang, W., Chiang, T.-Y., Velegol, D. and Mallouk, T. E. [2013b]. Understanding the efficiency of autonomous nano- and microscale motors, *Journal of the American Chemical Society* **135**(28): 10557–10565.

Chapter 7

Conclusions and outlook

This thesis describes our investigations on the dynamics of an electrocatalytic reaction-driven flow. By using a coupled experimental and numerical approach, we gained fundamental insights on the key elements that include the induced electric field, reaction kinetics, and concentration gradients that control the resulting mass transport characteristics. The flow is generated through heterogeneous surface reactions during the catalytic decomposition of an aqueous solution containing hydrogen peroxide, by an immobilized Pt-Au bielectrode. This leads to the establishment of ion concentrations and potential gradients that generate a body force comprising of an induced electric field and a net charge zone that drives the fluid flow.

7.1 Induced potential and electric field

An electrocatalytic system, consisting of Pt-Au bimetallic system within a hydrogen peroxide solution, was analyzed as a simple electrochemical cell whose characterization gives insights into the electrochemical reaction pathway and kinetics. Electrochemical characterization was conducted through current-potential measurements using interdigitated electrodes, via induced potential measurement (IPM) and the Tafel analysis. For the induced potential measurement, the potential difference is measured between the short-circuited electrodes and the electrolyte during the electrochemical reaction. During the connected mode, a common electrode potential is induced, also termed in this context as the bimetallic potential, which balances reactive fluxes on the electrodes to enforce current conservation under steady-state conditions. For the Tafel analysis, the mixed potential theory is applied to the current-voltage response. Each electrode was subjected to potential sweeps within the oxidation and reduction range, and the measured current is plotted in logarithm form versus potential to create the TAFEL plots from which the bimetallic potential and catalytic currents are directly inferred. The bimetallic potential is comparable to the potential obtained from IPM, while the catalytic current yields more information that pertains to the reaction rate and the flux on the electrode surface that serves as an input for the numerical simulations. These results confirm the catalytic decomposition of hydrogen peroxide as the dominant reaction pathway that powers the generation of the surface induced fluid flow. Both electrochemical and numerical results demonstrate the role of the induced potential by Pt-Au bimetallic system as a control mechanism for balancing reactive currents from the electrode. The steady state enforcement occurs through the adjustment the surface concentration of H^+ by the induced

potential. This is evident for reaction regimes under bulk pH 4, where the induced potential is negative. These results provides insight and clues for the design and optimization of electrocatalytic systems targeted at near surface mixing related applications.

7.2 Fluid flow field

The electrocatalytic reaction-driven flow for a Pt-Au and H_2O_2 system is typically driven from the anode towards the cathode and recirculated within a confined volume due to continuity. The fluid flow was visualized using tracers particles, which are dragged by the flow field. The velocity of the particles consists of both the electrophoretic and drag flow components, hence we used the 2-particle correlation technique to extract the fluid flow velocity and construct the velocity profile within the confined volume. This approach involves the usage of particles having a similar size and different surface charges to decouple the velocity components from each other. We observed that the particle movements close to the bielectrode surface region are highly influenced by a strong electrophoretic force, generated from the interactions between the charged particles and induced electric field, making accurate evaluation of the fluid velocity challenging. To circumvent this problem, the upper parabolic part of the velocity, where the electrophoretic effect is minimal, was fitted with an analytical expression to yield the maximum induced surface velocities at the electrode. The fluid velocity was found to be highly sensitive to the concentration and pH of the electrolyte solution. The dynamics of the fluid flow were investigated under several reaction regimes, created by varying the concentration with the bulk pH of hydrogen peroxide, as well as the presence of additional charged species such as Cl^-. The reaction regimes are defined by the dimensionless Damköhler number (Da), a parameter that relates the reaction timescale to a diffusive timescale. At higher anodic Da_a, the induced flow is similar in pattern to an electroosmotic flow where flow is driven from the anode to the cathode. At lower Da_a, the flow direction becomes fully reversed. The reaction regime that is associated with the transition from reverse to normal flow varies for different bulk pH variations and is signified by the formation of a counter-rotating vortex pair. These results are valuable for understanding the behaviour of the electrocatalytic systems within different ionic-medium conditions involving pH and ionic-strength. Moreover, a level of control can be exerted on the directionality of the fluid flow.

7.3 Numerical modeling

A 2D numerical model was formulated based on the Poisson-Nernst-Planck and Stokes equations to obtain more insights in and interpretation of the experimental results. The model includes the dependence of the electrodes' zeta potentials on pH variations, the auto-ionization reaction of water, and the acid equilibrium reaction that occurs during bulk pH adjustment. The model yielded more insights on the interplay and synergy between the key elements such as the induced fields (proton gradient, potential, and electric field), and the electrode reactivity that controls the production and depletion of protons in the resulting fluid flow, and reproduces velocities that are relatively the same order of magnitude and structure as the experimental results. The model results offered clues on improving the performance of the electrocatalytic system under different reaction regimes.

7.3.1 Proton gradient

In chapter five, the dynamics and origin of the flow reversal generated under lower anodic reactive regimes was considered. This phenomenon which could not be accounted for by the classical electroosmosis theory was approached fundamentally by examining the proton concentration gradient, which is central to the chemomechanical actuation of the bimetallic system. The proton gradient was spatially mapped and quantified using fluorescence lifetime imaging microscopy (FLIM). The FLIM analysis confirms the development of the proton gradient during the electrocatalytic reactions that establish the mass transport characteristics of the system. From the numerical results, it was established that the proton concentration gradient can be amplified or weakened depending on the reaction regime influenced by bulk pH variations, which has considerable consequences for the resulting diffusio-electroosmotic phenomena.

7.3.2 Reaction-induced particle aggregation

The aggregation of colloidal tracer particles used for visualizing the flow field was the subject of interest in chapter six. The experimentally visualized flow with tracer particles exhibits a combined electrohydrodynamic mechanism. Apart from the transport of particles along the flow direction from the anode to the cathode, the particles are observed to be (di)electrophoretically trapped and aggregated at the junction of the bielectrode, where the magnitude of the electric field is at its maximum. With time, the aggregation of particles

evolves into the formation of clusters that are clearly visible at the bielectrode junction. By using Pt-Au interdigitated electrodes, the electrocatalytic reaction was controlled by connecting and disconnecting the electrodes, to which the particle aggregation reacted, which confirms its dependence on the reaction-induced electric field. The particle aggregation study was advanced by proposing a DC dielectrophoretic force as the underlying mechanism for Immobilized bimetallic electrocatalytic systems. This hypothesis was tested using numerical models whose simulation yielded result that is consistent with experimental result. The current results and analyses helps to advance the existing knowledge on reaction-induced colloidal patterning and aggregation driven by immobilized electrocatalytic systems.

7.4 Perspectives and outlook

Research is an endless quest for knowledge and a continuous search for truth. Despite the achievements in this project, some hurdles still lie ahead, which will be discussed, with useful suggestions proposed to tackle them.

7.4.1 Mixing application

Electrocatalytic reaction-driven flow opens up new pathways for manipulating fluid flow for microscale applications, and one of which I explored was for micromixing applications, which has attracted several interests aimed at developing a system capable of achieving an optimum and rapid mixing of chemical or biological reactants within a microfluidic device. An ideal micromixer should offer a shorter mixing length and time [2]. However, in comparison with other forms of active micromixers that are driven by an externally applied field (AC, DC electric fields) [9], and acoustic energy [7], the mixing efficiency appears to be low as the velocity magnitude is several order of magnitude lower than its external counterparts. The mixing efficiency may be enhanced by integrating several electrocatalytic reactors that are alternately positioned to generate counter opposing flows capable of improving mixing efficiency. This approach involves using several repeated bielectrode patterns, which might not be cost-effective considering the types of metals that constitute the system. This may be solved by researching low-cost metals that can be alloyed with other transitional metals that possess a high reactivity capable of enhancing the flow and mixing output. The surface modification of the electrodes with catalytic coatings involving layers of catalytic oxides might be another solution that im-

proves the functionality and reactivity of the metals towards flow and mixing enhancement.

7.4.2 Fluid flow quantification

Particle tracking and imaging velocimetry form popular choices for measuring the trajectories and velocities using tracer particles. However, the fluid flow quantification for the electrocatalytic system, especially at lower anodic reactive regimes, becomes complicated because the charged particle movements are affected by a strong electrophoretic force that require corrections for obtaining the fluid flow. Furthermore, it has been proven that charged particles near charged surfaces are capable of inducing electroosmotic flow [10], which in this context may perturb the electrocatalytic reaction-driven flow. In chapter four we fitted the upper parabolic part of the velocity profile to determine the surface-induced velocity. However, this wasn't possible for the reversed flow obtained under lower reactive regimes in chapter five, due to the lack of flow symmetry at the upper part of the channel. The need for an alternative flow visualization and quantification techniques is crucial at the point. A possible method would be to seed the fluid medium with neutral particles. A neutral particle possesses zero electrophoretic mobility, whose advection is representative of the electrocatalytic reaction-driven flow. In this line of thought, PEG-functionalized particles were explored. However, these particles still have some significant surface charge (14 mV, pH 6) needed to keep the colloidal suspension stable to prevent flocculation, making them susceptible to the electric field. A good substitute would be neutral markers or dyes, which can be tracked using either ultraviolet absorption or fluorescence emission detection. It is capable of migrating with the induced fluid flow, and the electroosmotic mobility can be determined from its migration time based on the relation $\mu_{eo} = Ll/\phi t_{eo}$, where l is the distance from the position of the neutral marker injection to the detector, ϕ/L is the induced potential gradient and t_{eo} is the time of migration [8, 3].

7.4.3 Proton concentration gradients

Fluorescent lifetime imaging was used to visualize the steady-state proton concentration profile established across the bielectrode. However, this technique has its limitations. FLIM is unable to resolve the steeper concentration gradient at the near electrode surface. Total internal reflection fluorescence microscopy (TIRFM) would be a suitable alternative towards resolving the

localized steeper pH gradient. It has been used in the field of biophysics to observe molecular events at the nanometric range [5] and combined with electrochemistry to study dynamics close to electrode surfaces involving single-molecule electrochemistry [4]. TIRFM can be coupled with FLIM selectively illuminate fluorophores within near surface region to unravel the steep proton gradient surface that was presented in our simulation result.

7.4.4 Particle aggregation modelling

For the modeling of the particle aggregation dynamics, the rotational motion of the particle was neglected, likewise the effects of the particles on field variables (potential and flow) through 2-way coupling, which requires more computational power and time. Moreover, the current model fails to capture the 3D formation of clusters whose growth extends to a few heights above the surface of the electrodes. The existing model can be improved by considering a 3D model where translational $\mathbf{u}_p$ and rotational ω_p boundary conditions are prescribed on the particle surface [1]. The 3D model should capture the formation of rafts and clusters as observed experimentally. The Arbitrary Lagrangian-Eulerian (ALE) method will be effective for this purpose, such that the particle movements are resolved using the Lagrangian approach, while the continuous phase involving the flow and electric field is solved based on the Eulerian approach [6].

Finally, This thesis has demonstrated a proof-of-concept for immobilized electrocatalytic systems that is based on Pt-Au and hydrogen peroxide as a micropump that drives fluid flow and provided analyzes on the behavior of the system under different reactive conditions involving concentration and pH. In order for it to perform better than its externally controlled counterparts, its low efficiency has to be readily addressed. By improving the catalytic activity of the electrodes that catalyzes the electrochemical reactions that creates the potential and concentration gradients, and by researching suitable alternative fuels. The full integration of immobilized electrocatalytic devices into microfluidics systems for flow manipulations and control would eliminate energy demands that arises for an externally controlled microfluidics system.

References

[1] Ai, Y., Joo, S. W., Jiang, Y., Xuan, X. and Qian, S. [2009]. Transient electrophoretic motion of a charged particle through a converg-

ing–diverging microchannel: Effect of direct current-dielectrophoretic force, *Electrophoresis* **30**(14): 2499–2506.

[2] Chang, C.-C. and Yang, R.-J. [2007]. Electrokinetic mixing in microfluidic systems, *Microfluidics and Nanofluidics* **3**(5): 501–525.

[3] Devasenathipathy, S. and Santiago, J. [2005]. *Electrokinetic Flow Diagnostics*, Springer Berlin Heidelberg, Berlin, Heidelberg, pp. 113–154.

[4] Fan, S., Webb, J. E. A., Yang, Y., Nieves, D. J., Gonçales, V. R., Tran, J., Hilzenrat, G., Kahram, M., Tilley, R. D., Gaus, K. and Gooding, J. J. [2019]. Observing the reversible single molecule electrochemistry of alexa fluor 647 dyes by total internal reflection fluorescence microscopy, *Angewandte Chemie International Edition* **58**(41): 14495–14498.

[5] Fish, K. N. [2009]. Total internal reflection fluorescence (tirf) microscopy, *Current Protocols in Cytometry* **50**(1).

[6] Hu, H. H., Patankar, N. and Zhu, M. [2001]. Direct numerical simulations of fluid–solid systems using the arbitrary lagrangian–eulerian technique, *Journal of Computational Physics* **169**(2): 427–462.

[7] Rasouli, M. R. and Tabrizian, M. [2019]. An ultra-rapid acoustic micromixer for synthesis of organic nanoparticles, *Lab on a Chip* **19**(19): 3316–3325.

[8] Sandoval, J. E. and Chen, S.-M. [1996]. Method for the accelerated measurement of electroosmosis in chemically modified tubes for capillary electrophoresis, *Analytical Chemistry* **68**(17): 2771–2775.

[9] Zhang, K., Ren, Y., Hou, L., Feng, X., Chen, X. and Jiang, H. [2018]. An efficient micromixer actuated by induced-charge electroosmosis using asymmetrical floating electrodes, *Microfluidics and Nanofluidics* **22**(11).

[10] Zhao, H. and Bau, H. H. [2007]. On the effect of induced electro-osmosis on a cylindrical particle next to a surface, *Langmuir* **23**(7): 4053–4063.

Summary

Nature has engineered several high-precision locomotions of biological systems that are powered by the conversion of biochemical energy sourced from their local environment. This has inspired a myriad of research and developmental activities on artificial micromachines, aimed at understanding and replicating the complex functionalities presented by these biological motors. A good example is the autonomous locomotion of a catalytic nanorod that functions primarily on the conversion of chemical energy harvested from its surrounding fluid media. This nanorod consists of a pair of connected electrodes that catalyzes the decomposition of an aqueous solution, which leads to the creation of concentration and electrical gradients that propels the nanorod. If the motility of the nanorod is restrained, an interfacial flow will be generated based on Galilean invariance. The immobilized system is referred to as an electrocatalytic micropump, and the induced flow has the potential to mitigate mass transport limitations in microsystems. However, some issues limit the practical usage of an electrocatalytic micropump, especially its low energy conversion. This thesis investigates the fundamental parameters that drive the electrocatalytic reaction and impacts the chemomechanical actuation of the bimetallic system, through a combined experimental and numerical approach. Chapter one provides an introductory background on nanomachines in form of catalytic micromotors and micropumps with a concise description of the research objectives. In Chapter two a comprehensive review of the research field involving immobilized bimetallic systems is discussed, detailing the latest advances on the composition, characterization, and applications with this system. A comparative analysis for the power efficiency of several forms of the bimetallic catalytic system is provided. In chapter three, the numerical framework in the form of a 2D model that simulates the Pt-Au and hydrogen peroxide bimetallic system is formulated. This is based on Poisson-Nernst-Planck and Stoke's equations. The model dynamically couples the experimentally measured zeta potential of each electrode to the solution bulk

pH and accounts for bulk reactions that include water self-ionization and acid equilibrium. The key elements that contribute to the electrocatalytic reaction-driven flow are investigated and analyzed in chapter four. The electrocatalytic current between the electrodes and the induced potential that governs the reactive flux are measured electrochemically and the fluid flow is visualized and quantified using two-particle correlation. The interplay between the surface reactivity patterns of the electrodes, which is characterized by the dimensionless Damköhler number, with the resulting fluid flow is analyzed numerically. The flow is observed to be fully reversed at low anodic regimes (Da_a).

The origin and dynamics of the flow reversal under different reaction regimes are fundamentally studied in chapter five. The proton gradient triggers the overall electrokinetic process and was hypothesized as the causative factor of flow hysteresis. It is investigated using steady-state conditions using fluorescence lifetime imaging (FLIM). The variation of the proton gradient under bulk pH conditions and its consequences for the induced field variables are presented and analyzed. The combination of the numerical and experimental analyses elucidates the role of pH variations and additional ionic species (counterions) towards flow reversal obtained under lower anodic reactive regimes (Da_a).

Tracer particles are commonly used to visualize the surface reaction-driven flow. In addition to the advective transport, the particles are observed to aggregate and form clusters at the junction of the bielectrode. These phenomena that are mediated by the induced electric field, including its kinetics are investigated in chapter six. The results and analysis highlight the reaction-induced dielectrophoretic force as the underlying mechanism for the attraction, trapping, and aggregation of the tracer particles within the region of high electric field strength.

This work contributes towards the fundamental understanding of fluid flow powered by chemically powered micropumps that applies to mass transport enhancement in electrochemical systems.

Samenvatting

De natuur heeft verschillende zeer nauwkeurige locomoties van biologische systemen ontwikkeld die worden aangedreven door de omzetting van biochemische energie afkomstig uit hun lokale omgeving. Dit heeft een groot aantal onderzoeks- en ontwikkelingsactiviteiten op kunstmatige micromachines geïnspireerd, gericht op het begrijpen en repliceren van de complexe functionaliteiten van deze biologische motoren. Een goed voorbeeld is de autonome voortbeweging van een katalytische nanostaaf die primair functioneert op de omzetting van chemische energie die wordt gewonnen uit de omringende vloeibare media. Dit nanostaafje bestaat uit een paar verbonden elektroden die de ontleding van een waterige oplossing katalyseren, wat leidt tot het creëren van concentratie en elektrische gradiënten die het nanostaafje voortstuwen. Als de beweeglijkheid van de nanostaaf wordt beperkt, wordt een grensvlakstroom gegenereerd op basis van Galileïsche invariantie. Het geïmmobiliseerde systeem wordt een elektrokatalytische micropomp genoemd en de geïnduceerde stroom heeft het potentieel om de beperkingen van het massatransport in microsystemen te verminderen. Sommige problemen beperken echter het praktische gebruik van een elektrokatalytische micropomp, vooral de lage energieconversie. Dit proefschrift onderzoekt de fundamentele parameters die de elektrokatalytische reactie aansturen en de chemomechanische aandrijving van het bimetaalsysteem beïnvloeden, door middel van een gecombineerde experimentele en numerieke benadering.
Hoofdstuk één geeft een inleidende achtergrond over nanomachines in de vorm van katalytische micromotoren en micropompen met een beknopte beschrijving van de onderzoeksdoelstellingen.
In hoofdstuk twee wordt een uitgebreid overzicht van het onderzoeksveld met geïmmobiliseerde bimetaalsystemen besproken waarin de laatste vorderingen op het gebied van samenstelling, karakterisering en toepassingen met dit systeem worden beschreven. Er wordt een vergelijkende analyse gegeven voor de energie-efficiëntie van verschillende vormen van het bimetaalkatalytische

systeem.
In hoofdstuk drie wordt het numerieke raamwerk geformuleerd in de vorm van een 2D-model dat het Pt-Au en waterstofperoxide bimetaalsysteem simuleert. Dit is gebaseerd op de vergelijkingen van Poisson-Nernst-Planck en Stokes. Het model koppelt dynamisch de experimenteel gemeten zeta-potentiaal van elke elektrode aan de bulk-pH van de oplossing en houdt rekening met bulkreacties waaronder zelfionisatie van water en zuurevenwicht.
De belangrijkste elementen die bijdragen aan de elektrokatalytische reactiegedreven stroom worden onderzocht en geanalyseerd in hoofdstuk vier. De elektrokatalytische stroom tussen de elektroden en het geïnduceerde potentieel dat de reactieve fluxen regelt, wordt elektrochemisch gemeten en de vloeistofstroom wordt gevisualiseerd en gekwantificeerd met behulp van correlatie met twee deeltjes. Het samenspel tussen de oppervlaktereactiviteit van de elektroden, die wordt gekenmerkt door het Damköhler nummer, met de resulterende vloeistofstroom wordt numeriek geanalyseerd. Er wordt waargenomen dat de stroom volledig omgekeerd is bij laag anodische regimes (Da_a).
De oorsprong en dynamiek van de stroomomkering onder verschillende reactieregimes worden fundamenteel bestudeerd in hoofdstuk vijf. De protongradiënt trapt het algehele elektrokinetische proces af en werd verondersteld de oorzakelijke factor van de stromingshysterese te zijn. Het wordt onderzocht met behulp van steady-state condities met behulp van fluorescence lifetime imaging (FLIM). De variatie van de protongradiënt onder bulk-pH-condities en de gevolgen daarvan voor de geïnduceerde veldvariabelen worden gepresenteerd en geanalyseerd. De combinatie van de numerieke en experimentele analyses verduidelijkt de rol van pH-variaties en extra ionsoorten (tegenionen) in de richting van omkering van de stroom die wordt verkregen onder lagere anodische reactieve regimes (Da_a).
Tracerdeeltjes worden vaak gebruikt om de reactiegedreven stroming aan het oppervlak te visualiseren. Naast het advectieve transport, wordt waargenomen dat de deeltjes aggregeren en clusters vormen op de kruising van de biëlektrode. Deze verschijnselen die worden gecontroleerd door het geïnduceerde elektrische veld, inclusief de kinetiek ervan, worden onderzocht in hoofdstuk zes. Het resultaat en de analyse geven de door reactie geïnduceerde diëlektroforetische kracht aan als het onderliggende mechanisme voor het aantrekken, vangen en aggregeren van de tracerdeeltjes in het gebied van hoge elektrische veldsterkte. Dit werk draagt bij tot het fundamentele begrip van vloeistofstroming aangedreven door chemisch aangedreven micropomp die van toepassing is op verbetering van het massatransport in elektrochemische systemen.

Acknowledgements

"Veni Vidi Vici"

The journey of a thousand miles that began with some steps has finally been completed on a successful note. This would not have been possible without the support, guidance, and mentorship of my supervisor **Rob Lammertink**. He saw the potential in me towards the contribution to science and decided to take me on board. Thank you for guiding me on becoming a better researcher, by approaching a problem fundamentally, likewise being critical and thorough on data analysis and interpretation. Coming from a mechanical engineering and thermofluids science background, you introduced me to the world of electrokinetics, which was a learning curve. Thanks for giving me the independence and flexibility to explore my ideas, regardless of if they appeared sound or crazy. Your objectiveness and positivity during our weekly meetings always renewed my optimism especially when my results took several unexpected turns. Your excellent leadership skill is a trait that I strive to emulate along my career path.

I would like to thank **Jeff**, who was involved with my project, especially on the numerical modelling aspect. Your wit, wisdom, and resourcefulness have helped me to navigate several complex and technical hurdles. Your door was always open for valuable scientific discussions, after which I returned to my work desk to reflect, process, and decrypt every piece of information. Thank you for all your scientific input. I am privileged to have worked with you. I would like to appreciate my graduation committee members: Jan, Serge, Ali, Corinna, and Cécile for creating time from your busy schedule to assess my thesis. I appreciate **Moritz** and **Burak** for accepting to be my paranymphs.

On coming to Utwente, my first point of contact was **Lidy**. Thank you for helping me out with several administrative formalities during that period. I would also like to thank **Brigitte** and **Audrey** for their support in resolving administrative issues, especially with the financial departments. **Audrey**, it

was always fun conversing with you in dutch. You and **Bob Siemerink** have helped me to improve my Dutch proficiency through constant conversational practice.

My experimental success wouldn't have been possible without the help of **Jan** and **Ineke**. Your role behind the scenes is always a contributing factor to the success of the SFI group. Ineke helped and taught me to create PDMS channels, which was instrumental to my experiments. Jan encouraged me to acquire and hone my technical skills, especially in lithography, micromachining, and other microfabrication activities. These intangible gifts have decorated my work experience and open more opportunities for me in the industry.

To the present **SFI** colleagues, you have played a direct and indirect role in making my doctoral journey memorable. How can I forget my **SFI sisters Arputha and Dona**, who were there for me from the beginning to the end? During the pre-corona era, we were office-mates. We shared our successes, frustrations and extended our friendship outside work. Dona thanks for dealing with my endless questions according to your experience, which saved me from a lot of headaches. Your presence with Arputha at my wedding made the day more special with your colorful cultural appearance. Thanks, Arputha for remodeling our office with decorations, pictures, and flowers making it feel as working from home. Three years later Moritz joined us in the office and contributed to a pleasant working atmosphere. Thank Moritz, for making readily available cookies and chocolates in the office to snack on during stressful working hours. **Nicole and Burak**, we had interesting discussions regarding our work on common grounds. I wish you all the best on the remaining part of your program and I trust you both to nail the diffusion-osmosis project.

I am grateful to **Veerle** who chose my project for her master thesis. She worked on the electrochemical part and delivered important results and contributions.

Thanks to **Koen** for proofreading the samenvatting.

To the **SFI Alumni**, whom I've been privileged to work with. You are part of my success story. I am grateful to **Khalid** for giving me a lab tour on my first time with the group and teaching me how to use the FLIM setup. **Anne Benneker** and who helped me to jumpstart my microscopy experiment and taught me the right way of using a pipette. I'm grateful to Aura who provided me with valuable information at the start of my project after having worked with Pt-Au bimetallic catalysts. I appreciate **Pim Bullee** for his help with the μ-PIV setup. Thanks for also teaching me some Twentse slang such as "mooi pannenkoeken".

To the MST, cluster and colleagues, thanks for making my time here worthwhile. We had several nice moments together during activities such as the study tour to Denmark, MST bike tour, and safety day. During the winter school in Austria, I took ski lessons together with Ettore, Nikos, Elif, Shuyana, etc after which I could confidently ski on the blue slope. I would like to thank the Futsal AC membrane team, Mehrdad, Almond, Frank, Denis, etc for the beautiful memories we made during friendly matches with other groups at the sport centrum. We won and lost a couple of matches, but most importantly, we played together as a team.

I acknowledge the mentorship role played by Dr. **Odesola** and Dr. **Ige** during my master's degree program at the University of Ibadan. Likewise, **Xavier** and **Stéphane** who gave me a solid foundation on CFD and multiphase flow research during my time at U-pem.

To my Dutch family (**van der velde**) here in the Netherlands; Bedankt voor jullie interesse in mijn werk. Bedankt dat jullie me in het weekend bij verschillende uitstapjes en activiteiten hebben betrokken. Dat heeft mij geholpen om een balans te vinden, om werkstress opzij te zetten en om met een frisse blik weer te kunnen beginnen aan de volgende week. Bovendien steunden jullie mij constant en hebben jullie mij geholpen om hier goed in de samenleving te integreren. Ik ben enorm dankbaar en ik hou van jullie allemaal.

I am grateful to my family (**Ashaju**) who were supportive of my decisions to chart my path careerwise. To my Dad, who continually encouraged me to be diligent in my academic pursuits. To my mum (abiyamọ tòótọ́) whose endless support and prayers kept me going at all times, and my siblings Femi, Bolaji, Wumi, and Bola for their love and support over the years. Ẹ seun fún àtilẹ́yìn.

To my daughter **Nora**, the most important title I will ever have is being a Dad. Towards the twilight of my PhD program, I assumed fatherhood and learned quickly how to juggle parenthood with work.

To me dear wife **Inge**, thanks for being my true companion during the highs and lows of my PhD time and dealing with my crazy workaholic lifestyle. You helped me to achieve a healthy work-life balance during my doctoral journey. Thanks for your understanding whenever I'm back home after a tough day in the lab and while burning the midnight oil to meetup with deadlines. You have always been my number one supporter, by practicing my presentations with me giving me important feedback. Thanks for inspiring and motivating me to be a better man and husband. Mo nifẹ rẹ.

Lastly, I am grateful to God for sound health, sound mind, and who engraced me to finish my doctoral race on a high note. Ogo ni fun olorun loke ọrun.

Abimbola Ashaju
2021

About the author

Abimbola Ashaju was born on the 3rd of May 1988 in Lewisham United kingdom and grew up in Nigeria, where he obtained his Bachelor's degree in mechanical engineering. He obtained some work experience in the Refrigeration and Airconditioning industry working as a project engineer.
He embarked on a master of science program at the University of Ibadan where he majored in thermal-fluids science and pursued a second-year master's research program (M2) at Université Paris-Est Marne-la-Vallée, where he majored on modelling and simulation of fluid mechanics and heat transfer.
He interned at Veolia Research and Innovation Maison-Laffittes France where he contributed to the development of a water-based sensor for monitoring portable water conditions in France in real-time.
In 2017 he embarked on a Ph.D. program within the Soft matter, Fluidics, and interfaces group at the University of Twente under the supervision of Prof, dr. ir. Rob. G.H. Lammertink. The project is part of the research program, themed "Stirring the boundary layer" which was financed by the Dutch Research Council (NWO).
In May 2021, he started working as a R&D scientist at Veco precision in Eerbeek.

Scientific output

- **2021:** *Electrocatalytic Reaction-Driven flow*
  A.A Ashaju, J. A. Wood, R.G.H Lammertink
  Physiscal Review Fluids **6**, 044004 (2021)

- **2021:** *Electrocatalytic Reaction Driven: The role of pH on flow reversal*
  A.A Ashaju, J. A. Wood, R.G.H Lammertink

- **2021:** *Electrocatalytic reaction induced colloidal aggregation*
  A.A Ashaju, J. A. Wood, R.G.H Lammertink

Conferences, oral and poster presentations

- **2019: APS-Division of fluid dynamics, Seattle**
  Surface Reaction Driven Flow

- **2019: European Colloid & interface society (ECIS)**
  Surface Reaction Driven Flow

- **2019: Chemistry as Innovative science (CHAINS) NWO**
  Surface Chemistry Induced flows

- **2020: APS- Division of fluid dynamics (Virtual), Chicago**
  Electrocatalytic Reaction Driven flow: The role of pH on flow reversal

- **2021: European Symposium on Electrochemical Engineering (ESEE)**
  Electrocatalytic Reaction Driven flow